

Model-based Control in Adaptive Optics Systems

Hong SONG

PhD Thesis

Cover: Water reflection of a bridge in the old town of Delft
Designed by YANG Ping

MODEL-BASED CONTROL IN ADAPTIVE OPTICS SYSTEMS

PROEFSCHRIFT

ter verkrijging van de graad van doctor
aan de Technische Universiteit Delft,
op gezag van de Rector Magnificus Prof. ir. K.C.A.M. Luyben,
voorzitter van het College voor Promoties,
in het openbaar te verdedigen op
vrijdag 25 maart 2011 om 10:00 uur

door

Hong SONG

Master of Science in Electrical Engineering
Delft University of Technology
Master of Science in Microelectronics and Solid-state Electronics
Fudan University, Shanghai, China
geboren te Jingjiang, Jiangsu Province, China

Dit proefschrift is goedgekeurd door de promotor:

Prof. dr. ir. M. Verhaegen

Copromotor: Dr. G. Vdovin

Samenstelling promotiecommissie:

Rector Magnificus,	voorzitter
Prof. dr. ir. M. Verhaegen,	Technische Universiteit Delft, promotor
Dr. G. Vdovin,	vml. UHD-EWI, copromotor
Prof. dr. ir. G. Schitter,	Vienna University of Technology
Prof. dr. ir. C.U. Keller,	Utrecht Universiteit
Prof. dr. ir. D.J. Rixen,	Technische Universiteit Delft
Prof. dr. ir. J.A. Mulder,	Technische Universiteit Delft
Dr. ir. N.J. Doelman,	TNO Industrie en Techniek
Prof. dr. ir. P.J. French,	Technische Universiteit Delft, reservelid

The work presented in this thesis has been supported by the Delft Center for Mechatronics and Microsystems (DCMM).

ISBN: 978-94-91211-10-2

Copyright © 2011 by Hong Song.

All rights reserved. No part of the material protected by this copyright notice may be reproduced or utilized in any form or by any means, electronic or mechanical, including photocopying, recording or by any information storage and retrieval system, without written permission from the copyright owner.

Printed in The Netherlands

Author's email: cdreaming@gmail.com

To my family

Acknowledgments

During the past five years, I have got generous and continuous support and encouragement from my supervisors, colleagues, friends, and my family. I am really in a luxury situation because there are so many people around. I'd like to express my sincere gratitude to you all!

Special thanks to my supervisor — Prof. Michel Verhaegen! First of all, thanks for offering me the opportunity to start as a PhD student! It's you who brought me into such a big but almost invisible world of systems and control. Thanks a lot for your patience, in distilling key points out of all the awkward progress reports and teaching me to be more specific, more precise and more concrete through our many discussions. Thanks for putting me on the right track from time to time when I got lost in the darkness and giving me all the opportunities and freedom to play with the setup (I usually see them as my toys). And, thanks a lot for your solid support in my career development!

Thanks to my supervisor — Dr. Gleb Vdovin! You showed me not only the power of adaptive optics, but also a good example how to turn knowledge into successful business. Working with you is always a lot of fun. Thanks for replying my first email for a master project! Thanks for providing valuable comments and suggestions on my research! Thanks for showing me how a (seemingly) complicated problem can be solved in a simple way! Also thank for your care on my daily life!

Thanks to my supervisor — Dr. Rufus Fraanje! Although unwritten in the title page, you are surely my supervisor! Thanks for your patience, your willingness to help all the time, your brainstorming, suggestions and ideas! Thanks for commenting on my reports and papers word by word! Thanks for sitting beside me until late with the experiments! Thanks for introducing Dutch culture to me and translating the summary and propositions! Thanks for the nice dinners, bicycle and bicycle lamp!

Thanks to my supervisor — Prof. Georg Schitter! You are always generous in providing me inputs from both theoretical and practical sides, from which I benefit a lot! Thanks for always notifying me the key points that I overlooked! Thanks for helping me debug the setup with cables, probes and oscilloscope! Thanks for calming me down when I was anxious about my progress and my thesis! And thanks for all your support in my career development!

Thanks to Will van Geest, my solid support for all the issues on computers, cards and cameras! I could not have had any running setup if without your help in selecting the hardware, building up the control system and removing all the barriers! Thanks to Olaf for ordering the components, financial management and lab arrangement! The experimental setups could not have been built up so smoothly if without your help. Thanks to Arjan van Dijke for supporting the dSPACE system! Thanks to Kees and Ron for the help in electronics and starting the relaxation every Friday afternoon! Thanks to John Seiffers for setting up the optical table in the lab.

Thanks to Kitty for showing me my desk, giving me the key of my office, arranging everything in advance and providing kind advice! Thanks to Ellen, Saskia and Esther for handling all the forms and ordering office facilities.

Thanks to Prof. Bosgra for the instructions on how to be a good student assistant, how to encourage students and how to prepare solutions for the exercise and exams!

Thanks to all the committee members for reading through my thesis and providing me comments, which helps to improve the thesis a lot!

Thanks to my officemate Jelmer for translating Dutch letters and documents, always taking fresh ideas to my mind and having regular exercise together in the morning and afternoon! Although it is difficult to get up early in the morning, arriving at the office before 8 o'clock makes me feel the day get much longer!:) Thanks to Jan-Willem for getting me acquainted with DCSC and for this great thesis template! Thanks to Eric for instructing me how to make some noise!

Thanks to Dong Jianfei for being the first DCSC colleague speaking Chinese with me and playing Taiji together every Monday! Thanks to Pian Xiaochuan, Li Bei, Wang Yubin, Wangli Dongzi, Wei Xiukun, Shi Jing, Li Xuan, Chen Yiquan, Li Yuping, Lin Shu, Cong Zhe for all the warm talks and gatherings!

Thanks to Karel for your great thesis and all the codes, which I studied most in the past years! Thanks to Rogier for the AO toolbox! Thanks to Roland for instructions on the control lab assignment at the beginning of my PhD and the advice on making a fair comparison! Thanks to Diederick for sharing the experience in job hunting! Thanks to Ivo for inspiring me with the idea of fishing and the code on closed-loop subspace identification!

Thanks to Henk for initializing the wavefront-sensor-less AO setup and your great thesis. From your work, I got a vivid picture on how WFSless AO is really working and got some clue how to make it faster. Also, I am really impressed by your hand-on skills, like making a rail from sketch. Thanks to Wouter for working with me in the lab and sharing your opinions on doing research. Thanks to Markus for your great work on model predictive control (DM modeling, algorithms, C++, etc.), from which I got more aware of that every component has its own limit and it's so important to get the best performance out of it within its limit.

Thanks to Paolo for the help in matrix computation, and more surprisingly, writing to me in Chinese! I wish you enjoy the nice food (mei shi), nice wine (mei jiu), and happy life in Paris! Xie Xie!

Thanks to Arjan, Arturo, Jacopo, Federico, Hans, Ruxandra for sharing your knowledge, new findings, problems and solutions in imaging systems! Thanks to Remko Stuik from Leiden Univ. for your patient explanations on conjugated planes.

Thanks to Snezana for the discussions on the DISC homework and for answering difficult questions in the exercise courses! Thanks to Jan and Stefan for the discussions on the piezo stuff (hysteresis, charge control, dynamics, etc.), but also the talks during the coffee break, lab break and sports break! Thanks to Mathieu for fun in the fool-day drink when I was really fooled!

Thanks to Aleksandar, Alessandro, Arturo, Andrea, Aydin, Justin, Nikola, Stefan, Pawel and Dang for the fun in playing basketball! Thanks to Rudy and Robert for the tennis matches! Thanks to Justin for the Frisbee and notifying me not to work too hard! Thanks to Arturo for solving too simple/stupid latex problems! Thanks to Andrea for showing me his superb basketball skills and the dancing workshop!

Thanks to Navin, Lakshimi, Amol for introducing Indian culture! Thanks to Ali and Samira for the nice food for the Persian New Year! Thanks to Peter, Tamaz, Gabriel, Ilhan, Solomon, Matteo, Alfredo, Katerina, Noortje, Ilya, Patricio, Yashar for many nice talks!

Thanks to Inge and Marcel for organizing all the DCMM exhibitions and customer days such that I have the opportunities to present my work to a broad spectrum of audience and get feedback from them!

Thanks to Dr. Oleg Soloviev and Dr. Mikhail Loktev from OKOTech! Thanks for all your help, suggestions and discussions, which even date back to seven years ago! Thanks for helping me with the experiments in OKOTech, explaining the operation of the system and inviting me for mahjong!:)

Thanks to Ruud, Chris, Herman and Klaus from Twente University for broadening my scope in smart optical systems and answering all my stupid questions! It's a lot of fun to play with wavelength apart from the wavefront! I really enjoy working together with you! Thanks to Ruud for also helping me realize that I should enjoy most of my time! Thanks to Liu Feng, Tian Ye, Chang Lantian, Zhu Dan for the bicycles, dinners and your hospitality!

Thanks to Prof. Huang and Prof. Tang from Fudan University for providing me the opportunity to study in Delft since 2003. Thanks to Chris for a lot of care from time to time. Thanks to Jia Qi, Wang Yiyin, Tan Xi, Xu Jun, Huang Cong, Gong Lvyi for all your support, the happiness and the unforgettable time we've had together! Thanks to my roommate Qin Mian for the first dinner since I arrived in Holland!

Thanks to my Chinese friends in Delft — Wang Jinbing, Han Ying, Liu Xiaodong, Deng Wei, Wan Fang, Lin Yu, Lv Lin, Zhang Gang, Yu Yikun, Yang Chungkai, Yan Han, Liu Yong, Wu Rong, Jin Yanyu, Zhou Cui, Zhao Peng, Zhang Fan, Bi Yu, Wu Wanghua, Zhao Yi, Dong Yunzhi, Fang Zhen, Chen Xu, Jiang Yang, Wang Lingen, Zou Suqing, Li Peiyuan, for all your support and a lot of fun we had in dinners, basketball, badminton, Star Craft, cards, etc.

Thanks to Wei Jia for cooking for me since my ankle was broken! Thanks for training me with the guitar, which was actually the first (and the only) music instrument I can play so far. It's really fun to be your roommate, as you are always creative in making life more exciting, funny and easier! Thanks to Lu Weidong for taking me to the hospital, city hall and airport at that time! Thanks to Yuan Xiaoyu for taking care of me as well, but also for a lot of fun we had together in War Craft!:) Thanks to Li Minwei for offering me the happy place in Korvezeestraat! Thanks to Xu Wei for helping me with house-moving and be my good neighbor.

Thanks to my friends in ACSSNL (Association of Chinese Scholars and Students in the Netherlands): Zhan Hetian, Li Yunlei, Gu Yanyin, Yan Junlin, Li Dong, Li Hong, Ye Qinghua, Wan Taoping, Li Lin, Lin Kai, Zhao Yong, Yang Zhiming, Huo Feifei, Chen Yue, Nie Dalei, Gong Yiwei! It's really my pleasure to work with you and I had a very good time in those three years!

Thanks to Ms. Wang Xiali for teaching me Taiji every Monday evening, which keeps me energetic for the whole week afterwards! Thanks to my friends in the sports center for playing basketball every Saturday morning! You helped me release all the stress accumulated from the past week and get charged again!

Thanks to my friends in China: Zhang Han, Wang Jipeng, Lu Dongping, Xu Xiaodong, Liu Beirong, Zhang Yu, Wen Qing. You made me feel that I was not that far away from my home.

Thanks to Prof. Chen and Prof. Leng for inspiring me with idea of underwater AO! It's indeed a new application of AO and I am quite curious about the mystery!

Thanks to my wife for making all the way out to stay with me in my most exhausting time! Life was much harder than expected, but we still managed to build up our world full of happiness, warmth and love! Thanks to our parents for the endless care and support! Thanks for your encouragement! Thanks for giving us all the freedom! Although we are more than eight thousand kilometers away from each other, our minds are always together!

Delft, February 2011
Song Hong

Contents

Acknowledgements	vii
1 Introduction	1
1.1 Need for AO	1
1.2 Principles of AO	3
1.2.1 WFS-based AO	3
1.2.2 WFSless AO	6
1.3 Control of closed-loop AO systems	8
1.3.1 Control of WFS-based AO systems	8
1.3.2 Control of WFSless AO systems	15
1.4 Motivation and goal of this thesis	18
1.5 Main contributions	20
1.6 Outline of the thesis	20
2 Model-based control in a WFS-based AO system	23
2.1 Introduction	23
2.2 Problem formulation	25
2.3 Strategy	25
2.4 Identification of the AO system	29
2.4.1 Hysteresis compensation for the PDM	29
2.4.2 Identification of the linearized AO system	32
2.5 Model-based controller design	35
2.6 Experimental setup	38
2.6.1 Setup description	38
2.6.2 Measurement noise	42
2.6.3 Timing of the setup	43
2.7 Experiments and results	44

2.7.1	Hysteresis compensation	44
2.7.2	Identification of the linearized AO system	45
2.7.3	Performance of the closed-loop AO system	48
2.7.4	Computational time	49
2.8	Conclusion	49
3	Hysteresis compensation for a PDM in a WFSless AO system	59
3.1	Introduction	59
3.2	Experimental setup	61
3.3	Principles	63
3.3.1	Hysteresis reconstruction	63
3.3.2	Hysteresis compensation	65
3.4	Experimental results	66
3.4.1	Single-loop hysteresis reconstruction	66
3.4.2	Multi-loop hysteresis reconstruction	69
3.4.3	Identification of the inverse hysteresis model	71
3.4.4	Hysteresis compensation	71
3.5	Conclusion	74
4	Model-based control in a WFSless AO system	77
4.1	Introduction	77
4.2	System analysis	79
4.3	Model-based aberration estimation and correction	81
4.3.1	Modeling of the WFSless AO system	81
4.3.2	Aberration estimation and correction	83
4.4	Experimental setup	87
4.5	Experiments and results	90
4.5.1	System calibration	90
4.5.2	Modeling of the nonlinear AO system	91
4.5.3	Aberration correction	91
4.5.4	Computational complexity	96
4.6	Conclusion	96
5	Conclusions and Recommendations	97
5.1	Conclusions	97
5.2	Recommendations	98
	Bibliography	101

List of Abbreviations	109
List of Publications	111
Summary	113
Samenvatting	115
Curriculum Vitae	117

Introduction

In many scientific and medical applications, such as ground-based telescopes, scanning-type microscopes and laser systems, adaptive optics (AO) systems are used to improve the image resolution or the laser beam quality, by actively sensing and correcting the wavefront aberration in the optical path.

This thesis investigates how to improve the performance of the closed-loop AO systems by accurate modeling of the AO systems and advanced model-based controller design. Before we dive into all the details of the investigation, this chapter introduces the fundamentals on AO systems, summarizes the state-of-the-art in closed-loop AO control, discusses the limitations of existing approaches and motivates this thesis. More specifically, the following questions are answered:

- Why we need AO (Section 1.1)? How AO works (Section 1.2)?
- What is the state-of-the-art in AO control (Section 1.3)?
- What are the shortcomings of existing AO controllers (Section 1.4)?
- What is the goal of this thesis and how is the goal achieved (Section 1.4)?
- What are the main contributions of the thesis (Section 1.5)?

At the end of this chapter, the outline of the thesis is given in Section 1.6.

1.1 Need for AO

High-resolution images and high-quality light beams are sought for in many scientific and medical applications, such as ground-based telescopes, scanning-type

microscopes and laser systems [1–4]. The optics in these instruments is usually designed in such a sophisticated way that the diffraction of light [5] is expected to be the only limiting factor of the image resolution or the beam quality. According to Rayleigh’s criterion, the diffraction-limited angular resolution of an optical imaging system with a circular aperture of diameter D_a is given by [5]

$$\sin \theta = 1.22 \frac{\lambda}{D_a}, \quad (1.1)$$

where λ is the wavelength of light under observation and θ is the angular resolution in radians. In certain cases, super-resolution images are even expected with the image resolution better than the one given in Eq. (1.1) [4].

However, in practice, the aberration introduced by the transmission medium becomes the main limiting factor for the image resolution or the beam quality. For instance, the atmospheric disturbance around the earth modifies the refractive index of the air and distorts the wavefront as well as the intensity of light passing through it [1–3]. When one observes a distant star with a ground-based telescope, only blurred images of the star can be obtained (see Figure 1.1 (a) for an illustration). Although the resolution of the telescope is expected to improve with D_a , i.e., smaller θ for larger D_a , the atmospheric disturbance limits the angular resolution of the ground-based telescopes to about 1 arcsec in the near infrared range [1]. This corresponds to the diffraction-limit resolution of a telescope with a diameter of only 10 to 20 cm. What’s worse, since the atmosphere-induced aberration changes with time due to the wind or the temperature variation in the air, images taken at different time instants also differ from each other. This makes it even more challenging to get a sharp and reliable image through the atmospheric disturbance.

In 3-dimensional (3D) scanning-type fluorescence microscopes, such as confocal microscopes and multi-photon microscopes, the image is formed by scanning each point in the specimen, not only on its surface but also deep inside. In that case, one attempts to focus the illuminating beam at a target point inside the specimen, and collect light emitted by the fluorophore from the same point [4]. When the illuminating beam and the emitted light pass through the volume above the scanned point, the refractive index variation in the illuminated volume introduces aberration to the optical path. The detected signal level is reduced and eventually the image quality is degraded.

In laser systems, the laser heating modifies the temperature distribution within the laser resonator and its refractive index [6]. As a consequence, the output laser beam is distorted and can not reach its full brightness.

The specific reasons for image-quality or beam-quality degradation are different in these applications, e.g., due to the atmosphere, the specimen or the laser heating, but there is a common need for correcting the medium-induced aberration in the optical path. Adaptive optics (AO) is just a promising solution for this.

1.2 Principles of AO

This section briefly explains the fundamental principles of two commonly used closed-loop AO systems: one is used in the ground-based telescopes for rejecting the atmospheric disturbance, and the other is used in 3D scanning-type microscopes to compensate for the specimen-induced wavefront aberration. These two closed-loop AO systems mainly differ in their sensors for wavefront aberration measurement and, as a consequence, the control algorithms for aberration correction. Controller designs for the closed-loop AO systems are dug in depth in Section 1.3. Since AO is a rapidly developing area, the introduction to the closed-loop AO systems in this section intends to provide a background information on how closed-loop AO system works in general. For an extensive overview on the closed-loop AO systems, readers may refer to, e.g. [1–3].

1.2.1 WFS-based AO

The working principle of the closed-loop AO system used in ground-based telescopes [1–3] is illustrated in Figure 1.1. When light from a distant star in the space travels through the atmosphere, the wavefront of light is disturbed by the atmospheric disturbance. As light enters the AO system, it is reflected by the deformable mirror (DM) and the beam splitter, and directed to the wavefront sensor (WFS). The WFS converts the wavefront of light into a measurement vector, e.g., a Shack-Hartmann WFS converts the local gradients of the wavefront to the spots displacement in the CCD/CMOS image sensor. The measurement is fed to the controller. The controller reconstructs the wavefront from the WFS measurement, compares the reconstructed wavefront to a reference plane wavefront and computes the control signal to the DM, such that the DM deforms its surface to counter-act the wavefront aberration. Because the wavefront measurement, control signal computation and wavefront correction are implemented in closed-loop and in real-time, both the spatial and temporal variations in the wavefront aberration are tracked and corrected. Images with higher resolution are then achieved by the science camera, when compared to the those obtained without AO (see Figure 1.2).

Because the closed-loop AO systems in ground-based telescopes employ one or more WFSs for wavefront sensing, this type of closed-loop AO systems are referred to as WFS-based AO systems in this thesis. A most commonly-used WFS is the Shack-Hartmann (S-H) WFS. The working principle of the S-H WFS is illustrated in Figure 1.3. The S-H WFS consists of an array of microlens and a camera. The incident light illuminates the microlens array and each microlens focuses light in its focal plane as a single spot. The image sensor (e.g., the CCD sensor or CMOS sensor) of the camera is placed in the focal plane of the microlens array such that the pattern of the focal spots is captured and sent to the control computer for image processing. When the incident beam has a plane wavefront, the spots are located in the optical axis of each microlens (i.e., the center of each square in Figure 1.3). However, if the wavefront of the beam is aberrated, then the spots deviate from their nominal positions horizontally and/or vertically. By

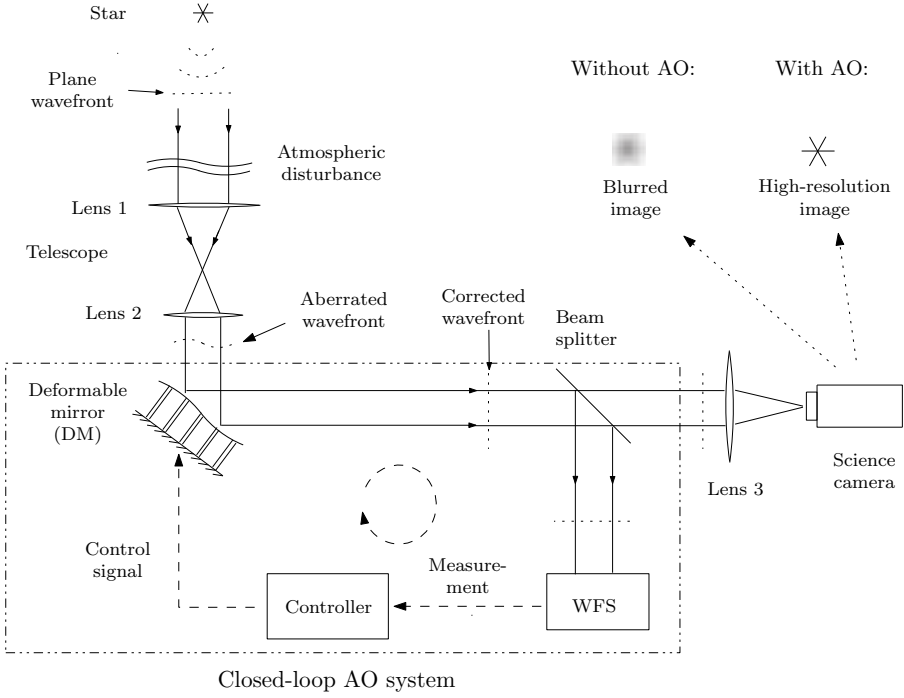


Figure 1.1: Working principle of a closed-loop AO system used in ground-based telescopes for rejecting the atmospheric disturbance. The initial plane wavefront of light is disturbed by the atmospheric disturbance. The DM surface is conjugate to the disturbance layer by Lens 1 and 2 in the telescope for efficient wavefront aberration correction. With the closed-loop AO system operated in real time, the dynamic wavefront aberration is corrected and a high-resolution image is achieved by the imaging system (Lens 3) and the science camera. The image is blurred if without AO.

comparing the aberrated spot pattern with the nominal pattern, the spot deviation is determined, which also represents the local gradients/slopes of the aberrated wavefront.

Denote the wavefront at time k as a discrete signal $\phi(k) \in \mathbb{R}^{n_f}$ with dimension n_f and the spot deviation as $s_\nu(k) \in \mathbb{R}^{n_s}$ with dimension n_s (n_s is twice the number of the spots), then $\phi(k)$ and $s_\nu(k)$ are related by

$$s_\nu(k) = G_w \phi(k) + \eta_\nu(k), \quad (1.2)$$

where $G_w \in \mathbb{R}^{n_s \times n_f}$ is the geometry matrix determined by the geometry of the microlens array. Measurement noise $\eta_\nu(k)$ has zero-mean, white and uncorrelated with $\phi(k)$. With G_w and $s_\nu(k)$ available, the wavefront can be reconstructed as

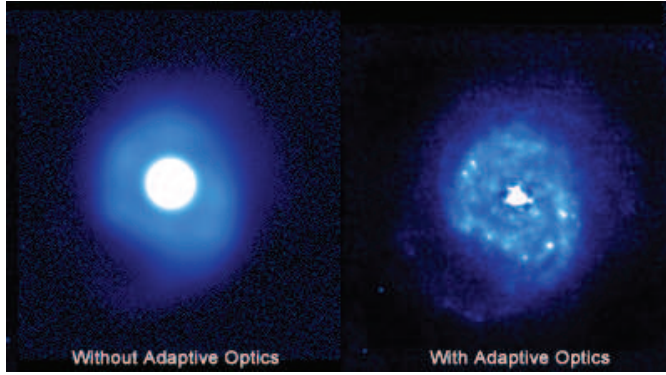


Figure 1.2: The nuclear region of the nearby galaxy NGC 7469, without and with AO. The resolution of the image has been improved significantly by AO and the details can be visualized. Image courtesy: Center for Adaptive Optics (CfAO), University of California (<http://cfao.ucolick.org/ao/why.php>).

[7–9]

$$\hat{\phi}(k) = (G_w^T G_w)^{-1} G_w^T s_\nu(k), \quad (1.3)$$

where $\hat{\phi}(k)$ is the reconstructed wavefront and G_w has full column rank. Because the wavefront reconstruction method in Eq. (1.3) is sensitive to the measurement noise, particularly at low intensity level, the wavefront is also reconstructed as [10–12]

$$\hat{\phi}(k) = (G_w^T C_\phi G_w + C_\eta)^{-1} G_w^T C_\eta s_\nu(k), \quad (1.4)$$

where $C_\phi = \varepsilon\{\phi^T(k)\phi(k)\}$ and $C_\eta = \varepsilon\{\eta_\nu^T(k)\eta_\nu(k)\}$ are the covariance matrices of $\phi(k)$ and $\eta_\nu(k)$, respectively. The operator $\varepsilon\{\cdot\}$ represents the expectation of the stochastic signal.

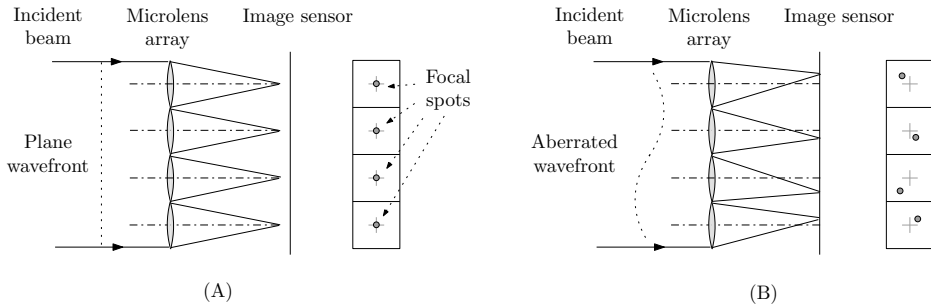


Figure 1.3: Principle of the S-H WFS. The local gradients/slopes of the aberrated wavefront are translated into the spots displacement in the image sensor.

1.2.2 WFSless AO

The working principle of the closed-loop AO systems used in the 3D scanning-type confocal microscopes is illustrated in Figure 1.4. The collimated illumination beam is focused to a single point (Point A in the figure) inside the specimen by the objective lens. The fluorescent molecules (also called fluorophore) within the illumination cone is excited by the illumination light and fluorescence is emitted. The emitted fluorescence is collected by the objective lens, filtered by the Dichroic beam splitter and focused into a pin hole by Lens 2. The pin hole is optically conjugate to Point A, to eliminate out-of-focus signal. A photon-detector is placed right behind the pin hole to measure light intensity. Scanning is achieved by either moving the specimen with a translation stage or steering the illumination beam with tip/tilt mirrors. Images of different layers of the specimen are then formed by scanning each point in the specimen in 3D.

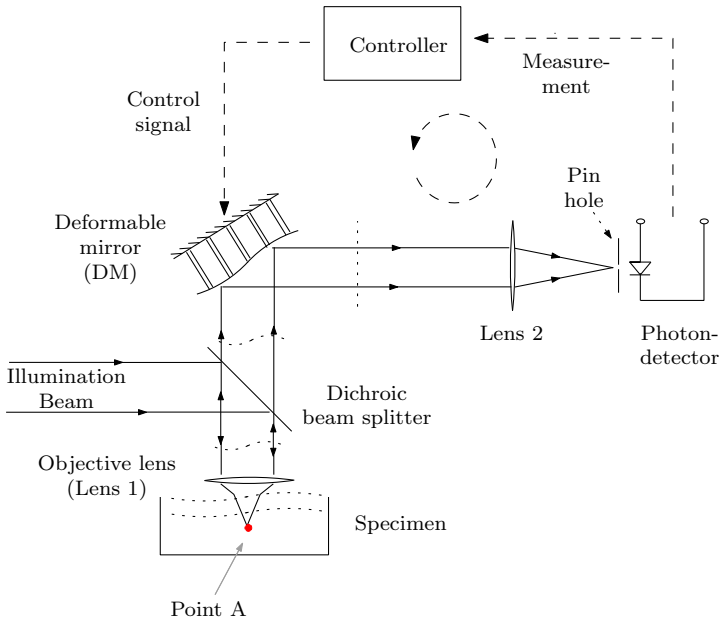


Figure 1.4: Working principle of a WFSless AO system used in the 3D scanning-type microscope for compensating the specimen-induced wavefront aberration. A photon-detector (e.g., a photodiode) is employed instead of a WFS and aberration is corrected by maximizing the intensity measurement.

In the ideal case when the specimen does not introduce any aberration to the illumination light or the emitted fluorescence, all the fluorescence emitted at Point A is focused into the pin hole and the intensity measurement reaches its maximum (see Figure 1.5). However, in practice, due to the refractive index variation in the illumination cone above Point A, both the wavefront and the amplitude of the emitted fluorescence is distorted. As a consequence, the fluorescence from Point

A can not be completely focused into the pin hole by Lens 2 and the measured intensity is reduced.

With the closed-loop AO system equipped, the DM manipulates the distorted wavefront of light collected by the objective lens. The intensity measurement is fed into the controller and the control signal to the DM is calculated. Since only the intensity measurement is available for feedback control, the closed-loop AO system in Figure 1.4 is referred to as a WFSless AO system in this thesis.

By physical modeling [13], the resulting light intensity measurement $y(k)$ is related to the incident wavefront aberration and the DM deformation as

$$U_i(\xi, \eta, k) = a_i(\xi, \eta, k) \exp \left[-j \frac{2\pi}{\lambda} (\phi_x(\xi, \eta, k) + \phi_m(\xi, \eta, k)) \right], \quad (1.5)$$

$$I(\alpha, \beta, k) = \left| \underbrace{\iint_{\Sigma_1} U_i(\xi, \eta, k) \exp \left[-j \frac{2\pi}{\lambda d} (\alpha \xi + \beta \eta) \right] d\xi d\eta}_{U_f(\alpha, \beta, k) = \mathcal{F}\{U_i(\xi, \eta, k)\}} \right|^2, \quad (1.6)$$

$$y(k) = S_\lambda \iint_{\Sigma_2} I(\alpha, \beta, k) d\alpha d\beta + \nu_1(k). \quad (1.7)$$

Here (ξ, η) and (α, β) represent the coordinates in the input plane and the focal plane of the Lens 2, respectively, and with $j = \sqrt{-1}$. The complex optical field in the input plane of the Lens 2 at discrete time instant k is represented by $U_i(\xi, \eta, k)$ (see Eq. (1.5)), with $a_i(\xi, \eta, k)$ the amplitude and $\phi_x(\xi, \eta, k) + \phi_m(\xi, \eta, k)$ the phase. $\phi_x(\xi, \eta, k)$ is the incident wavefront aberration and $\phi_m(\xi, \eta, k)$ is the wavefront manipulation by the DM. λ is the wavelength of light.

Lens 2 makes a Fourier transform on the input field $U_i(\xi, \eta, k)$ and the resulting optical field in its focal plane is represented as $U_f(\xi, \eta, k)$, i.e., $U_f(\xi, \eta, k) = \mathcal{F}\{U_i(\xi, \eta, k)\}$ where $\mathcal{F}\{\cdot\}$ denotes the Fourier transform. The intensity distribution in the focal plane of Lens 2 is represented as $I(\alpha, \beta, k)$, which is the square of the magnitude of $U_f(\xi, \eta, k)$. Here d is the focal distance of Lens 2. Σ_1 represents the illuminated area of Lens 2.

Eq. (1.7) gives the measurement from the photodiode behind the pin hole, which is an integral of the intensity $I(\alpha, \beta, k)$ over the pin hole aperture Σ_2 , multiplied by the sensitivity of the photodiode at λ (denoted as S_λ). $\nu_1(k)$ is the measurement noise, imposing a limit on the signal-to-noise ratio of the system.

Static nonlinearity is visible in Eq. (1.6) in the transfer from the complexity optical field to its magnitude. The wavefront-intensity mapping is surjective (i.e., different wavefronts can give the same intensity measurement) and not invertible, therefore a unique wavefront can not be obtained from a single intensity measurement. Aberration is corrected by maximizing the intensity measurement $y(k)$.

Investigations have been made to reconstruct the wavefront from multiple intensity measurements for efficient aberration correction. This topic is discussed in details in Section 1.3 and the contribution of the thesis on this topic is presented in Chapter 4.

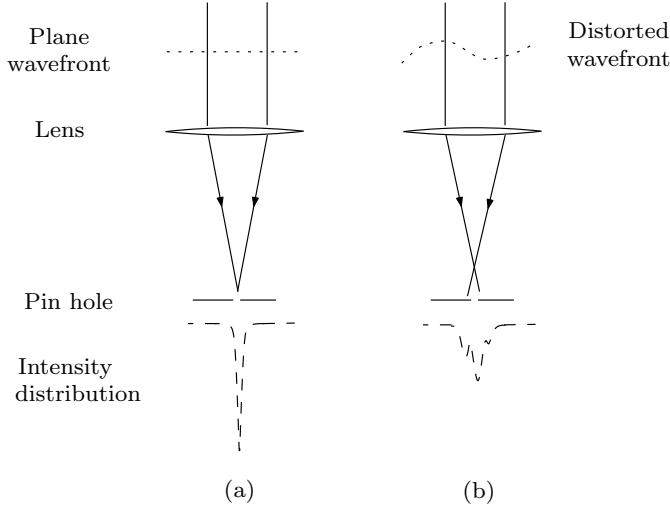


Figure 1.5: The intensity distribution in the focal plane of the lens depends on the wavefront of the incident light: (a) light with plane wavefront is focused at the focal point of the lens, which results in the highest intensity measurement from the pin hole; (b) the intensity spreads widely over the focal plane of the lens due to the wavefront aberration, which degrades the intensity measurement from the pin hole.

1.3 Control of closed-loop AO systems

Fundamentals of the WFS-based and WFSless closed-loop AO systems have been explained in previous section. This section digs into the control of both AO systems and gives an overview on the state-of-the-art in AO control. This survey is by no means exhaustive, but rather provides the insight in the limitations of existing control approaches which may be further improved, as well as the rapid developments in the past decades.

1.3.1 Control of WFS-based AO systems

Classical control approach

The block diagram of a WFS-based closed-loop AO system is shown in Figure 1.6. The incident beam with wavefront distortion $\phi(k) \in \mathbb{R}^{n_f}$ (n_f is the dimension of the discrete wavefront $\phi(k)$) at time instant k is reflected by the DM, which provides the wavefront manipulation by $\phi_m(k) \in \mathbb{R}^{n_f}$. The reflected beam, with a residual wavefront distortion $\epsilon_\phi(k) = \phi(k) - \phi_m(k)$ enters the WFS and the WFS measurement is corrupted by measurement noise $\eta(k) \in \mathbb{R}^{n_y}$ with dimension n_y . The WFS measurement is denoted as $\epsilon_y(k) \in \mathbb{R}^{n_y}$. Based on $\epsilon_y(k)$ and the model of the WFS and the DM, the controller reconstructs the wavefront $\epsilon_\phi(k)$ as $\hat{\epsilon}_\phi(k)$

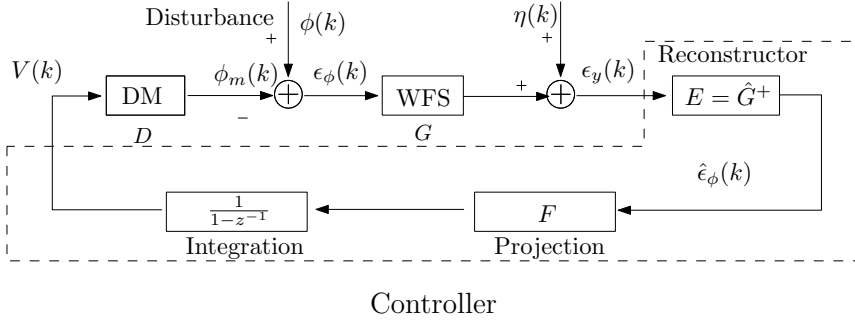


Figure 1.6: Block diagram of the WFS-based closed-loop AO system.

and determines the control voltage $V(k) \in \mathbb{R}^{n_a}$ to the DM such that $\phi(k)$ is compensated. Since $V(k)$, $\epsilon_y(k)$, $\phi_m(k)$, $\phi(k)$ are all multi-dimensional signals, the AO system is essentially a multi-input multi-output (MIMO) system. The control objective of the closed-loop AO system is to minimize the variance of the residual wavefront error $\hat{\epsilon}_\phi(k)$ (note that the offset in the $\hat{\epsilon}_\phi(k)$ does not influence the image quality), i.e.,

$$\min_{V(k)} \text{var}(\hat{\epsilon}_\phi(k)), \quad (1.8)$$

where $\text{var}(\hat{\epsilon}_\phi(k))$ is variance of $\hat{\epsilon}_\phi(k)$.

In the conventional control approach, it is assumed that the DM is a linear device and the sampling rate of the closed-loop AO system is far below the resonance frequency of the DM, so that the DM is considered linear static. The wavefront manipulation $\phi_m(k)$ is related to the control voltage $V(k)$ by

$$\phi_m(k) = DV(k), \quad (1.9)$$

where matrix $D \in \mathbb{R}^{n_f \times n_a}$ represents the linear static mapping between $V(k)$ and $\phi_m(k)$. The WFS is considered linear with one-sample delay, satisfying

$$\epsilon_y(k+1) = G\epsilon_\phi(k) + \eta(k+1), \quad (1.10)$$

where $G \in \mathbb{R}^{n_y \times n_f}$ is the geometry matrix of the microlens array in the WFS.

The reconstructor estimates the residual wavefront aberration from the WFS measurement as

$$\hat{\epsilon}_\phi(k+1) = \underbrace{\hat{G}^+}_E \epsilon_y(k+1), \quad (1.11)$$

where $\hat{\epsilon}_\phi(k+1) \in \mathbb{R}^{n_f}$ denotes the reconstructed wavefront. The reconstruction matrix $E \in \mathbb{R}^{n_f \times n_y}$ is obtained as $E = \hat{G}^+$, where \hat{G} is the estimation of G and \hat{G}^+ is the pseudo inverse of \hat{G} , i.e., $\hat{G}^+ = (\hat{G}^T \hat{G})^{-1} \hat{G}^T$ with \hat{G} full column rank.

After the residual wavefront aberration $\hat{e}_\phi(k+1)$ is reconstructed, the increment on the control voltage (denoted as $\Delta V(k+1)$) is calculated as

$$\Delta V(k+1) = F\hat{e}_\phi(k+1), \quad (1.12)$$

$$F = \hat{L}^+ = (\hat{L}^T \hat{L})^{-1} \hat{L}^T. \quad (1.13)$$

Here the matrix $F \in \mathbb{R}^{n_a \times n_f}$ projects the wavefront $\hat{e}_\phi(k+1)$ to the control voltage space. Matrix $L \in \mathbb{R}^{n_f \times n_a}$ represents the linear mapping from $V(k)$ to $\hat{e}_\phi(k)$, given by

$$L = EGD. \quad (1.14)$$

The estimation of L is denoted as \hat{L} . Eq. (1.13) gives a linear least-square (LLS) fitting from $V(k)$ to $\hat{e}_\phi(k)$.

Since the WFS only measures the residual wavefront aberration after the DM correction, $\Delta V(k+1)$ is only the increment over the previous voltage $V(k)$. The voltage at time $k+1$ is then updated as

$$V(k+1) = V(k) + \mu \Delta V(k+1) = V(k) + \underbrace{\mu F E}_{\hat{e}_\phi(k+1)} \epsilon_y(k+1). \quad (1.15)$$

Eq. (1.15) is essentially an integrator, with μ the integral gain. μ is closely related to the transient response and the convergence speed of the closed-loop AO system. μ is defined by the user during controller design and $\mu = 1$ yields fastest convergence at the expense of low stability robustness.

Eq. (1.15) provides the optimal update law with respect to the 2-norm of the residual wavefront error under the conditions that [14–16]:

1. The transfer from $V(k)$ to $\hat{e}_\phi(k)$ is linear and quasi-static with pure one-sample delay, such that it is represented as

$$\hat{e}_\phi(k+1) = LV(k). \quad (1.16)$$

2. The disturbance $\phi(k)$ is an integrated white noise process, which can be represented as

$$\phi(k) = \frac{1}{1 - z^{-1}} p_\nu(k), \quad (1.17)$$

where $p_\nu(k)$ is a white and stationary random process with zero-mean and unit covariance and z is the shift operator.

However, these conditions are not always satisfied in practice. For instance, as the sampling rate increases in modern AO systems, the DM dynamics becomes more significant and the assumption on the quasi-static DM is not valid any more. Since piezo-driven DM (PDM) are widely in AO systems, the nonlinearity in the PDM (e.g., hysteresis) also limits the accuracy of the linear AO model and degrades the

closed-loop bandwidth. The atmospheric disturbance usually is not an integrated white noise process but, e.g., follow a $f^{-\frac{2}{3}}$ power law before a cut-off frequency of tens of Hz [17]. What's more, the statistics of the atmospheric disturbance even varies with the time, e.g., due to the variation in wind speed or in air temperature distribution. In modern large-scale AO systems, the high dimension of the sensor and control signals impose a challenge for efficient wavefront reconstruction and control signal generation within limited time. All these have motivated intensive investigations on the model-based control, adaptive control, efficient wavefront reconstruction algorithms and distributed control, as will be explained in the following parts.

Modal gain optimization

The basic idea of the modal gain optimization approaches proposed by [18, 19] is to represent the wavefront of the disturbance, DM and the residual error in certain basis such that each mode is decoupled. Therefore the MIMO AO system is decomposed into multiple single-input single-output (SISO) systems and each SISO system is independent to each other. An integrator is designed for each SISO system and the gain of each integrator is tuned independently to make a balance among the residual modal error, system stability and closed-loop bandwidth.

Model-based control approaches

Due to the inherent delay in digital control systems, e.g, sample delay, computational delay, the DM always corrects the wavefront aberration one or more samples later than the disturbance. The concept behind model-based control is that the performance of the closed-loop AO system would be optimal if the AO system were known perfectly and the disturbance could be predicted beforehand. The performance of the closed-loop AO system with model-based controller strongly depends on the accuracy of the disturbance model and the AO model. In reality, optimal performance can never be achieved due to the uncertainty in the model and the statistics of the disturbance. However, investigations have shown that the performance of the closed-loop AO system has still been improved by incorporating accurate AO model and disturbance model in the controller.

Paschall and Anderson [20] were one of the first to design the linear quadratic Gaussian (LQG) controller for a closed-loop AO system. The controller aims at minimizing the variance of the residual wavefront error, by incorporating the model of the DM, WFS and the disturbance. In their work, each actuator in the DM is assumed to be linear and the dynamics of each actuator is decoupled and represented as a first-order system. The DM model is then derived from the dynamics of each actuator and the steady-state response of the DM surface as

$$\dot{x}_m(t) = \mathcal{F}_m x_m(t) + \mathcal{B}_m u_m(t), \quad (1.18)$$

where $x_m(t)$ is composed of the first 14 Zernike coefficients describing the wavefront manipulation by the DM surface and $u_m(t)$ is the control voltage to the DM.

The matrix $\mathcal{F}_m = \text{diag}(a_m, \dots, a_m) \in \mathbb{R}^{14 \times 14}$ (a_m is a parameter determined by the structure of the DM) represents the dynamics of the DM and

$$\mathcal{B}_m = -a_m \mathcal{M}_m \quad (1.19)$$

contains the steady-state influence matrix of the DM, \mathcal{M}_m . The WFS is assumed to have a pure one-sample delay. The disturbance model is also represented by the first 14 Zernike modes. Each Zernike coefficient is obtained in 3 steps: (1) an autocorrelation kernel of the Zernike coefficients is obtained, which assumes the disturbance has the Kolmogorov spectrum; (2) the kernel is evaluated to generate the autocorrelation data; (3) the generated data is fit to a first-order Markov process for each Zernike coefficient. With the models of the DM, WFS and disturbance available, a LQG controller is designed to minimize the residual wavefront error and the performance of the resulting closed-loop AO system is verified by simulation.

Looze [21] proposed a LQG controller with the wavefront represented in the Karhunen-Loève basis. By this representation, all Karhunen-Loève modes are geometrically orthogonal to each other and uncorrelated. The controller for the MIMO AO system is decomposed into n_c modal controllers, where n_c is the number of modes to be controlled. Each modal controller is scalar and discrete-time. In the AO model, the DM dynamics is neglected and only the computational delay in the loop is accounted for. The disturbance is also decomposed in n_c modes, where each modal coefficient is approximated by an autoregression and moving average (ARMA) model. Each ARMA model is identified by fitting the model to the measurement data in an open-loop observation. In his later work [22], the AO model is built by modeling the DM dynamics as a first-order lag filter, the camera in the WFS as an integration process, and taking into account the exposure time of the camera and the computational delay. In [23], a hybrid model is built which represents both the discrete AO system and the continuous incident disturbance. A hybrid LQG controller is then designed based on the hybrid model and the closed-loop performance is evaluated.

Roux [24] has extended the LQG controller design to the multi-conjugate AO (MCAO) systems, where the wavefront aberration in different layers of the atmosphere is sensed by several WFSs and DMs. In the controller design, the DM is considered as linear and quasi-static except for a pure one-sample delay, i.e.,

$$\phi_m(k) = A_m u(k-1), \quad (1.20)$$

where $u(k-1)$ is the input to the DM at time $k-1$ and $\phi_m(k)$ is the wavefront manipulation by the DM at time k . Matrix A_m is the influence matrix of the DM. The disturbance is modeled by a first-order autoregressive (AR) model as

$$\phi_d(k+1) = A_p \phi_d(k) + \nu_2(k), \quad (1.21)$$

where $\phi_d(k)$ is the disturbance at time k , represented in Zernike modes. Matrix A_p contains both the temporal and spatial characteristics of the disturbance. A_p is diagonal and its elements have been adjusted to enforce a correlation time decreases

with the Zernike radial order. $\nu_2(k)$ is a white noise. Based on the AO model and the disturbance model, the LQG controller is designed, which consists of a Kalman filter estimating the incident disturbance and a static state feedback law. The same modeling and controller design strategy is employed by Petit [25, 26] and the performance improvement of the resulting closed-loop AO system have been demonstrated in laboratory experiments at a closed-loop sampling rate of 60 Hz.

Doelman [14] revealed that the conventional integrator is an optimal controller if the disturbance is an integrated white-noise process and the DM is linear and quasi-static DM. This conclusion is also drawn by Kulcsár [15]. In a recent work by Correia [27], the DM dynamics is considered in the controller design. The DM deformation is represented in certain modal basis and each modal coefficient is related to the control input by a second-order differential equation with strong oscillation and low damping. The results show that by considering the DM dynamics, both the performance and stability robustness of the closed-loop AO system is improved.

Hinnen [28–30] explored the spatial-temporal correlation in the disturbance and identified the disturbance model from the measurement data using a subspace identification approach. Since no assumption was required on the decoupling between the spatial and temporal dynamics in the disturbance, an accurate disturbance model is achieved. Concerning the AO system, apart from an integer number of sample delays, the DM is considered static and the exposure of the camera is modeled as a two-tap finite impulse response (FIR) filter. The parameters in the AO model are optimized by fitting the model output with the measurement data. Based on the disturbance model and the AO model, a H_2 optimal controller is designed and validated in the experimental setup at a closed-loop sampling rate of 25 Hz.

Adaptive control

The approaches discussed above depend on a prior knowledge on both the AO system and the disturbance statistics. However, in practice, the statistics of the disturbance may vary with time, e.g., due to the variation in the wind speed or the variation of the atmospheric temperature distribution. Therefore the nominal model used for the controller design can not accurately represent the reality and the performance of the closed-loop AO system is degraded. In this case, adaptive control strategies [16, 31–33] are explored to track the variation in the disturbance statistics and update the control algorithm in real-time.

Ellerbroek and Rhoadarmer [31] proposed a method to adaptively optimize the wavefront reconstructor of a closed-loop AO system based on the closed-loop WFS data. This method relies on the recursive least squares (RLS) algorithm to track the temporal and spatial correlations of the disturbance wavefront. The main ideas are: (1) to reconstruct the wavefront in the future from a combination of past and current wavefront sensor measurements, thus the system latency is compensated; (2) the space of the WFS measurement is split into two subspaces, i.e., the

range space of the DM actuation and its orthogonal complement. These two subspaces are completely independent of each other. Therefore open-loop prediction algorithms such as RLS can be used to optimize the second component and gives accurate prediction even in case the loop is closed. Results show a significant performance improvement over the conventional wavefront reconstructor, particularly at high wind speed.

Another adaptive control strategy has been explored by [32, 33], where the controller consists of a fixed nominal LTI controller augmented with an adaptive controller. In the adaptive controller design, the closed-loop feedback disturbance rejection problem is formulated as a feedforward disturbance rejection problem by internal model control (IMC) approach, which allows to interpret the controller design in a pseudo open-loop manner. The adaptive controller is implemented as a FIR lattice filter. The lattice gains in the lattice filters are updated by recursive least squares (RLS) algorithms. This multichannel adaptive lattice filter has superior numerical stability and efficiency, which is important for control of large-scale AO systems in real-time.

Doelman [16] proposed a batch-wise subspace predictor algorithm to adaptively predict the time-variant disturbance statistics. The Kalman gain in the predictor is determined directly from a batch of samples of the estimated disturbance by a closed-loop subspace identification algorithm. The subspace predictor is implemented by the RLS algorithm and compared with the least-mean-squares (LMS) based recursive predictor. Simulation results show that the recursive subspace predictor and the LMS algorithm obtain similar performance in a stationary situation.

Distributed control for large-scale AO systems

In the upcoming large-scale or extremely large-scale ground-based telescopes, the number of actuators and sensors in the AO systems are expected to be in the order of $10^4 - 10^5$ and the closed-loop sampling rate will be in the order of kHz. This means that the wavefront distortion should be reconstructed and the control signal to the DM be updated all within 1 ms or even less. Therefore efficient algorithms are required for wavefront reconstruction and for the controller design.

Massioni [34, 35] considers that all actuators in the DM have the identical influence on its neighboring mirror surface and each actuator is an identical subsystem in the DM. The large-scale DM is then represented as the interconnection of a number of identical subsystems, also called the decomposed system. The interconnection follows a pattern that is described by a "pattern matrix". Because each actuator in the DM can only influence a limited number of neighboring elements, the pattern matrix for the DM is a sparse matrix. By taking advantage of the sparsity in the pattern matrix, the control command to the DM is computed efficiently in a H_2 -optimal controller despite of the number of actuators in the DM.

To compensate for the delay in the control system, the disturbance wavefront is predicted in the model-based controller using the Kalman filter. Solving the

Riccati equation in the Kalman filter for large-scale systems imposes a big challenge for the efficient disturbance wavefront prediction. Fraanje [36] proposed a fast reconstruction and prediction algorithm for the disturbance wavefront based on the structured Kalman filtering. The disturbance is considered as a frozen flow with von Kármán spatial correlation and the temporal and spatial evolution of the disturbance is represented as the shift of the frozen flow in time and space. The disturbance is modeled as a string of interconnected subsystems and described by a distributed state-space model, where the system matrices in the state-space model are sparse. This sparse structure allows to solve the Riccati equation in the Kalman filter efficiently by taking advantage of the recent development in sequentially semi-separable systems (SSS) (see also [37]). The computational complexity of the resulting disturbance predictor scales with the number of subsystems N rather than N^3 as required by the centralized prediction approach.

1.3.2 Control of WFSless AO systems

The main difference between the controllers used in WFS-based AO systems and those in WFSless AO origins from the wavefront sensing components in these two AO systems. As discussed in Section 1.2, the WFS measurement in Eq. (1.2) is linear to the incident wavefront and the wavefront can be reconstructed directly, e.g., by Eq. (1.3) or Eq. (1.4). If the nonlinearity in the DM is appropriately compensated (e.g., the hysteresis in the PDM is compensated), then the controller can be designed by linear design approaches, e.g., LQG controller design, H_2 -optimal controller design. However, in WFSless AO systems, the only measurement available is the intensity within the pin hole, which, as seen from Eq. (1.6), is a nonlinear function of the wavefront aberration in the AO system. Because the nonlinear mapping is surjective, the wavefront aberration can not be determined by simply inverting the nonlinear function. The control objective in WFSless AO systems is to maximize the intensity measurement of a single point or the sharpness of the whole image, by adapting the shape of the DM, i.e.,

$$\max_{u(k)} y(k), \quad (1.22)$$

where $y(k)$ is the intensity measurement of a single point or the sharpness of the image and $u(k)$ is the control signal to the DM. Depending on whether a prior knowledge is required for intensity maximization, the control algorithms can be classified into two categories: model-free optimization algorithms and model-based algorithms.

Model-free optimization

The intensity $y(k)$ can be maximized by standard optimization algorithms, without any a prior knowledge on the aberration or on the AO system itself. Different optimization algorithms, e.g., gradient descent optimization algorithm, simplex optimization algorithm, genetic algorithm, simulated annealing algorithm, etc.,

have been used for intensity maximization in WFSless AO systems and the improvements in the performance metric have been demonstrated in [6, 38–51]. The optimization algorithms usually take hundreds of iterations to converge and the computational time is in the order of seconds or minutes.

Model-based optimization

To speed up the optimization process, models of WFSless AO systems have been incorporated in the control algorithm. Booth [52–54] made a linear approximation between the unknown aberration and the center-of-mass of a set of DM control signals, as represented by

$$a = SW, \quad (1.23)$$

$$W = \frac{\sum_{m=1}^M b_m I_m}{\sum_{m=1}^M I_m}, \quad (1.24)$$

where $a \in \mathbb{R}^N$ contains the modal coefficients of unknown wavefront aberration in the AO system, with N the number of modes. Vector $W \in \mathbb{R}^N$ is the center-of-mass of a set of DM control signals $b_m \in \mathbb{R}^N$, $m = 1, \dots, M$ (M is the number of DM control signals) where each control signal b_m is weighted by the resulting intensity measurement I_m . The control signal b_m is pre-defined before the experiments as the $N + 1$ vertices of a simplex around the origin. The intensity I_m is obtained when both b_m and a are present in the system. Matrix $S \in \mathbb{R}^{N \times N}$ is the linear mapping from W to a , which is calculated beforehand from an aberration-free physical model. Based on Eq. (1.23) and (1.24), together with $M = N + 1$ intensity measurements, the unknown aberration a is estimated.

Débarre [55–57] represented the sharpness of an image as a nonlinear function of the net wavefront aberration in the AO system. In [55], the sharpness of an image is approximated as a separable quadratic function of each Lukosz modal coefficient in the AO system, i.e.,

$$p_m = q_1 + q_2 \sum_{n=4}^{n=N+3} (a_n + b_n)^2, \quad (1.25)$$

where $p_m \in \mathbb{R}$ is the sharpness of the image. q_1 and q_2 are the coefficients of the quadratic function. N is the number of modes. $a_n \in \mathbb{R}$ is the n th Lukosz modal coefficient of the unknown wavefront aberration. b_n is the n th Lukosz modal control command to the DM. Since p_m is a quadratic function of each modal coefficient a_n and a_n is independent from each other, each a_n can be estimated from 3 performance metric evaluations when 3 modal commands $-b_n$, 0 and b_n are assigned to the DM. In total, the unknown wavefront aberration is estimated from $2N + 1$ measurements.

The requirement that each mode is separable in Eq. (1.25) is released in [56], where the performance metric is generalized as a quadratic function of the aber-

ration of the system, i.e.,

$$p_m = p_0 - a_q^T A a_q. \quad (1.26)$$

Here p_0 is a parameter. Vector $a_q \in \mathbb{R}^N$ contains the modal coefficients of the wavefront aberration and the positive semi-definite matrix A describes the coupling between all modes. Taking an eigenvalue decomposition of A gives

$$A = A_1 \Lambda A_1^T, \quad (1.27)$$

where Λ is diagonal matrix with the eigenvalues of A in the diagonal. A_1 contains the eigenvectors of A . Substituting Eq. (1.27) into (1.26) results in

$$p_m = p_0 - a_q^T A_1 \Lambda A_1^T a_q = p_0 - b_q^T \Lambda b_q \quad (1.28)$$

with $b_q = A_1^T a_q$ the new modal coefficient vector after the coordinate transformation. Because Λ is diagonal matrix, all elements in b_q are decoupled and the performance metric can be written as a separable quadratic function of each modal coefficient as in Eq. (1.25). Wavefront aberration is estimated from $2N + 1$ measurements as well.

1.4 Motivation and goal of this thesis

This thesis focuses on controller design for closed-loop AO systems. The reasons are two-fold. On one hand, advanced controller design helps to get the most performance out of the fixed AO system hardware. As shown in Section 2,3,4 of this thesis, the performance of closed-loop AO systems is improved by accounting for the hysteresis in the DM, the dynamic in the AO system and the nonlinear model of the intensity measurement. On the other hand, research in controller design also suggests or inspires modifications in system hardware (e.g., changing the number of sensors or their locations). By iteratively enhancing the system hardware and software, the overall system performance is improved.

Based on the literature survey in Section 1.3, some limitations of existing controllers are summarized below.

- WFS-based AO controllers

In WFS-based AO controllers, attention has paid in modeling the statistics of the disturbance, e.g., by approximating the disturbance as frozen layers or by the data-driven subspace identification approach, etc., but the model of the deterministic AO system is less focused, particularly the dynamics and nonlinearity in the AO system.

- Dynamics

The AO system is mostly considered quasi-static with pure integer number of sample delays [25,26,28–30], for the reason that the time constant of the DM is much smaller than the sampling period of the AO system and the loop delay (e.g., integration time of the WFS camera, data transmission time, computational time of the controller) takes integer number of sampling periods. As the sampling rate increases in modern AO systems, the dynamics in the AO system can not be neglected.

The dynamics of the AO system has been modeled as a scalar transfer function, assuming that all the actuators in the DM have the identical dynamics and their dynamics are decoupled. Since the AO system is essentially a multi-input multi-output (MIMO) system and the actuators in the DM are all coupled, the scalar transfer function representation may not give an accurate description of the AO dynamics. What's more, the dynamic AO models are parameterized from first-principles. The parameters are either obtained directly from the individual component models which may not give an accurate AO model as a whole, or optimized to fit the measurement data where the convergence is not guaranteed and computation can be very demanding.

- Nonlinearity

Piezo-driven DMs (PDMs) [58], bimorph DMs [59–61], electromagnetic DMs [62, 63] and micro-electro-mechanical-system (MEMS) DMs [64–66] are commonly used in AO systems. Because PDMs are able to provide large amplitude wavefront manipulation required by atmospheric disturbance rejection, they have been widely used in many closed-loop

AO systems and are to be used in some upcoming closed-loop AO systems [67–70]. However, the hysteresis in the PDM limits the accuracy of the linear AO model. If hysteresis is not accounted for, then the performance of the closed-loop AO system will be degraded.

- WFSless AO controller

Most of the controllers in WFSless AO systems use model-free standard optimization algorithms, which usually take hundreds of iterations to converge. Booth and Débarre [52–57, 71] have incorporated the model of the WFSless AO system into the control algorithm and sped up the aberration correction process significantly, i.e., $N + 1$ intensity measurements required by a linear model and $2N + 1$ measurements required by a quadratic model. The linear model in [52, 53] is a first-order approximation of the nonlinearity in the AO system and holds only for small aberrations around the operational point. Débarre decouples the influence of each aberration mode on the performance metric and makes use of the quadratic relationship between the performance metric and each modal coefficient. But the parameters in the quadratic relationship have not been used for aberration estimation yet. If the full information on the WFSless AO system (i.e., both the nonlinear structure and the parameters) is used, then the convergence speed of the WFSless AO can be further improved.

Apart from this, the dynamics in the aberration has not been touched yet. As shown in WFS-based AO systems, the performance of WFS-based closed-loop AO systems have been improved significantly by properly modeling the disturbance and predicting the disturbance in the controller. Therefore, by taking the aberration model into account in the controller design, the convergence speed of WFSless AO systems is expected to be improved as well.

According to the analysis above, the goal of the thesis is stated as follows:

Goal: To demonstrate that the performance of the closed-loop AO systems can be improved by accurate modeling of the AO systems and model-based controller design. More specifically,

- the nonlinearity and the dynamics in the high-sampling-rate WFS-based AO system with PDM should be accounted for during the model identification and controller design;
- the static nonlinearity of the WFSless AO system should be identified and an efficient model-based approach be developed.

By this goal, it is shown that model-based control can not only improve the performance of AO systems with linear wavefront measurement, but also those with limited sensor information (e.g, only the intensity measurement is available in WFSless AO systems). The effectiveness of model-based control in AO is then demonstrated and proved in a general sense.

1.5 Main contributions

The main contributions of the thesis are summarized briefly as follows:

- In WFS-based AO systems, an integrated approach has been proposed and validated to reject the disturbance. This makes high performance AO control design accessible to the new developments in control relevant modeling and identification. Nonlinearity in the PDM is modeled and compensated, enabling the use of existing linear system identification and controller design approaches for control of high-sampling-rate closed-loop AO systems.
- A novel method is proposed to extract hysteresis in PDMs from nonlinear intensity measurements of WFSless AO systems. Based on the extracted hysteresis curve, an inverse hysteresis model is identified to compensate for the hysteresis in the PDM. This reduces the uncertainty in AO systems significantly.
- In WFSless AO systems, an efficient approach has been proposed and validated for wavefront aberration correction, only based on the model of the WFSless AO system and a minimum number of $N + 2$ intensity measurements. Although dynamics is not considered in the AO model nor in the disturbance model, this pioneering work still gives a convincing demonstration that the aberration can be corrected efficiently in WFSless AO systems by model-based control.
- Two closed-loop AO experimental setups have been developed to validate the proposed control strategies. The experimental validations prove that the proposed control strategies are not only efficient in improving the system performance, but also tractable on modern computers, which is vital for real-time implementation of closed-loop AO systems.

1.6 Outline of the thesis

This thesis consists of five chapters. Apart from the introduction, the rest of the thesis is organized as follows (see Figure 1.7).

- Chapter 2 focuses on model-based controller design for a closed-loop AO system with PDM and high-sampling-rate WFS. Since the hysteresis in the PDM adds to the uncertainty in the AO system, hysteresis compensation is necessary to reduce this uncertainty and improve the model accuracy. The hysteresis in PDM is compensated by inverse hysteresis models. A linear dynamic model of the AO system is then identified by closed-loop subspace identification algorithm. A controller is designed based on the models of the AO system and the disturbance. The performance of the closed-loop AO system with the proposed controller is evaluated by experiments and compared with conventional controller. Experimental results show that the

variance of the residual error has been reduced by 30% by the proposed controller. This chapter is based on the papers below:

- **H. Song**, R. Fraanje, G. Schitter, G. Vdovin and M. Verhaegen, "Hysteresis compensation for a piezo deformable mirror", in *Proceedings of the Sixth International Workshop on Adaptive Optics for Industry and Medicine*, pages 112-117, Ireland, 2007.
- **H. Song**, R. Fraanje, G. Schitter, G. Vdovin and M. Verhaegen, "Modeling and control of a nonlinear dynamic adaptive optics system", invited paper, in *2010 IFAC Symposium on Mechatronic Systems*, Boston, 13-15 Sep., 2010.
- **H. Song**, R. Fraanje, G. Schitter, G. Vdovin and M. Verhaegen, "Controller design for a high-sampling-rate closed-loop adaptive optics system with piezo-driven deformable mirror", accepted by *European Journal of Control*, Special Issue on Adaptive Optics Control for Ground Based Telescopes.
- Chapter 3 describes how to compensate for the hysteresis in the PDM in a WFSless AO system. Since the intensity measurement in the WFSless AO system contains both hysteresis and memoryless nonlinearity originating from the optical system, hysteresis is first extracted from the intensity measurement, and then used for inverse hysteresis model identification. The approach has been validated by experiments. The results in this chapter have been published in
 - **H. Song**, G. Vdovin, R. Fraanje, G. Schitter, and M. Verhaegen, "Extracting hysteresis from nonlinear measurement of wavefront-sensorless adaptive optics system", *Opt. Lett.* **34**(1), 61-63 (2009).

and presented in

- **H. Song**, R. Fraanje, G. Schitter, G. Vdovin, and M. Verhaegen, "Hysteresis compensation in a wavefront-sensor-less adaptive optics system", presented in *the Seventh International Workshop on Adaptive Optics for Industry and Medicine*, Moscow, Russia, 8-11 June, 2009.
- Chapter 4 explores how to correct the wavefront aberration in a WFSless AO system by model-based control. The model of the WFSless AO system is identified from the input-output data of the AO system, using a black-box identification approach. The wavefront aberration is estimated by solving a nonlinear least squares (NLLS) problem online, based on the model of the WFSless AO system and a minimum number of $N + 2$ intensity measurements (N is the number of considered aberration modes). This approach is validated in an experimental setup with 20 static aberrations having Kolmogorov spatial distributions. By correcting $N = 9$ Zernike modes, an intensity improvement from 49% of the maximum value to 89% has been achieved in average based on $N + 5 = 14$ intensity measurements. With the lowest initial intensity, an improvement from 17% of the maximum value to 86% has been achieved based on $N + 4 = 13$ intensity measurements. This chapter is based on the paper

- H. Song, R. Fraanje, G. Schitter, H. Kroese, G. Vdovin, and M. Verhaegen, "Model-based aberration correction in a wavefront-sensor-less adaptive optics system", *Opt. Express*, **18**(23), 24070-24084 (2010).

- Chapter 5 concludes the thesis and gives recommendations for future work.

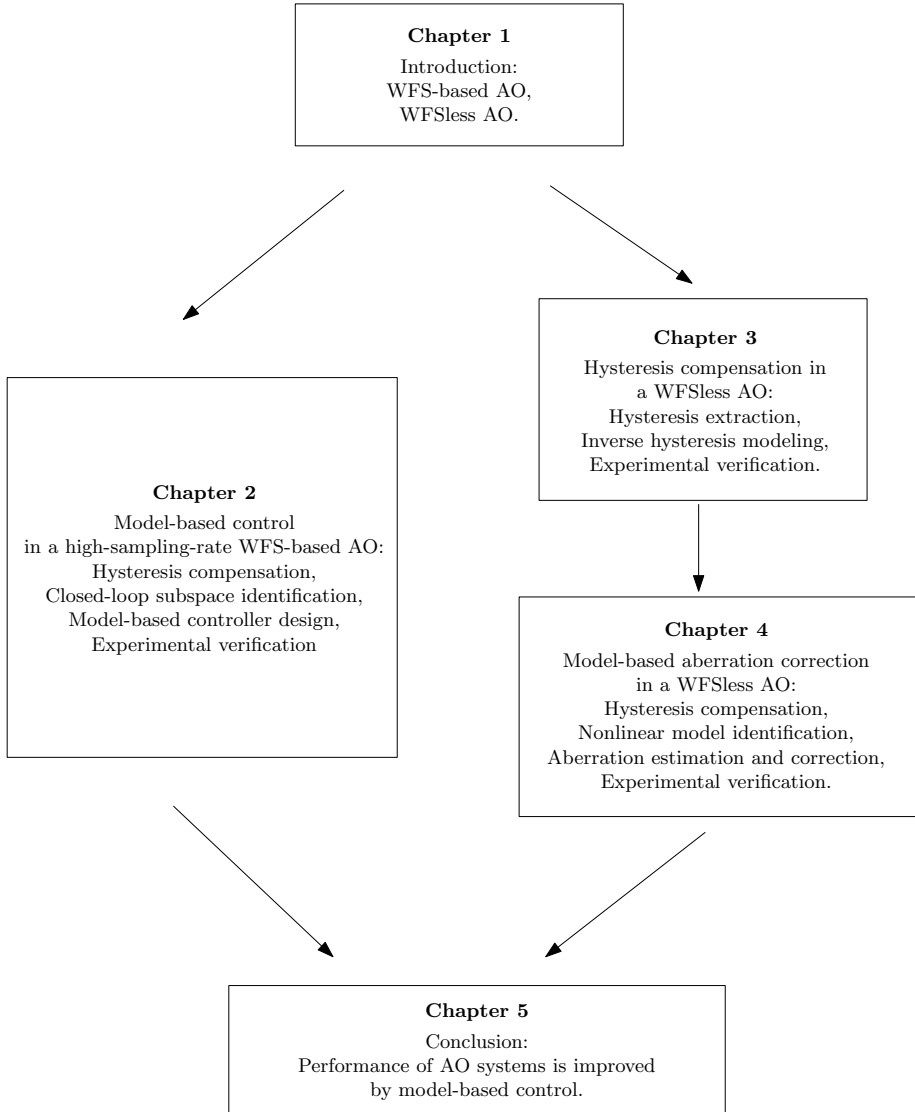


Figure 1.7: Structure of the thesis. This thesis demonstrates that the performance of closed-loop AO systems is improved by model-based control.

Model-based control in a WFS-based AO system

This chapter aims at improving the performance of a closed-loop AO system with piezo-driven deformable mirror (PDM) and high-sampling-rate wavefront sensor (WFS) by means of model-based control. The improvement is achieved by reducing the hysteresis in the PDM with a hysteresis compensator and identifying a linear dynamic model of the AO system from the measurement data with a closed-loop subspace identification approach. Based on the identified model of the AO system and the model of the disturbance, a dynamic controller is designed. Experimental results show that the variance of the residual error of the proposed closed-loop AO system has been reduced by 30% with respect to the conventional AO control approach.

2.1 Introduction

The resolution of many optical imaging systems, like telescopes, microscopes, is limited by the diffraction of light [5]. However, in most practical cases, the optical aberration in the light path is the dominant limitation of the resolution of the imaging system. Therefore in many scientific and medical applications, such as astronomy, laser systems and microscopy, adaptive optics (AO) systems have been widely used to improve the image quality, by actively sensing and compensating the optical aberration in the system [2, 3].

Conventional closed-loop AO controllers [2, 3] consists of a linear static gain, the pseudo-inverse of the deformable mirror (DM) influence matrix, and an integrator. The gain is tuned to make a trade-off among disturbance rejection, noise amplification and closed-loop stability [18, 19]. To further improve the performance of the closed-loop AO system, controllers based on both the deterministic AO model and the stochastic model of the disturbance have been proposed

[15,20,23–25,30]. Performance improvement of such closed-loop AO systems have been demonstrated in laboratory experiments by [25] and [30], at a closed-loop sampling rate of 60 Hz and 25 Hz, respectively. As the sampling rate increases in modern AO systems [67], the dynamics of the AO system becomes more significant and an accurate dynamic model of the AO system is important for model-based controller design. Looze [23] built a dynamic model of the AO system based on the dynamic models of the DM and the wavefront sensor (WFS), and evaluated the performance improvement of the closed-loop AO system by simulation. Chiuso [72] applied a closed-loop subspace identification approach for the AO system based on the measurement data. Because the identification process is based on real data without assumption on the sampling rate of the AO system, the accuracy of the model of the AO system is improved.

In this chapter we continue the line of improving the performance of a closed-loop AO system with nonlinear piezo-driven DM (PDM) and high-sampling-rate WFS by means of model-based control. Apart from PDMs, bimorph DMs [59–61], electromagnetic DMs [62,63] and DMs based on microelectromechanical systems (MEMS) technology [64–66] have also been used or proposed in many closed-loop AO systems. A PDM is considered in this thesis because PDMs are able to provide large amplitude wavefront manipulation required by atmospheric disturbance rejection and have been widely used [67–70]. Furthermore, the nonlinearity in the PDM (e.g., the hysteresis) makes the controller design even more challenging in large-amplitude-disturbance rejection. By demonstrating controller design for a PDM, our controller design strategy is also applicable to other types of DMs.

The main contribution of this chapter is to make high performance AO control design accessible to the new developments in control relevant modeling and identification [72,73]. This is reflected in two aspects: (1) nonlinearity in the PDM is modeled and compensated, enabling the use of existing linear system identification and controller design approach for control of high-sampling-rate closed-loop AO system; (2) the controller and the model are validated by evaluating the performance of the closed-loop AO system in the experimental setup. The investigation is carried as follows. First, the hysteresis in the PDM is reduced by a hysteresis compensator using feedforward control [60,61]. By doing this, the linearity of the AO system is improved even in case of large-amplitude control signal. Second, a linear dynamic model of the AO system is identified using a closed-loop subspace identification approach [72]. Because the experimental condition for identification is close to that for closed-loop operation, a realistic model of the AO system is identified for controller design [73]. Third, a dynamic controller is designed based on the identified model of the AO system and a disturbance model. Fourth, the performance of the closed-loop AO system with the proposed controller is evaluated experimentally. Comparison is also made in closed-loop performance between the proposed controller and the conventional controller.

This chapter is organized as follows. Section 2.2 formulates the problem and the strategy is proposed in Section 2.3. Section 2.4 focuses on identification of the AO system, followed by model-based controller designed in Section 2.5. Section 2.6 describes the experimental setup, which validates the strategy for controller design. The experimental results on AO system identification and the closed-loop

performance are reported in Section 2.7. Section 2.8 concludes this chapter.

2.2 Problem formulation

The schematic of the common closed-loop AO system [2,3,74] under investigation is shown in Figure 2.1. The collimated laser beam passes through the beam splitter (BS) first, then reflected by the DM and directed to the Shack-Hartmann (S-H) WFS. The S-H WFS transfers the local gradients of the incident wavefront to the spot displacements in the CCD camera, denoted as $y(k) \in \mathbb{R}^{m_y}$ with m_y the number of measurements at time instant k . The disturbance, denoted as $d(k) \in \mathbb{R}^{m_y}$, is introduced numerically in the computer after the measurement, to have a good control of the disturbance. Disturbance $d(k)$ is generated by $d(k) = D(z)s(k)$, where $s(k) \in \mathbb{R}^{m_s}$ (m_s is the dimension of $s(k)$) is a white and stationary random process with zero-mean and unit covariance. Filter $D(z)$ shapes both the temporal dynamics and the spatial range of $d(k)$, with z the shift operator (it should be noted that the filter $D(z)$ is different from the matrix D in Figure 1.6 where D represents the static DM model). Based on the residual error $e(k) = d(k) - y(k)$, the voltages $V(k) \in \mathbb{R}^{m_u}$ (m_u is the number of actuators) are generated by the controller to drive the DM such that the disturbance is rejected. The control objective is

$$\min_{V(k)} \text{var}(e), \quad (2.1)$$

where $\text{var}(e)$ is the variance of the residual error $e = d - y$.

The model-based controller would give the optimal closed-loop performance (i.e., minimal $\text{var}(e)$ in Eq. (2.1)) if the models of the AO system and the disturbance statistics were perfect and the controller is properly designed. Therefore the problem is how to identify an accurate model of the AO system accounting for the nonlinear in the PDM and the dynamics in the AO system.

2.3 Strategy

To have an accurate model of the AO system for controller design, the nonlinearity in the PDM, the high sampling rate in the WFS and the experimental conditions under which the data is collected should be considered during the identification.

Creep and hysteresis are two common nonlinearities in the PDM, originating from the piezo-actuators [60,61,75]. Creep can be considered as the drifting in the actuators which is observed when fixed DM deformation is required over extended periods of time, e.g. in the order of tens of seconds [75]. Since the time scale when creep takes effect is much longer than the sampling interval of the closed-loop AO system, creep can be neglected in closed-loop operation.

Hysteresis can be considered as a static nonlinearity occurring at the input of the PDM, between the applied electrical field and the displacement of the piezo

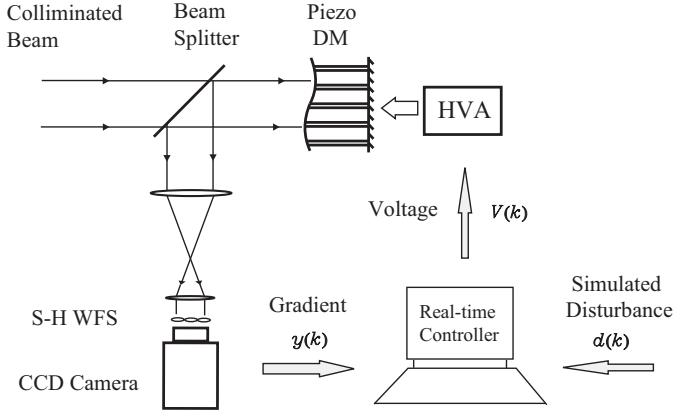


Figure 2.1: Schematic of the closed-loop AO system under investigation (HVA: high voltage amplifier). Disturbance $d(k)$ is introduced numerically in the computer after the measurement, to have a good control on the disturbance.

actuators [75]. Hysteresis becomes significant when the PDM is driven by a voltage source with stroke in the order of micro-meters. In PDM all the piezo actuators are coupled, for instance, by the face plate and the substrate of the DM. During the operation of the PDM, apart from the linear mechanical coupling between piezo actuators, additional electrical charge may also be induced in the piezo actuators due to the piezo-electric effect [76], e.g., when certain piezo actuator is subject to the mechanical stress from neighboring actuators; however, this induced electrical charge will be absorbed by the driving power electronics in a very short time. In our setup, the output impedance of the high voltage amplifier is about $5\text{ K}\Omega$, the capacitance of the piezo-actuator is less than 10 nF and the time constant of the RC loop is less than $50\text{ }\mu\text{s}$. This means that the induced charge in the piezo-actuator reduces to about 36.8% of its initial value in less than $50\text{ }\mu\text{s}$, which is negligible compared with the sampling interval of the WFS, e.g., 4 ms . Therefore the coupling between the piezo actuators in the DM is considered only in mechanical domain and the hysteresis in each piezo-actuator in the DM is considered independent. The AO system can then be thought of as a Hammerstein-type nonlinear system [77] with hysteresis at its input followed by linear dynamics at its output, represented as (see Figure 2.2)

$$h_i(k) = H(V_i(k)), \quad (2.2)$$

$$y(k) = G(z)h(k), \quad (2.3)$$

where $V_i(k)$ and $h_i(k)$ are the voltage and displacement of the i th piezo actuator at time instant k , respectively. Each actuator is considered to have identical hysteretic behavior, which is represented as $H(\cdot)$. The actuator displacement vector $h(k)$ is constructed as

$$h(k) = [h_1(k) \quad h_2(k) \quad \cdots \quad h_{m_u}(k)]^T. \quad (2.4)$$

The linear transfer from $h(k)$ to $y(k)$ is denoted by $G(z)$.

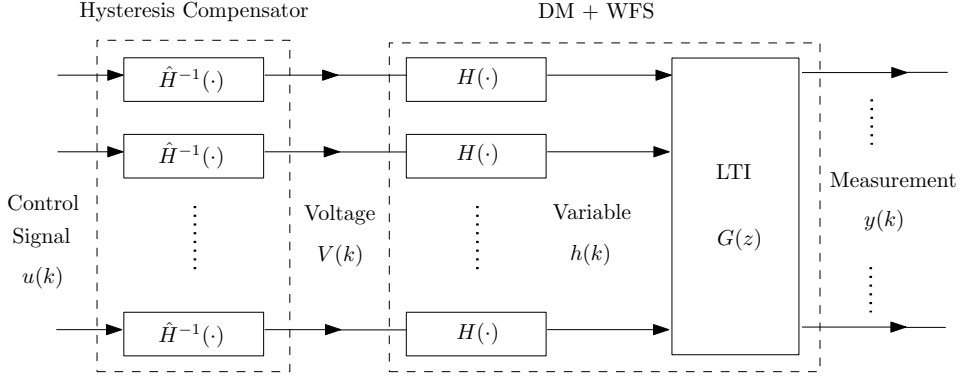


Figure 2.2: Block diagram of the conceptual open-loop AO system, including the hysteresis compensator, DM and WFS. The input of the AO system is the control signal $u(k)$ and the output is the measurement $y(k)$. By hysteresis compensation, the transfer from $u(k)$ to $y(k)$ is expected to be linear.

Hysteresis in the PDM can be compensated by different approaches. For instance, Kudryashov [59] compensated for hysteresis of a bimorph mirror by applying harmonic signal with decreasing amplitude to the piezo actuator each time before a new control voltage is assigned. Essentially this method initializes the piezo actuator to a certain state each time before the new action, which requires extra samples and thus limits the effective sampling rate of the system. Chang [78] used strain gauges, temperature sensors and feedback control to linearize each piezo actuator in a segmented DM, where the temperature sensor is used to remove the effect of temperature variation on the strain gauge. This scheme requires both hardware and software modification, adding to the complexity of the closed-loop AO system. Yang [60] corrected the hysteresis of a bimorph mirror by feed-forward linearization with an enhancing Coleman-Hodgdon inverse hysteresis model. Dubra [61] also reduced the hysteresis of a single-actuator bimorph mirror with a classical and a generalized Preisach inverse hysteresis model. Compared with [59] and [78], the work in [60] and [61] indicates a more cost-effective approach for hysteresis compensation (HC) in AO systems because it only requires a mathematical model instead of any hardware modification or extra samples in the control, but meanwhile provides efficient correction on hysteresis.

Concerning the linear dynamics of the AO system, as already discussed before, the closed-loop subspace identification approach proposed in [72] allows to identify the model of the AO system without the static-DM assumption or the individual models of the DM and WFS, therefore suitable for identification of the AO system with high sampling rate as in our case. Apart from that, since the data for identification is collected in closed-loop operation, the experimental condition for data collection is close to that for normal operation. Realistic model for controller design can be expected.

The identification of the AO system can be summarized as follows.

- Compensate for the hysteresis in the PDM by feedforward control as shown in Figure 2.2, where the hysteresis in each piezo actuator is compensated by the inverse hysteresis model identified from the measured hysteresis data. During the experiment, the PDM should be excited by slowly varying inputs with large amplitude such that the dynamics in the PDM can be neglected while the hysteresis is excited. The hysteresis compensator should be validated by evaluating the linearity from the control signal $u(k)$ to the measurement $y(k)$.
- After HC in the previous step, a dynamic model of the linear AO system (transfer from $u(k)$ to $y(k)$, denoted as $G(z)$) can be identified at high sampling rate with a closed-loop subspace identification approach [72]. The disturbance in the identification experiment should be designed such that the dynamics in the linear AO system is excited persistently.
- With the identified model of the AO system and the model of the simulated disturbance, the controller can be designed.

This strategy leads to the block diagram of the closed-loop AO system in Figure 2.3, where the hysteresis compensator $\hat{H}^{-1}(\cdot)$ is placed before the DM to reduce the hysteresis and a linear controller $C(z)$ is designed to take care of the linear part of the AO system.

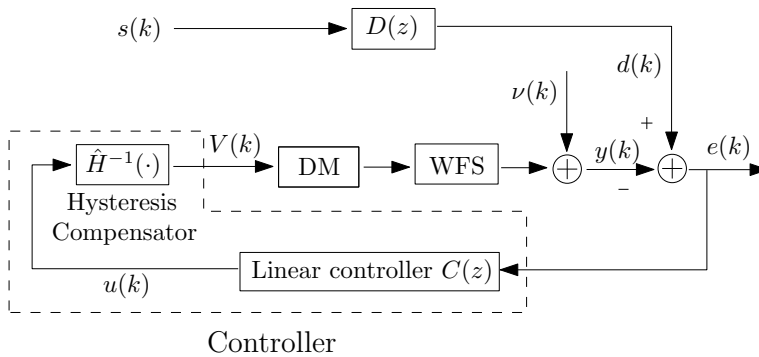


Figure 2.3: Block diagram of the closed-loop AO system. The measurement noise is denoted as $\nu(k)$. The proposed controller consists of a hysteresis compensator $\hat{H}^{-1}(\cdot)$ and a linear controller $C(z)$. Note that the filter $D(z)$ is different from the matrix D in Figure 1.6, where D represents the static DM model.

2.4 Identification of the AO system

According to the strategy proposed in previous section, the model of the AO system is identified in two steps: (1) hysteresis compensation for the PDM; (2) identification of the linearized AO system.

2.4.1 Hysteresis compensation for the PDM

Because the hysteresis in each piezo actuator is considered independent during the DM operation, the hysteresis in the PDM can be reduced by compensating for hysteresis in piezo actuators separately. Referring to Figure (2.2), the hysteresis compensator consists of m_u single-input single-output (SISO) inverse hysteresis models, one for each piezo actuator. Each inverse hysteresis model takes one channel of the control signal as input and computes the voltage as output. Now the problem becomes how to identify the inverse hysteresis model to compensate for the hysteresis in the piezo actuator.

The identification of the inverse hysteresis model involves parameterization of the model and parameter optimization. Concerning the model structure, Holman [79] used separate polynomials to fit the hysteresis branches in the measurement data. As an generalization of the polynomial curve-fitting, Coleman-Hodgdon equations [60, 80, 81] are also used to capture the hysteresis branches. Since these two approaches do not take into account the input amplitude variations, the accuracy is limited [75]. Compared with these two, Preisach models [61, 75, 82–84] have more general structure and are very effective in capturing both the amplitude variations and non-symmetry in the hysteresis of the piezo-actuator. Therefore in this thesis Preisach inverse hysteresis model is considered. Here it should be noted that Preisach hysteresis model and Preisach inverse hysteresis model share the same model structure, but the input and output for these two models are interchanged during the model identification and only the parameters are different in these two models. Since there have been intensive investigations on the Preisach inverse hysteresis model as mentioned above, only the numerical implementation of the Preisach inverse hysteresis model is described briefly in this chapter from the user's point of view. Readers may also refer to, e.g. [75, 82, 84], for a detailed theoretical description.

In Preisach inverse hysteresis model, the congruency and wiping-out properties are assumed. The congruency property states that all inverse hysteresis loops with the same input extrema are congruent. The wiping-out property means that the output of the Preisach inverse hysteresis model at time instant k (denoted as $\tilde{V}(k)$) depends not only on the input $\tilde{u}(k)$ but also on the past dominant local input extrema. Here $\tilde{u}(k)$ and $\tilde{V}(k)$ can be looked as the scalar version of $u(k)$ and $V(k)$, respectively. Denote the past dominant local input maxima and minima as α_j and β_j , respectively, $j = 1, \dots, n_e$ (n_e is the number of the (α_j, β_j) pairs), then α_j and β_j should satisfy $\alpha_1 > \alpha_2 > \dots > \alpha_{n_e}$ and $\beta_1 < \beta_2 < \dots < \beta_{n_e}$. If a new local maximum α' (or local minimum β') appears which is larger than the last n_l number of α_j (or smaller than the last n_l number of β_j), then the last n_l pairs of

(α_j, β_j) are wiped out from the (α, β) sequence and the last pair of the new sequence is updated as $\alpha_{n_e - n_l} = \alpha'$ (or $\beta_{n_e - n_l} = \beta'$). By the wiping-out property, memory in the inverse hysteresis loop has been reflected in the model.

To explain how the output of the Preisach model is computed, let's consider the input-output trajectory in Figure 2.4, where the input $\tilde{u}(k)$ varies as $\beta_1 \rightarrow \alpha_1 \rightarrow \beta_2 \rightarrow \alpha_2 \rightarrow \tilde{u}_5$ and the input-output trajectory follows $P_1 \rightarrow P_2 \rightarrow P_3 \rightarrow P_4 \rightarrow P_5$. Here β_1 and β_2 are the dominant local minima, and α_1 and α_2 are the dominant local maxima. The output of the Preisach model at input \tilde{u}_5 is determined by

$$\tilde{V}_5 = \tilde{V}_1 + \Delta\tilde{V}_1 - \Delta\tilde{V}_2 + \Delta\tilde{V}_3 - \Delta\tilde{V}_4. \quad (2.5)$$

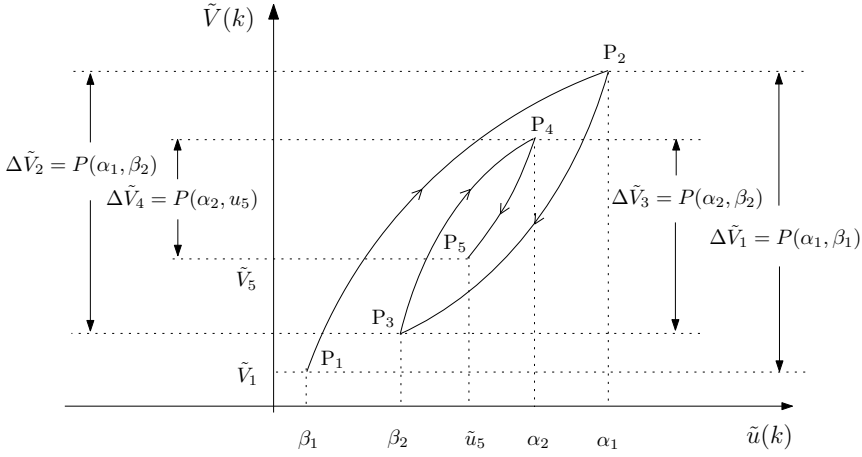


Figure 2.4: Illustration of the numerical implementation of Preisach inverse hysteresis model. Input $\tilde{u}(k)$ varies as $\beta_1 \rightarrow \alpha_1 \rightarrow \beta_2 \rightarrow \alpha_2 \rightarrow \tilde{u}_5$, with dominant local minima β_1 and β_2 and dominant local maxima α_1 and α_2 . The input-output trajectory follows $P_1 \rightarrow P_2 \rightarrow P_3 \rightarrow P_4 \rightarrow P_5$. $\tilde{V}(k)$ is computed by: (1) determining the dominant local extrema $\{\alpha_j, \beta_j\}_{j=1}^{n_e}$; (2) evaluating the Preisach functions $P(\alpha, \beta)$.

According to the congruency property of the Preisach model, any $\Delta\tilde{V}$ corresponding to certain input extrema α and β can be calculated as $\Delta\tilde{V} = P(\alpha, \beta)$, where $P(\alpha, \beta)$ is called the Preisach function. Equation (2.5) can thus be written as

$$\tilde{V}_5 = \tilde{V}_1 + P(\alpha_1, \beta_1) - P(\alpha_1, \beta_2) + P(\alpha_2, \beta_2) - P(\alpha_2, \tilde{u}_5) \quad (2.6)$$

$$= \tilde{V}_1 + \sum_{i=1}^2 P(\alpha_i, \beta_i) - \sum_{i=1}^1 P(\alpha_i, \beta_{i+1}) - P(\alpha_2, \tilde{u}_5). \quad (2.7)$$

Here \tilde{u}_5 is treated the same way as a local minima in the Preisach function evaluation.

From the description above, it can be seen that the output of the Preisach model

is calculated mainly in two steps: (1) determining the dominant local input extrema $\{\alpha_j, \beta_j\}_{j=1}^{n_e}$; (2) evaluating the Preisach function $P(\alpha, \beta)$. The dominant local input extrema are determined by logic operations according to the wiping-out property as described above. For online implementation of the Preisach model as in the closed-loop AO system, $\{\alpha_j, \beta_j\}_{j=1}^{n_e}$ should be stored in the computer memory and updated with the input $\tilde{u}(k)$. The Preisach function $P(\alpha, \beta)$ is usually identified from the first-order reversal hysteresis curves. Based on the collected data, a look-up table can be made, or more generally, $P(\alpha, \beta)$ can be approximated by some basis functions, for instance, neural network (NN) [85], hinging hyperplane [86,87], etc. In this thesis, $P(\alpha, \beta)$ is approximated by a two-layer neural network consisting of n_Q tangent hyperbolic-neurons in the first layer and one neuron in the second layer with input (α, β) and output $P(\alpha, \beta)$ (see Figure 2.5). The output of the neural network is determined by the following equation:

$$P(\alpha, \beta) = W_L \tanh \left(W_I \begin{bmatrix} \alpha \\ \beta \end{bmatrix} + b_1 \right) + b_2, \quad (2.8)$$

where $W_I \in \mathbb{R}^{n_Q \times 2}$ and $W_L \in \mathbb{R}^{1 \times n_Q}$ contain the input and output weights of the NN, respectively; $b_1 \in \mathbb{R}^{n_Q \times 1}$ and $b_2 \in \mathbb{R}$ are biases on the input and output neurons, respectively. Parameters W_I , W_L , b_1 and b_2 are obtained by minimizing the estimation error in the Preisach function (i.e. training the NN).

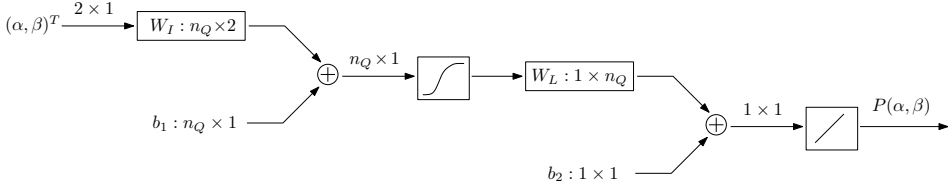


Figure 2.5: Schematic representation of a two-layer neural network with input (α, β) and output $P(\alpha, \beta)$.

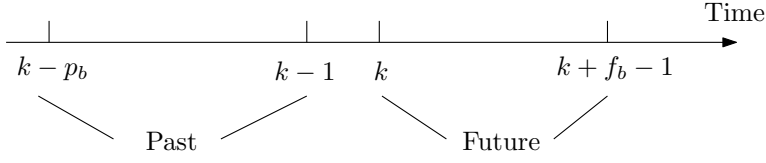


Figure 2.6: Illustration of the past and future horizons. The past horizon contains p_b time instants and the future contains f_b .

2.4.2 Identification of the linearized AO system

After hysteresis compensation of the PDM, the transfer from the control input $u(k)$ to the sensor output $y(k)$ is considered linear and a linear dynamic model is identified for the controller design.

In the predictor-based subspace identification (PBSID_{opt}) algorithm [72], the linear AO system is represented in the innovation form as

$$x(k+1) = Ax(k) + Bu(k) + K\epsilon(k), \quad (2.9)$$

$$y(k) = Cx(k) + \epsilon(k), \quad (2.10)$$

where $u(k) \in \mathbb{R}^{m_u}$, $y(k) \in \mathbb{R}^{m_y}$ and $x(k) \in \mathbb{R}^{m_x}$ are the input, output and state variable of the state space model at time instant k , respectively. $A \in \mathbb{R}^{m_x \times m_x}$, $B \in \mathbb{R}^{m_x \times m_u}$, $C \in \mathbb{R}^{m_y \times m_x}$ are the system matrices with m_x the order of the system. $K \in \mathbb{R}^{m_x \times m_y}$ is the Kalman gain. The innovation signal $\epsilon(k) \in \mathbb{R}^{m_y}$ is the one-step-ahead linear prediction error of $y(k)$, defined as

$$\epsilon(k) = y(k) - Cx(k). \quad (2.11)$$

Here the direct feedthrough term from $u(k)$ to $y(k)$ is neglected, accounting for the inherent sample delay in the digital control system.

Substituting Eq. (2.11) into (2.9), we have the closed-loop observer form as

$$x(k+1) = \underbrace{(A - KC)}_{\bar{A}} x(k) + Bu(k) + Ky(k), \quad (2.12)$$

$$y(k) = Cx(k) + \epsilon(k). \quad (2.13)$$

Matrix $\bar{A} = A - KC$ is assumed to be stable and the system be controllable and observable.

The matrices A , B , C and K are identified in three steps: (1) the Markov parameters are estimated from the block Hankel matrices by solving a least squares problem; (2) the states of the system are estimated from Markov parameters and the Hankel matrices; (3) A , B , C and K are identified based on the Markov parameters, the Hankel matrices and the states of the system by solving two least squares problems.

Estimation of Markov parameters

Denote the past and future horizons (also called the past and future windows, see Figure 2.6) as $p_b \in \mathbb{N}^+$ and $f_b \in \mathbb{N}^+$, respectively, denote $\tilde{B} = \begin{bmatrix} B & K \end{bmatrix}$, stack Eq. (2.13) for time instants $k, k+1, \dots, k+f_b-1$ in the future horizon as

$$\underbrace{\begin{bmatrix} y(k) \\ y(k+1) \\ \vdots \\ y(k+f_b-1) \end{bmatrix}}_{\mathbf{y}_{[k, k+f_b]}} = \underbrace{\begin{bmatrix} C \\ C\bar{A} \\ \vdots \\ C\bar{A}^{f_b-1} \end{bmatrix}}_{O_{f_b}} x(k) + \underbrace{\begin{bmatrix} 0 & 0 \\ C\tilde{B} & 0 \\ \vdots & \vdots \\ C\bar{A}^{f_b-2}\tilde{B} & C\bar{A}^{f_b-3}\tilde{B} & \dots & 0 \end{bmatrix}}_{T_{f_b}} \underbrace{\begin{bmatrix} u(k) \\ y(k) \\ \vdots \\ u(k+f_b-1) \\ y(k+f_b-1) \end{bmatrix}}_{\mathbf{z}_{[k, k+f_b]}} + \underbrace{\begin{bmatrix} \epsilon(k) \\ \epsilon(k+1) \\ \vdots \\ \epsilon(k+f_b-1) \end{bmatrix}}_{\mathbf{e}_{[k, k+f_b]}}. \quad (2.14)$$

Eq. (2.14) can also be written in a compact form as

$$\mathbf{y}_{[k, k+f_b]} = O_{f_b} x(k) + T_{f_b} \mathbf{z}_{[k, k+f_b]} + \mathbf{e}_{[k, k+f_b]}. \quad (2.15)$$

Note that O_{f_b} and T_{f_b} are both time-independent. Let's define the following data matrices:

$$Y_{k, f_b, n_b} = \begin{bmatrix} \mathbf{y}_{[k, k+f_b]} & \mathbf{y}_{[k+1, k+f_b+1]} & \dots & \mathbf{y}_{[k+n_b-1, k+f_b+n_b-1]} \end{bmatrix}, \quad (2.16)$$

$$X_{k, 1, n_b} = \begin{bmatrix} x(k) & x(k+1) & \dots & x(k+n_b-1) \end{bmatrix}, \quad (2.17)$$

$$Z_{k, f_b, n_b} = \begin{bmatrix} \mathbf{z}_{[k, k+f_b]} & \mathbf{z}_{[k+1, k+f_b+1]} & \dots & \mathbf{z}_{[k+n_b-1, k+f_b+n_b-1]} \end{bmatrix}, \quad (2.18)$$

$$E_{k, f_b, n_b} = \begin{bmatrix} \mathbf{e}_{[k, k+f_b]} & \mathbf{e}_{[k+1, k+f_b+1]} & \dots & \mathbf{e}_{[k+n_b-1, k+f_b+n_b-1]} \end{bmatrix}, \quad (2.19)$$

where $n_b \in \mathbb{R}$ is the number of vectors being stacked in the matrices Y_{k, f_b, n_b} , $X_{k, 1, n_b}$, Z_{k, f_b, n_b} and E_{k, f_b, n_b} , i.e., the number of columns in each matrix. Combining Eq. (2.15) - (2.19), we have

$$Y_{k, f_b, n_b} = O_{f_b} X_{k, 1, n_b} + T_{f_b} Z_{k, f_b, n_b} + E_{k, f_b, n_b}. \quad (2.20)$$

Although the state $X_{k, 1, n_b}$ is unknown, the term $O_{f_b} X_{k, 1, n_b}$ can be constructed

from the past horizon as

$$O_{f_b} X_{k,1,n_b} = \underbrace{\begin{bmatrix} C\bar{A}^{p_b} \\ C\bar{A}^{p_b+1} \\ \vdots \\ C\bar{A}^{p_b+f_b-1} \end{bmatrix}}_{\mathbf{b}_x} X_{k-p_b,1,n_b} + \underbrace{\begin{bmatrix} C\bar{A}^{p_b-1}\tilde{B} & C\bar{A}^{p_b-2}\tilde{B} & \dots & C\tilde{B} \\ C\bar{A}^{p_b}\tilde{B} & C\bar{A}^{p_b-1}\tilde{B} & \dots & C\bar{A}\tilde{B} \\ \vdots & \vdots & \dots & \vdots \\ C\bar{A}^{p_b+f_b-2}\tilde{B} & C\bar{A}^{p_b+f_b-3}\tilde{B} & \dots & C\bar{A}^{f_b-1}\tilde{B} \end{bmatrix}}_{H_{p_b}} \quad (2.21)$$

$$\cdot \underbrace{\begin{bmatrix} \mathbf{Z}[k-p_b,k] & \mathbf{Z}[k-p_b+1,k+1] & \dots & \mathbf{Z}[k-p_b+n_b-1,k+n_b-1] \end{bmatrix}}_{Z_{k-p_b,p_b,n_b}}. \quad (2.22)$$

Since \bar{A} is stable as assumed, the bias \mathbf{b}_x can be neglected by choosing large p_b . Combining (2.20) and (2.22), we may derive the following relationship

$$Y_{k,f_b,n_b} \approx H_{p_b} Z_{k-p_b,p_b,n_b} + T_{f_b} Z_{k,f_b,n_b} + E_{k,f_b,n_b}. \quad (2.23)$$

Here the " \approx " sign is due to ignoring \mathbf{b}_x . The matrices H_{p_b} and T_{f_b} , also called the Markov parameters, can now be obtained by solving the following linear least squares problem

$$\min_{\Xi} \|Y_{k,f_b,n_b} - \Xi Z_{k-p_b,p_b,n_b}\|_F^2, \quad (2.24)$$

with $\Xi = \begin{bmatrix} H_{p_b} & T_{f_b} \end{bmatrix}$ and $Z_{k-p_b,p_b,n_b} = \begin{bmatrix} Z_{k-p_b,p_b,n_b} \\ Z_{k,f_b,n_b} \end{bmatrix}$.

Estimation of the states

With estimation of the Markov parameters \hat{H}_{p_b} and \hat{T}_{f_b} available, the term $O_{f_b} X_{k,1,n_b}$ can be calculated from Eq. (2.22) by ignoring \mathbf{b}_x . Compute the following singular value decomposition (SVD)

$$\hat{H}_{p_b} Z_{k-p_b,p_b,n_b} = \begin{bmatrix} U_{b_1} & U_{b_2} \end{bmatrix} \begin{bmatrix} \Sigma_{b_1} & \\ & \Sigma_{b_2} \end{bmatrix} \begin{bmatrix} V_{b_1}^T \\ V_{b_2}^T \end{bmatrix}. \quad (2.25)$$

The matrix Σ_{b_1} contains the m_x largest singular values, which corresponds to the order of the model and can be chosen by the user. The matrix O_{f_b} and the state sequence $X_{k,1,n_b}$ can now be estimated by

$$\hat{O}_{f_b} = U_{b_1} \Sigma_{b_1}^{1/2}, \quad (2.26)$$

$$\hat{X}_{k,1,n_b} = \Sigma_{b_1}^{1/2} V_{b_1}^T. \quad (2.27)$$

Identifying A , B , C and K

According to Eq. (2.9) and (2.10), the matrices A , B , C and K can be estimated (the estimation are denoted as \hat{A} , \hat{B} , \hat{C} and \hat{K} , respectively) based on $u(k)$, $y(k)$ and $\hat{X}_{k,1,n_b}$, by solving two least square problems:

$$\hat{C} = \arg \min_C \left\| Y_{k,1,n_b} - C \hat{X}_{k,1,n_b} \right\|_F^2, \quad (2.28)$$

and

$$\begin{bmatrix} \hat{A} & \hat{B} & \hat{K} \end{bmatrix} = \arg \min_{A,B,K} \left\| \hat{X}_{k+1,1,n_b-1} - \begin{bmatrix} A & B & K \end{bmatrix} \begin{bmatrix} \hat{X}_{k,1,n_b-1} \\ U_{k,1,n_b-1} \\ \hat{E}_{k,1,n_b-1} \end{bmatrix} \right\|_F^2, \quad (2.29)$$

with

$$U_{k,1,n_b-1} = \begin{bmatrix} u(k) & u(k+1) & \cdots & u(k+n_b-2) \end{bmatrix}, \quad (2.30)$$

$$\hat{E}_{k,1,n_b-1} = Y_{k,1,n_b} - \hat{C} \hat{X}_{k,1,n_b}. \quad (2.31)$$

With the estimation of A , B and C available (denoted as \hat{A} , \hat{B} and \hat{C} , respectively), the linear AO model can be constructed.

2.5 Model-based controller design

Two commonly used model-based controllers in closed-loop AO systems are LQG controller [15, 20, 23] and H_2 optimal controller [30]. In the LQG controller design proposed by [23], the LQG controller is computed by solving two algebraic Riccati equations (ARE), one for the Kalman gain design and the other for the optimal state feedback. In the H_2 optimal controller design proposed by [30], the feedback optimal controller design problem is converted to a feedforward optimal controller design problem by the internal model control (IMC) approach. The feedforward optimal controller is computed by applying the Causal Wiener Filter (CWF) theory and two AREs need to be solved as well. As proved by [88], the LQG and H_2 controller design methods result in the same input-output behavior of the controller and hence the same closed-loop performance, given the same disturbance model and AO model. Since the IMC approach used in H_2 optimal controller design allows to interpret the controller design in a pseudo open-loop manner that is commonly applied in standard AO control, the H_2 optimal controller design approach proposed in [30] and [88] is taken in this thesis.

Referring to Figure 2.3, the block diagram of the closed-loop AO system is also described in Figure 2.7 (a). The transfer from $s(k)$ to disturbance $d(k)$ and from the control signal $u(k)$ to $y(k)$ are represented by asymptotically stable rational transfer functions $D(z)$ and $G(z)$, respectively. $C(z)$ is the controller structured by

the IMC approach. In this controller, the AO model $\hat{G}(z)$ is used to reconstruct the disturbance by removing the DM modulation from the residual error, i.e., $\hat{d}(k) = e(k) + \hat{y}(k)$. Here $\hat{d}(k)$ and $\hat{y}(k)$ are the estimation of disturbance and the DM modulation, respectively. With $\hat{d}(k)$ as input, the control signal $u(k)$ is generated by the control block $W(z)$ such that the cost function

$$J = \text{tr} \mathbf{E}(e^T(k)e(k)) \quad (2.32)$$

is minimized, where $\text{tr}(\cdot)$ is the trace operator and $\mathbf{E}(\cdot)$ is the stochastic expectation operator. The control block $W(z)$ and the controller $C(z)$ are related by

$$C(z) = (I - W(z)\hat{G}(z))^{-1}W(z). \quad (2.33)$$

The problem of finding optimal feedback control block $W(z)$ to minimize Eq. (2.32) in Figure 2.7 (a) is equivalent to finding the optimal feedforward controller $W(z)$ minimizing Eq. (2.32) in Figure 2.7 (b). Here it is assumed that $\hat{G}(z) = G(z)$ and $\hat{d}(k) = d(k)$. Because $s(k)$ is a white noise process with unit covariance, the cost function J in Figure 2.7 (b) can also be written as

$$J = \text{tr} \mathbf{E}(e^T(k)e(k)) = \|D(z) - G(z)W(z)D(z)\|_2^2 \quad (2.34)$$

using Parseval's Theorem, where $\|\cdot\|_2$ represents the H_2 norm. The solution to this feedforward optimal controller design problem is given by the Causal Wiener Filter theory.

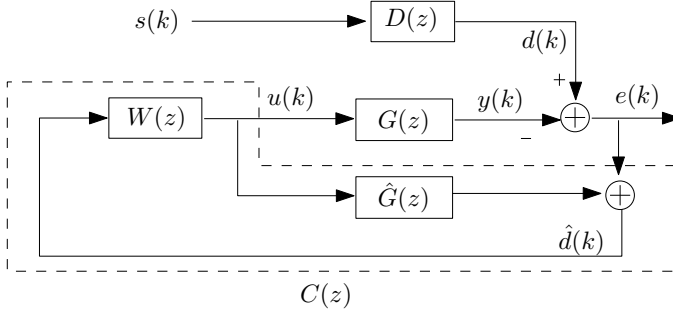
Lemma 2.1 (Causal Wiener Filter [88]) *Let $G(z)$ and $D(z)$ belong to the set of asymptotically stable rational transfer functions and assume that $G(z)$ and $D(z)$ do not lose rank $\forall |z| = 1$. Then the optimal feedforward controller $W(z)$ which is minimizing (2.34) is given by*

$$W(z) = G_o^\dagger(z) [G_i^*(z)D(z)D_{ci}^*(z)]_+ D_{co}^\dagger(z) \quad (2.35)$$

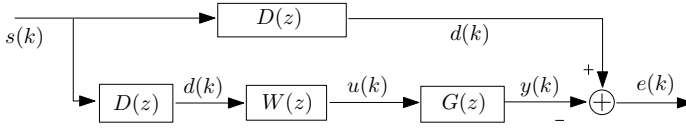
with $[\cdot]_+$ the causality operator and $(\cdot)^\dagger$ the left or right pseudo inverse. $G(z) = G_i(z)G_o(z)$ is an inner-outer factorization of $G(z)$, where $G_i(z)$ and $G_o(z)$ are asymptotically stable, $G_i^*(z)G_i(z) = I$ and $G_o(z)$ has a stable right inverse. $D(z) = D_{co}(z)D_{ci}(z)$ is an outer-inner factorization of $D(z)$, where $D_{co}(z)$ and $D_{ci}(z)$ are asymptotically stable, $D_{ci}(z)D_{ci}^*(z) = I$ and $D_{co}(z)$ has a stable left inverse.

Once the state-space realizations of $G(z)$ and $D(z)$ are given, the inner-outer factorization of $G(z)$ and the outer-inner factorization of $D(z)$ can be determined by solving two Riccati equations. If the disturbance $d(k)$ is an integrated white noise process, i.e. $D(z) = \frac{1}{1-z^{-1}}I$, and the transfer from $u(k)$ to $y(k)$ is static except for a pure 1-sample delay (i.e., $G(z) = z^{-1}L$ where $L \in R^{m_y \times m_u}$ is the static gain with full column rank), then the analytical expression of the optimal controller can be derived from Eq. (2.33) and Eq. (2.35) as

$$W(z) = L^\dagger, \quad (2.36)$$



(a) Block diagram of the closed-loop AO system where the optimal controller is structured by IMC approach



(b) Block diagram of the feedforward system which leads to identical $W(z)$ as in (a)

Figure 2.7: The problem of finding optimal feedback control block $W(z)$ to minimize the cost function J in (a) is equivalent to finding the optimal feedforward controller $W(z)$ minimizing cost function J in (b). It is assumed that $\hat{G}(z) = G(z)$ and $\hat{d}(k) = d(k)$ in (b).

$$C(z) = \frac{1}{1 - z^{-1}} L^\dagger, \quad (2.37)$$

with

$$D_{ci}(z) = I, D_{co}(z) = \frac{1}{1 - z^{-1}}, \quad (2.38)$$

$$G_i(z) = z^{-1}U_1, G_o(z) = \Sigma_1 V^T, \quad (2.39)$$

$$L = U_1 \Sigma_1 V^T. \quad (2.40)$$

Eq. (2.40) is the singular value decomposition (SVD) of L in economy size, with Σ_1 a diagonal matrix containing m_u non-zero singular values. L^\dagger is the pseudo-inverse of L such that $L^\dagger L = I$. It is worth noting that the optimal controller in Eq. (2.37) is just the conventional integrator-type controller with static gain L^\dagger and pure integrator $\frac{1}{1-z^{-1}}$. This gives a nice physical interpretation of the controller. The static gain L^\dagger is calculated by the CWF as in (2.36), which indicates that a static matrix projection is the optimal control action to minimize the residual error $e(k)$ in the feedforward scheme in Figure 2.7 (b), in case $d(k)$ is an integrated white noise process and DM is static. The integrator accounts for that only residual error $e(k)$ is available in closed-loop AO system instead of the disturbance itself.

To increase the robustness of the closed-loop AO system and prevent actuator saturation, two weighting parameters (denoted as $\rho_{in} \in \mathbb{R}$ and $\rho_{out} \in \mathbb{R}$) can be introduced in the controller design [88]. With ρ_{in} and ρ_{out} , the block $W(z)$ can be calculated as

$$W(z) = \tilde{G}_o^\dagger(z) \left[\tilde{G}_i^*(z) \bar{D}(z) \tilde{D}_{ci}^*(z) \right]_+ \tilde{D}_{co}^\dagger(z), \quad (2.41)$$

where $\tilde{G}(z)$, $\tilde{D}(z)$ and $\bar{D}(z)$ are constructed as

$$\tilde{G}(z) = \begin{bmatrix} G(z) \\ \rho_{out} I_{m_u} \end{bmatrix}, \tilde{D}(z) = \begin{bmatrix} D(z) & \rho_{in} I_{m_y} \end{bmatrix}, \bar{D}(z) = \begin{bmatrix} \tilde{D}(z) \\ 0_{m_u \times (m_y + m_s)} \end{bmatrix}. \quad (2.42)$$

$\tilde{G}(z) = \tilde{G}_i(z) \tilde{G}_o(z)$ is the inner-outer factorization of $\tilde{G}(z)$ and $\tilde{D}(z) = \tilde{D}_{co}(z) \tilde{D}_{ci}(z)$ is the outer-inner factorization of $\tilde{D}(z)$. I_{m_u} and I_{m_y} are the identity matrices with dimension m_u and m_y , respectively. ρ_{in} takes into account the measurement noise in $y(k)$. ρ_{out} balances the control effort $u(k)$ and the residual error $e(k)$. By increasing ρ_{in} and ρ_{out} , the measurement noise is accounted for more cautiously and control effort is reduced by the controller.

2.6 Experimental setup

2.6.1 Setup description

To validate the proposed strategy for model-based controller design, an experimental WFS-based AO setup has been built in the Smart Optics laboratory in Delft Center for Systems and Control (DCSC). Figure 2.8 illustrates the schematic of the setup and Figure 2.9 shows the photo.

Light from a HeNe laser ($\lambda=632$ nm) is focused by a microscope objective ($20\times$) into a pin hole with a diameter of $20 \mu\text{m}$. The spatial filter (i.e., the microscope objective and the pin hole) is used to suppress the high-order Gaussian modes in the laser [89] and simulate a distant star as a point source. The light passing through the spatial filter is collimated by lens L1. Because the laser is polarized, its intensity can be adjusted by the polarizer.

The collimated laser beam is reflected by flat mirrors M1 and M2 successively and passes through above the heater (see Figure 2.9). The heater had meant to be a disturbance generator. However, because the disturbance generated by the heater results in wavefront aberration which is beyond the spatial resolution of the 11-actuator PDM as checked from the WFS measurement, the heater is not used during the experiments and neglected in the schematic. Instead, the disturbance is introduced numerically after the WFS measurement as shown in Figure 2.3.

The laser passes through lens L2 and L3, and then directed to the PDM via M3, Lens L4, L5 and the beam splitter (BS1). BS1 splits the beam into two branches: one is reflected to the flat mirror M4 (red dashed in Figure 2.9) and the other

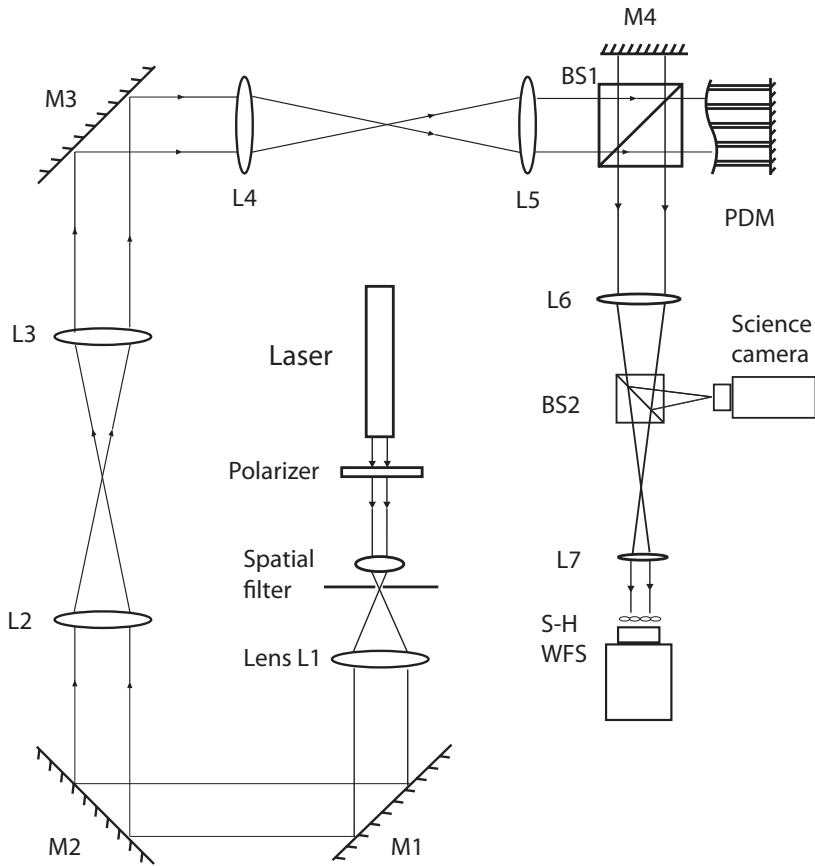


Figure 2.8: Schematic of the experimental AO setup in DCSC Smart Optics Lab.

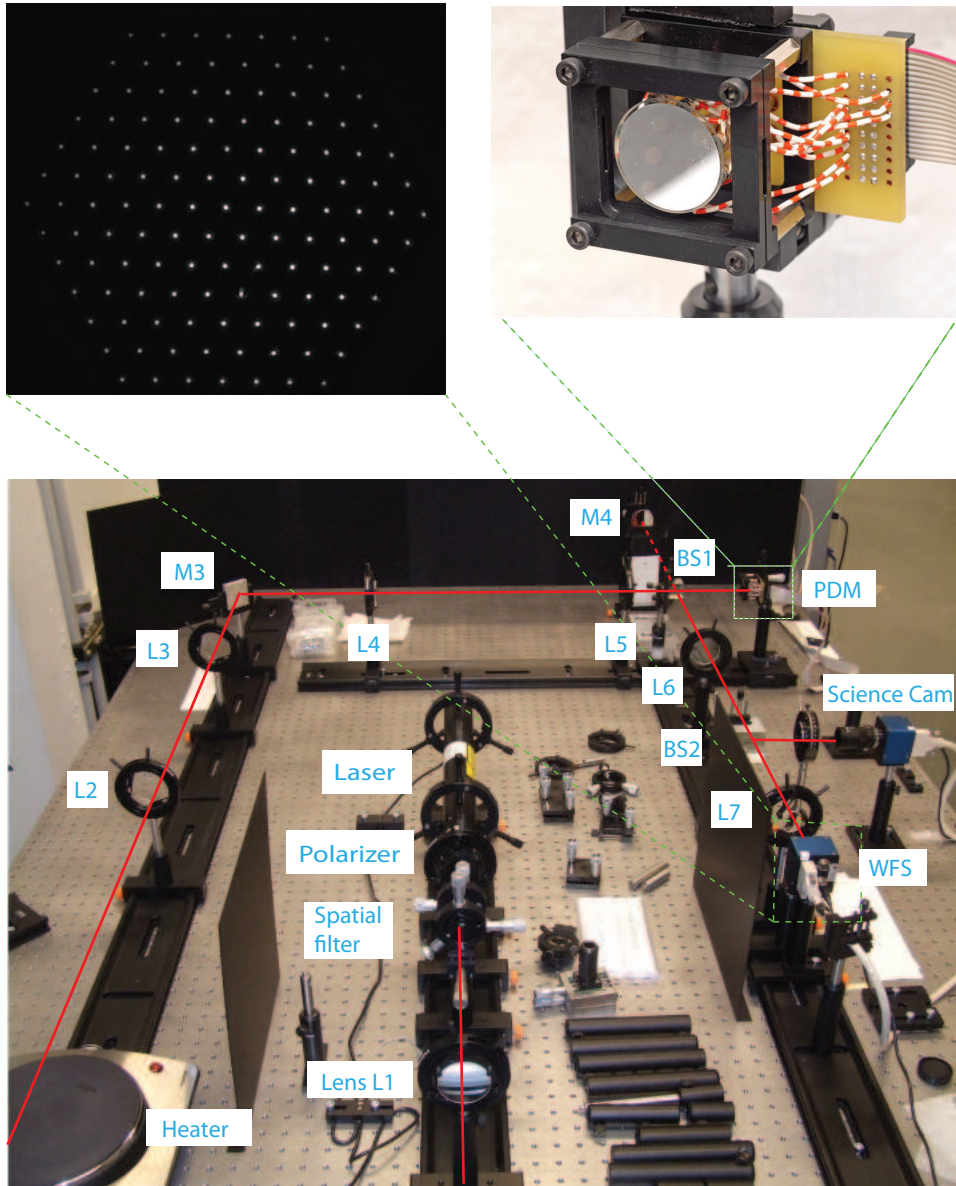


Figure 2.9: Photo of the experimental AO setup in DCSC Smart Optics Lab. The images of the S-H WFS (top left) and the PDM (top right) are zoomed in.

continues to the PDM. The flat mirror M4 is only used to calibrate the WFS so it is shielded during normal operation. The beam reflected back by the PDM is directed by BS1 to a telescope structure which consists of two lenses: L6 and L7. The PDM surface and the aperture of the WFS are conjugated by this telescope structure. The beam diameter is also scaled down by L6 and L7 such that the beam fits within the aperture of the WFS. A science camera has been installed in the setup to image the point source, i.e., the light emitted through the pin hole in the spatial filter.

The camera in the WFS captures the image formed by the lenslet array. Referring to Figure 2.10 (see Page 50), the image captured by the WFS camera is readout and transmitted to the control PC via a frame grabber (FG). The exposure of the camera is also set by the FG. The image processing algorithm removes the background light from the image and determines the center-of-mass of each spot. The spot locations are compared with their nominal values and the deviations are fed into the controller for control signal calculation. The control voltage to the PDM is set via a digital-to-analog (DA) card and amplified by a high voltage amplifier (HVA).

The image processing algorithm and the controller are implemented in a C-routine, which also calls the drivers of the FG and DA card for interfacing. Before the experiment, all the user-defined parameters for the hardware and software in the control loop are written in a .txt file by MATLAB and then read by the C-routine, e.g., the exposure and waiting time of the camera, the neural network in the hysteresis compensator, the system matrix in the state-space implementation of the controller, etc. During the experiment, only the C-routine communicates with the FG and DA card, while MATLAB has no influence on the AO system. After the experiment is finished, the results are written in another .txt file by the C-routine and then read by MATLAB for performance evaluation. e.g., the control signals, the spot locations or the residual output error.

In the setup, the DM prototype (OKOTech, Delft, The Netherlands) has a clear aperture of 25 mm and the mirror plate is supported by 11 piezoelectric tubes (PT130.00, Physik Instrumente, Germany). The piezo actuators are driven by the high voltage amplifiers (HVA, from OKOTech, Delft, The Netherlands) with an input range of 0~5 V, a DC voltage amplification of 80 and a -3dB bandwidth of 1 kHz. The S-H WFS (OKOTech, Delft, The Netherlands) consists of 127 hexagonally distributed lenslets with a focal distance of 15 mm and pitch of 300 μm . Figure 2.11 depicts the relative actuator-sensor layout in the CCD camera. Figure 2.12 shows the influence of each actuator in the DM. Each lenslet in the WFS provides a 2-dimensional measurement (i.e., horizontal and vertical movements of the spot) so that 254 sensor measurements are available in total. To make good use of the available sensor measurements but meanwhile reduce the computational complexity and improve the signal-to-noise ratio (SNR) of the system, 28 sensor measurements with high SNR are selected from the spots marked with * for control. This over-parameterized sensor-actuator configuration is in accordance with many operational AO systems where there are more sensor measurements than actuators [2, 3, 30]. The CCD camera (SVS340, SVS-VISTEK GmbH, Germany) has 640×480 square pixels of 7.4 μm and a maximum frame rate of 250 Hz. Via a frame

Table 2.1: List of main control components in the AO setup

Component	Model/Manufacturer	Description
PDM	OKOTech	11 piezo-actuators, prototype
HVA	OKOTech	0~400 V, 40 channels
WFS	OKOTech	127 hexagonal lenslets
Camera	SVS340, SVS-Vistek	640×460, maximum rate: 250fps
PC	Dell precision T7400	OS: openSUSE 10.3, kernel 2.6.22
DA	PD2-AO-96/16, UEI	±10 V, 96 channels, 16-bit
FG	Leonardo CL Full, ARVOO	Cameralink interface

grabber (Leonardo CL Full, ARVOO, The Netherlands), the image captured by the camera is transferred to the control computer (Dell Precision T7400, operated in openSUSE 10.3 with kernel 2.6.22). The DA card (PD2-AO-96/16, UEI, United States) has an output range of ± 10 V with 16-bit resolution. The main components in the setup has been summarized in Table 2.1.

2.6.2 Measurement noise

The measurement noise in the AO setup is characterized from the WFS measurements while the disturbance is absent and the control signal is zero (i.e., $d(k) = 0$, $u(k) = 0$). 1000 WFS measurements have been collected at a sampling rate of 230 Hz. The standard deviation of the measurement noise is about 0.023 pixel. In the identification of the inverse hysteresis model, since the amplitude of the excitation signal is very large (about 30 pixels in the peak-to-peak value as shown in Figure 2.14), the measurement noise is neglected. In the identification of the linear AO system, the effect of the measurement noise is incorporated by the PBSID_{opt} closed-loop identification algorithm. In the model-based controller design, the influence of the measurement noise is accounted for by the parameter ρ_{in} as explained in Section 2.7.3. The value of ρ_{in} is tuned such that the cost function J is minimized.

2.6.3 Timing of the setup

The timing of the closed-loop AO system is shown in Figure 2.13. The delay from the exposure trigger to the control voltage generation (denoted as τ) mainly consists of

- t_e : exposure time of the camera;
- $t_{m,1}$: image transmission time (from the camera to the frame grabber);
- $t_{m,2}$: image transmission time (from the frame grabber to CPU, also including image processing);
- t_c : controller computational time, including control signal calculation in the linear controller and hysteresis compensation.

Here $t_{m,2}$ also includes the image processing time, i.e., the center-of-mass algorithm to calculate the local gradients of the wavefront.

Based on the measured values of t_e , $t_{m,1}$, $t_{m,2}$ and t_c (shown in Figure 2.13), the delay τ is about 7.5 ms. During hysteresis compensation, the sampling interval t_s is 50 ms, which is far more than τ and the settling time of the DM (about 3 ms); hence the transfer from $V(k)$ to $y(k)$ is static except for a pure 1-sample delay. During the AO model identification, the sampling interval t_s is 4.3 ms (230 Hz), the influence of $V(k)$ can only be sensed since Frame $k + 2$. The time interval between $V(k)$ and the exposure trigger $k + 2$ is about $2t_s - \tau = 1.1$ ms, which is less than the settling time of the DM. Therefore dynamics can be observed from $V(k)$ to $y(k)$ apart from a pure 1-sample delay.

2.7 Experiments and results

The experiments are devoted to hysteresis compensation of the PDM, identification of the linear AO system and performance evaluation of the closed-loop AO system with model-based controller. The experimental setup is the same as depicted in Figure 2.1 with the number of inputs $m_u = 11$ and the number of outputs $m_y = 28$. The strategy in Section 2.3 is applied to obtain a linear dynamic model of the AO system. Controller design is based on Section 2.5.

2.7.1 Hysteresis compensation

To get the hysteresis data of the piezo actuator, actuator 1 is excited by a saw tooth signal, denoted as $V_1(k)$, of which the local maxima slowly decreases in time while the local minima are kept constant. The signal $V_1(k)$ is within the range 0~4 V (equivalent to 0~320 V over the piezo actuators) such that the hysteresis of the piezo actuator is excited. The period of the sawtooth signal is 5 s with the sampling rate of the WFS 20 Hz, to prevent exciting the dynamics of the AO system. The vertical displacement of spot s1 is recorded as $y_1(k)$ (the pure 1-sample delay has been removed so that $V_1(k)$ and $y_1(k)$ are already synchronized). Due to the creep in the piezo actuator, drift is observed in the displacement measurement as the local minima of the measurement decreases slowly in time, which all should theoretically lie at the same height. To reduce the drift, the measurement is lifted by a linear function obtained by fitting the local minima of the measurement. After this, the displacement measurement $y_1(k)$ is normalized such that it is within the same range as the voltage input $V_1(k)$.

A Preisach inverse hysteresis model is identified using $y_1(k)$ as input and $V_1(k)$ as output. The Preisach function $P(\alpha, \beta)$ is approximated by a two-layer feedforward neural network with eight neurons in the first layer and one neuron in the second layer. The neural network is trained by means of Levenberg-Marquardt (LM) backpropagation, using the MATLAB neural network toolbox [85]. Figure 2.14 (left) shows the relationship between the control signal $u_1(k)$ to actuator 1 and the measurement $y_1(k)$ when HC is off (solid, blue) and on (dashed, red). To quantify the hysteresis in the piezo actuator, a single parameter h_s is defined as the ratio of the maximum possible output difference for any input (Δy) divided by the output range (y_m), i.e., $h_s = \Delta y / y_m$. From the plot, it can be seen that h_s of actuator 1 has been reduced from 16.2% to 0.8% by HC and the linearity of the input-output curve has been improved significantly. This inverse hysteresis model is also used to compensate for hysteresis in all other actuators. The residual hysteresis in other actuators has been evaluated by exciting individual actuator one by one and measuring the displacement of the spot which gives best signal-to-noise ratio. The result is plotted in Figure 2.14 (right), where the hysteresis of single piezo actuators has been reduced from 16.4% to 1.4% in average by HC.

To further validate the hysteresis compensator in a more realistic situation where all the piezo actuators are excited simultaneously, a spectral analysis based

approach as described in [90] is used. In this approach, the PDM is excited by a multi-sine signal $u(k)$ where each channel of $u(k)$ consists of n_f harmonics at frequencies $f = (4i+1)f_0, i = 0, \dots, n_f-1$ with $f_0 \in \mathbb{R}$ the frequency resolution (see Figure 2.15). If the transfer from $u(k)$ to $y(k)$ is linear, then $y(k)$ should only consists of harmonics at $f = (4i+1)f_0$; otherwise the power at $f \neq (4i+1)f_0$ can be used as a measure of the nonlinearity in the AO system. During the experiments, all the actuators in the DM are excited by the control signal $u(k)$ simultaneously, with 2000 time samples. The frequency resolution is set $f_0 = 0.01$ Hz and the sampling rate of the WFS is 20 Hz.

Figure 2.16 shows the power spectrum averaged over all output channels in $y(k)$ with HC off (top) and on (bottom). The frequency components at $(4i+1)f_0$ are dominant in both plots, but the components at $(4i+3)f_0$ with HC off is about one order of magnitude above the noise level due to the nonlinearity in the AO system. By hysteresis compensation, these components at $(4i+3)f_0$ have been attenuated to the same order as the noise, indicating significant improvement in the linearity of the AO system and validating the hysteresis compensator.

2.7.2 Identification of the linearized AO system

After hysteresis compensation, a linear dynamic model of the AO system is identified with the closed-loop subspace identification approach. The identification consists of the following steps:

1. Excite the AO system in open-loop with control input denoted as $u_o(k)$ and record the measurement as $y_o(k)$. $u_o(k)$ are pseudo-random numbers between 1 V and 3 V, accounting for the fact that the control signal $u(k)$ is biased by 2 V in the closed-loop operation afterwards. The sampling rate of the WFS is 230 Hz. As explained at the beginning of Section 5, $u_o(k)$ and $y_o(k)$ consist of both the dynamics of the DM and a pure 1-sample delay. To get a static model of the AO system from $u_o(k)$ and $y_o(k)$, the measurement $y_o(k)$ is shifted by 2 time samples such that $\tilde{y}_o(k) = y_o(k+2)$, where $\tilde{y}_o(k)$ is the shifted output. A linear static model of the AO system, denoted as \hat{L} , is identified based on the data set $\{u_o(k), \tilde{y}_o(k)\}_{k=1}^N$ ($N=2000$ is the length of the data set) by linear least squares fitting, i.e.,

$$\hat{L} = \arg \min_{\hat{L}} \sum_{k=1}^N \|\tilde{y}_o(k) - \hat{L}u_o(k)\|_2^2. \quad (2.43)$$

The accuracy of the static model \hat{L} is evaluated by calculating the variance accounted for (VAF) of the model, which is defined as

$$\text{VAF}(\hat{y}, \tilde{y}) = \left(1 - \frac{\text{var}(\hat{y} - \tilde{y})}{\text{var}(\tilde{y})}\right) \times 100\%. \quad (2.44)$$

Here \hat{y} is the estimation of \tilde{y} and $\text{var}(\tilde{y})$ is the variance of \tilde{y} . Static models have also been identified by shifting $y(k)$ by 1 or 3 time samples, but only

shifting $y(k)$ by 2 time samples gives the highest VAF.

2. A conventional controller

$$C(z) = \frac{\mu}{1 - z^{-1}} (\hat{L}^T \hat{L} + \rho I)^{-1} \hat{L}^T, \quad (2.45)$$

is implemented with $\mu \in \mathbb{R}$ and $\rho \in \mathbb{R}$ user-defined parameters. The closed-loop AO system with this conventional controller is then operational to reject the disturbance $d(k)$ as in Figure 2.3. $d(k)$ is generated by $d(k) = D(z)s(k)$ with $D(z) = \hat{L}$ to simulate disturbance with broad temporal frequency range. The use of \hat{L} tries to limit $d(k)$ within the spatial range of the DM and reduce the influence of the DM-fitting error on the residual error of the closed-loop AO system. A bias of 2 V is added to the control signal $u(k)$ to allow for bi-directional deformation of the DM.

The closed-loop experiments are carried out for two times. Each time $D(z)$ is unchanged, but a new set of $s(k)$ is used to generate $d(k)$. The control signal and the WFS measurement in these two closed-loop experiments are recorded as $\{u_{c1}(k), y_{c1}(k)\}_{k=1}^{N_c}$ and $\{u_{c2}(k), y_{c2}(k)\}_{k=1}^{N_c}$, respectively. The data length in these two experiments are $N_c=2000$ and the sampling rate of the WFS is 230 Hz. $\mu = 0.2$ and $\rho = 2$ are taken in the controller to balance the stability and performance of the closed-loop AO system.

3. Considering that there is a pure 1-sample delay between $u_{c1}(k)$ and $y_{c1}(k)$, measurement $y_{c1}(k)$ is shifted by 1 time sample such that $\tilde{y}_{c1}(k) = y_{c1}(k+1)$, where $\tilde{y}_{c1}(k)$ is the shifted output. A set of dynamic models of the AO system are then identified in the state-space form with the order $m_x = 1, 2, \dots, 20$, based on the data set $\{u_{c1}(k), \tilde{y}_{c1}(k)\}_{k=1}^{N_c}$ with the closed-loop subspace identification algorithm in Section 3. The past horizon and future horizon used in the algorithm are both set 30. The VAF values of these dynamic models are evaluated as shown in Figure 4.6. There is significant improvement in the VAF if the order m_x of the dynamic model is increased until $m_x = 10$. The VAF value at $m_x = 10$ is already as high as 99.1% with HC on. A higher order can be also selected, however, as shown by the plot, an order higher than 10 gives very little improvement on the model accuracy. Therefore $m_x = 10$ is taken to balance the model accuracy and the model complexity. Apart from the numerical evaluation, a physical interpretation on this order selection is that since the DM surface has a free edge, the piston movement of the surface when all the actuators are deformed by the same amount can not be observed by WFS. Therefore effectively the DM only has 10 degrees-of-freedom.

From the subspace identification algorithm, \hat{A} , \hat{B} and \hat{C} are obtained and the transfer from $u_{c1}(k)$ to $\tilde{y}_{c1}(k)$ is represented by $\tilde{G}(z) = \hat{C}(zI - \hat{A})^{-1}\hat{B}$. The AO model from $u(k)$ to $y(k)$ is then obtained as $\hat{G}(z) = \tilde{G}(z)z^{-1} = \hat{C}(zI - \hat{A})^{-1}\hat{B}z^{-1}$, where z^{-1} accounts for the shift in $\tilde{y}_{c1}(k)$. In the minimal state-space realization, $\hat{G}(z)$ has an order of 21. In our case, because the disturbance $d(k)$ is introduced numerically in the controller instead of in the optical path, the response of the AO system $y(k)$ can be directly used for

identification of the AO system. This corresponds to the calibration of the AO system in a telescope [72] where the atmospheric disturbance is absent and the AO system is subject to the excitation source.

4. The accuracy of the static model \hat{L} and the dynamic model $\hat{G}(z)$ are evaluated with the fresh data set $\{u_{c2}(k), y_{c2}(k)\}_{k=1}^{N_c}$ according to the VAF of the models. In favor of the static model, the measurement $y_{c2}(k)$ is shifted by 2 time samples such that $\tilde{y}_{c2}(k) = y_{c2}(k+2)$ is used to validate \hat{L} . But in validating the dynamic model $\hat{G}(z)$, $y_{c2}(k)$ is used directly.

Table 1 gives the VAF of the static model \hat{L} and the dynamic model $\hat{G}(z)$ for the identification set and validation set, with HC off and on. The results are summarized as follows.

- Horizontally, in either identification set or validation set, no matter HC off or on, the dynamic models result in higher VAF values than the static models. In the worst case, VAF of the dynamic model can still reach as high as 96.5% while only 82.1% can be reached with static model in best case. This indicates that the dynamic models give more accurate estimation of the AO system than the static models.
- Vertically, the VAF values with HC on are higher than those with HC off in all the four cases. The difference is among 0.4% and 7.8%. It's noted that for the dynamic model, the difference in VAF between HC on and off (e.g., 99.1%-98.7%=0.4% for identification set) is less than that with static model (e.g., 82.1%-78.2%=3.9% for identification set). This is mainly due to that the hysteresis is modeled as dynamics in the AO system (referring to Figure 2.16, the spectrum of $y(k)$ is re-shaped by hysteresis). However, with the validation set, the difference between HC on and off has been enlarged for both static and dynamic model. This indicates that the uncertainty in the AO system has indeed been reduced by HC.
- Comparing the VAF values in the top left corner (78.2%) and the one in the bottom right corner (98.4%), it can be concluded that the dynamic model with HC has significantly improved the accuracy of the estimation.

Table 1. VAF of the models of the AO system. Static model \hat{L} and the dynamic model $\hat{G}(z)$ are identified from $\{u_o(k), \tilde{y}_o(k)\}_{k=1}^{2000}$ and $\{u_{c1}(k), y_{c1}(k)\}_{k=1}^{2000}$, respectively. \hat{L} is validated with $\{u_{c2}(k), \tilde{y}_{c2}(k)\}_{k=1}^{2000}$. $\hat{G}(z)$ is validated with $\{u_{c2}(k), y_{c2}(k)\}_{k=1}^{2000}$.

	Identification set		Validation set	
	Static model	Dynamic model	Static model	Dynamic model
HC off	78.2%	98.7%	72.0%	96.5%
HC on	82.1%	99.1%	79.8%	98.4%

2.7.3 Performance of the closed-loop AO system

After the model of the AO system is identified, a controller is designed based on the identified model of the AO system and the disturbance model. The disturbance is assumed to be integrated white noise process with $D(z) = \hat{L} \frac{1}{1-z^{-1}}$ in favor of the conventional controller, because it has been shown in Eq. (2.37) that the conventional controller is the optimal controller if the DM is static and the disturbance is an integrated white noise process. The controller is implemented in the state-space form with an order of 21. It's worth noting that in different applications, the disturbance may have different spatial or temporal characteristics other than an integrated white noise process. In that case, the filter $D(z)$ can be adapted according to the prior knowledge of the statistics of the disturbance, e.g., [17], or be identified from the measurement data using a data-driven identification approach [30]. Based on the disturbance model and the AO model, the controller $C(z)$ can be updated using Eq. (2.33) and (2.35).

Experiments are carried out to evaluate the performance of the closed-loop AO system, with the disturbance $d(k)$ integrated white noise as described above. The sampling rate of the closed-loop AO system is 230 Hz. The data length is $n_d = 1000$. The performance of the closed-loop AO system is evaluated in terms of the sum of the variance of the residual error (denoted as J_e), which is defined as

$$J_e = \frac{1}{n_d - 1} \sum_{k=1}^{n_d} (e(k) - \bar{e})^T (e(k) - \bar{e}), \quad (2.46)$$

where \bar{e} is the mean of $e(k)$ over n_d time samples. Comparison is made between four cases: conventional controller with HC off (A1) and HC on (A2), dynamic-model-based controller with HC off (B1) and HC on (B2). The parameters in all the controllers are tuned such that the best performance of each is achieved. Figure 2.18 shows J_e achieved for different μ and ρ in the conventional controller and for different ρ_{in} and ρ_{out} in the proposed dynamic-model-based controller. It can be seen that the dynamic-model-based controllers (B1 and B2) result in less residual error than the conventional controller (A1 and A2). Minimal J_e is reduced from 13.8 (A1) to 10.4 (B1) and from 12.7 (A2) to 9.6 (B2). Hysteresis compensation improves the performance and performance robustness of the closed-loop AO system, either with the conventional controller or dynamic-model-based controller. Broader range of μ and ρ_{out} , e.g. $\mu = 0.5$ and $\rho_{out} = 0.4$, can be used in the controllers without severely deteriorating the performance. By combining hysteresis compensation and dynamic-model-based controller design, J_e has been reduced from 13.8 (A1) to 9.6 (B2), by about 30%.

Figure 2.19 shows the transient response of the closed-loop AO system subject to static disturbances. The response is averaged over 20 experiments. In each experiment, a random static disturbance is applied since $k = 0$. Apart from the measurement noise, the error is unchanged at $k = 1$ due to the delay in the closed-loop AO system (see Figure 2.13, control signal $u(0)$ can only influence the measurement since $y(2)$). The dynamic-model-based controllers (B1 and B2) lead to

faster convergence than conventional controllers (A1 and A2) in general. A1 and A2 require 4 time samples to reach about 10% of the initial error while B1 and B2 only take 3 time samples. The effect of hysteresis compensation can be visualized as well in this figure where a reduction of 0.13 is observed in the normalized error variance at time sample 2 (from 0.34 in B1 to 0.21 in B2) and the oscillation at the 7th time sample in A1 is reduced significantly in A2.

2.7.4 Computational time

The controller computational time t_c (see Figure 2.13) is important for real-time implementation of the closed-loop AO system. The computational load comes from the hysteresis compensator and the dynamic-model-based controller. Since the inverse hysteresis models in the hysteresis compensator have the same structure, the computational complexity of the hysteresis compensator is proportional to the number of actuators in the PDM. In our experiments, the computational time required by the hysteresis compensator is about $20 \mu\text{s}$ per sample (approximately $1.9 \mu\text{s}$ per sample per actuator). The model-based controller is implemented in the state-space form with input dimension $m_y = 28$, output dimension $m_u = 11$ and an order of 21. The computational time for the dynamic-model-based controller is about $15 \mu\text{s}$ per sample, which results in a total computational time of $t_c = 20 + 15 = 35 \mu\text{s}$. With conventional static-model-based controller and HC off, the computation takes about $5 \mu\text{s}$. The additional $30 \mu\text{s}$ introduced by our dynamic-model-based controller with HC is negligible compared with the sampling interval of the closed-loop system ($t_s = 4.3 \text{ ms}$), but a significant performance improvement can be achieved by the proposed controller.

2.8 Conclusion

A model-based controller is designed for a closed-loop AO system with PDM and high-sampling-rate WFS. The proposed controller consists of a hysteresis compensator reducing the hysteresis in the PDM and a linear model-based controller taking care of the linear dynamics in the closed-loop system.

The hysteresis in the piezo actuators is reduced from 16.4% to 1.4% in average by the hysteresis compensator. After hysteresis compensation, a linear dynamic model of the AO system is identified by a closed-loop subspace identification approach. The identified dynamic AO model gives more accurate estimation of the AO system compared to the conventional static AO model, with an improvement in VAF from 72.0% to 98.4% for the validation data set. The variance of the residual error of the closed-loop AO system has been reduced by 30% in case the disturbance is an integrated white noise. Transient response shows that the convergence speed and the robustness of the closed-loop AO system has been improved significantly.

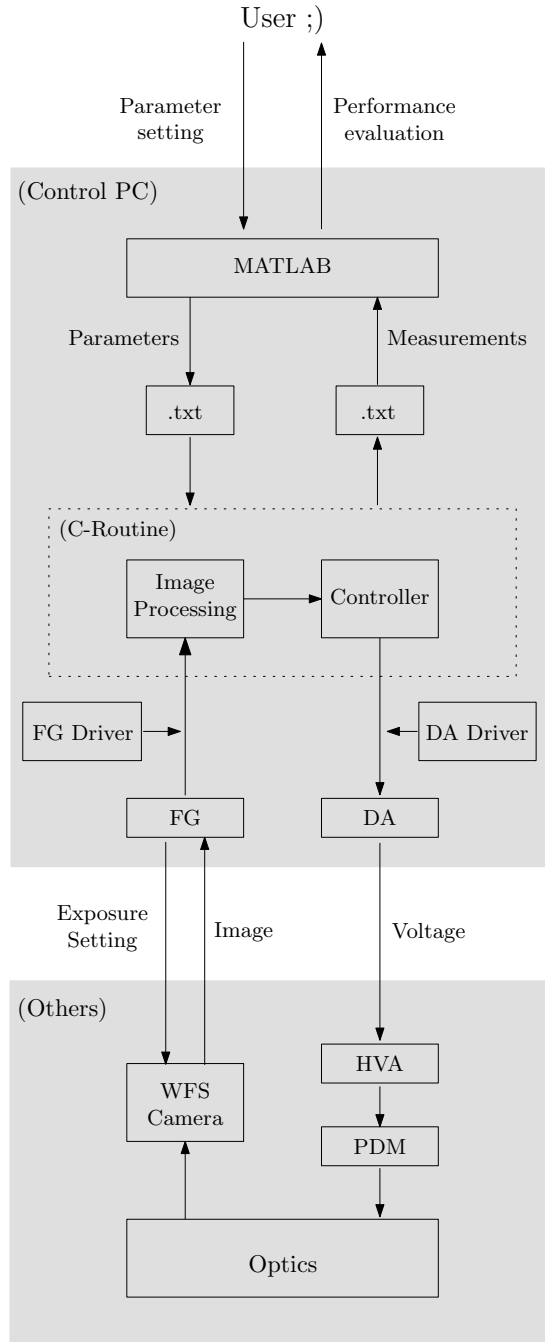


Figure 2.10: Structure of the control system in the WFS-based AO setup. The controller is implemented in a C-routine with the image processing algorithm. User sets the parameters for the control system before the experiment and evaluates the performance afterwards, both via MATLAB.

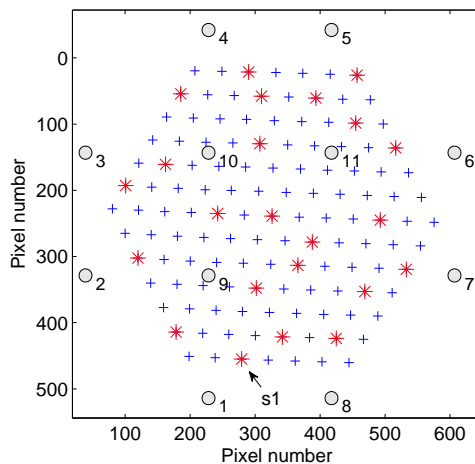


Figure 2.11: Layout of the actuator (o) and the S-H WFS (+) in the CCD camera. Because the deformation of the DM surface is spatially restricted by 11 actuators, 28 representative measurements from the spots marked with * are selected for control, in order to reduce the computation complexity and have a good SNR. Vertical displacement from spot s1 is used for hysteresis identification.

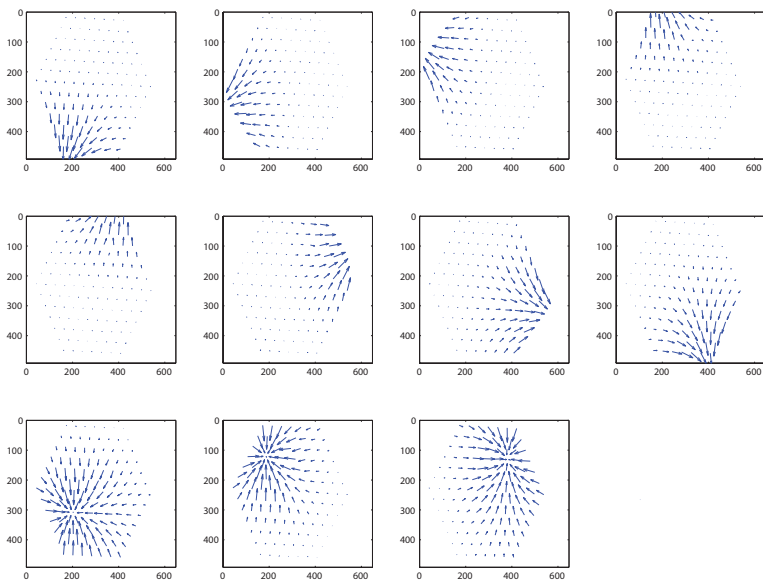


Figure 2.12: Influence of each actuator in the DM on the WFS measurement. Each actuator has a significant influence on its neighboring spots.

t_s : sampling interval of the camera;
 $t_e = 0.1$ ms: exposure time of the camera;
 $t_{m,1} = 4.0$ ms: transmission time from the camera to the frame grabber;
 $t_{m,2} = 3.4$ ms: transmission time from the frame grabber to CPU, including image processing;
 $t_c = 35$ μ s: controller computational time;
 F_k : Frame k taken by the camera.

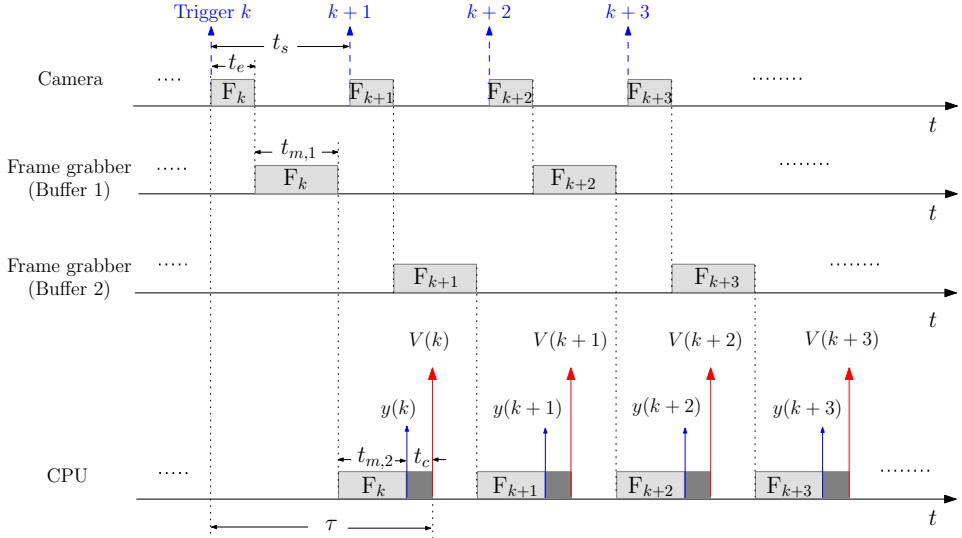


Figure 2.13: Timing of the closed-loop AO system. Each frame captured by the camera is transmitted to the CPU via the buffer (Buffer 1 or 2) of the frame grabber. Only after the image stored in the buffer has been processed by CPU (after time $t_{m,2}$), is this buffer available for a new image. The CPU computational time $t_{m,2} + t_c$ for each frame should be less than t_s , otherwise images will be accumulated in the buffers.

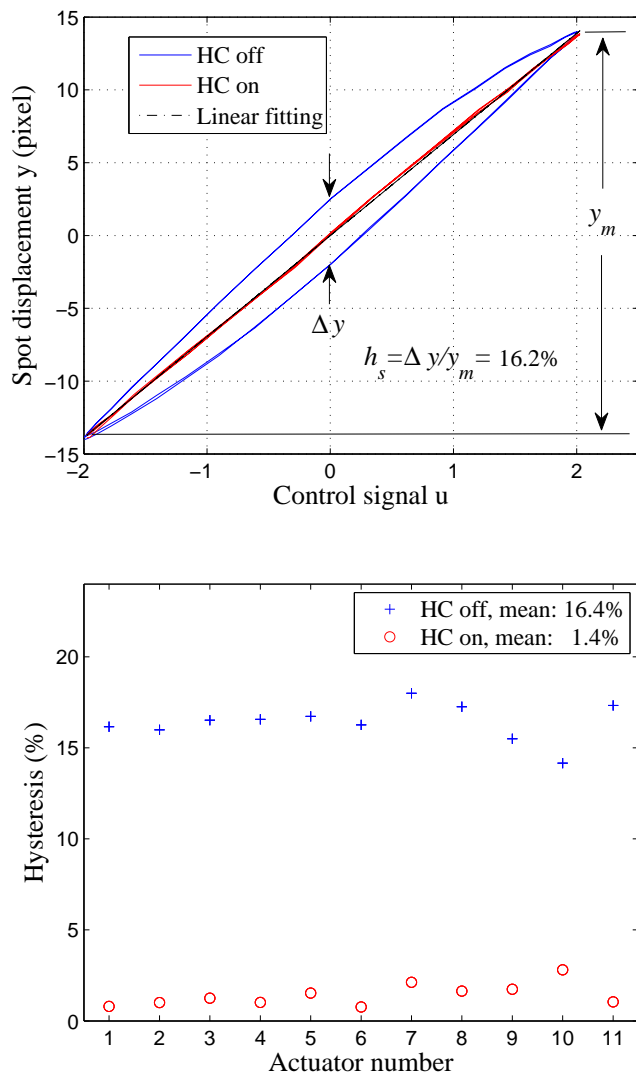


Figure 2.14: Top: hysteresis curve of a piezo-actuator (i.e., $y_1(k)$ with respect to $u_1(k)$) without (blue) and with (red) hysteresis compensation; bottom: hysteresis in each actuator with hysteresis compensation off (cross) and on (circle). The hysteresis of single piezo actuator has been reduced from 16.4% to 1.4% in average.

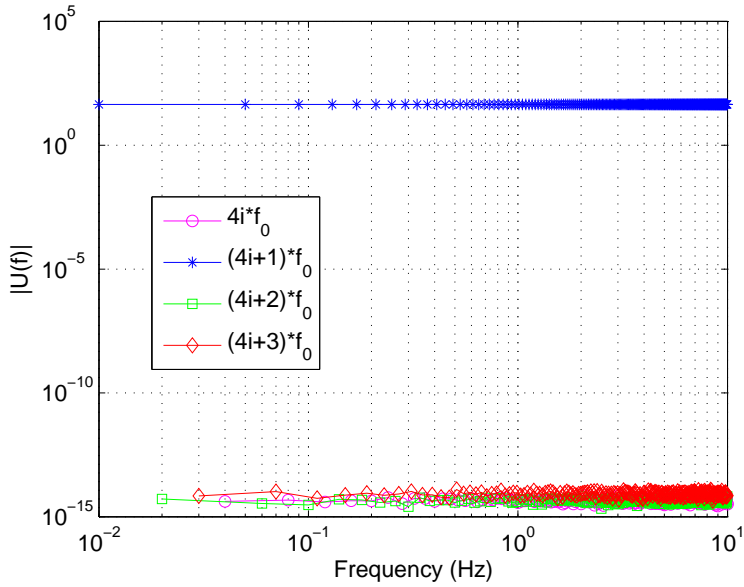


Figure 2.15: Power spectrum of the control signal $u(k)$. $U(f)$ is the Fourier transform of $u(k)$. Power of $u(k)$ is only located at frequencies $f = (4i+1)f_0, i = 0, \dots, n_f - 1$.

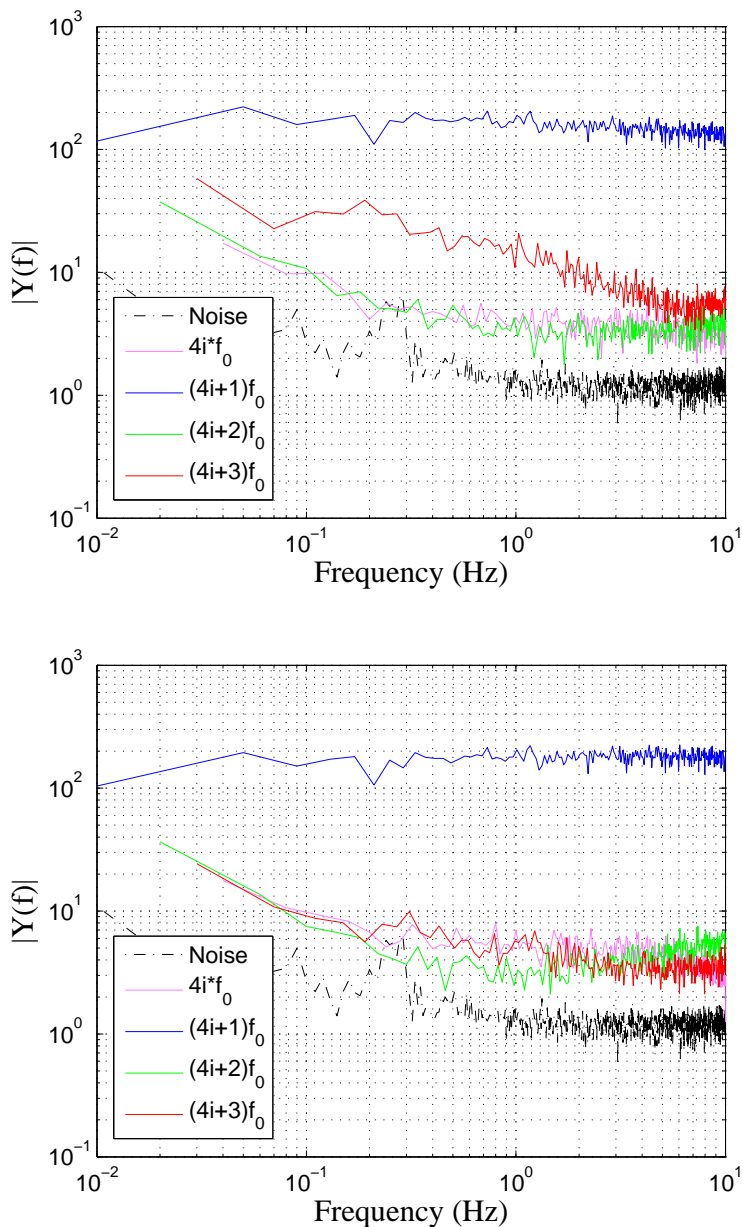


Figure 2.16: Spectrum of the measurement $y(k)$ with HC off (top) and on (bottom). $Y(f)$ is the Fourier transform of $y(k)$. By HC, the power components at $f = (4i+3)f_0$ have been significantly reduced, indicating improved linearity of the PDM.

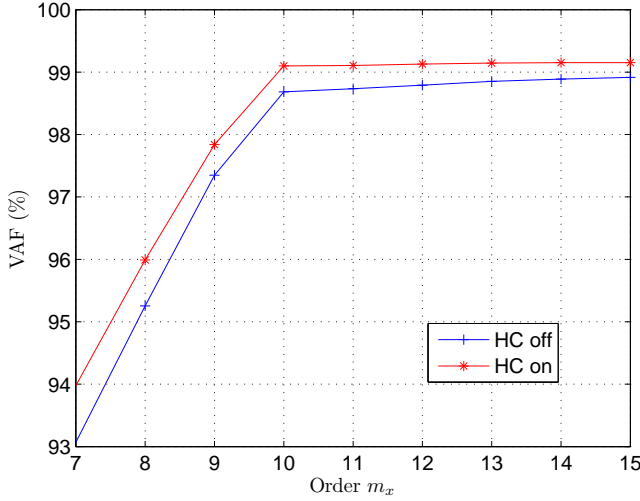


Figure 2.17: VAF of the state-space model of the AO system with respect to the order m_x , zoomed in for $m_x = 7, \dots, 15$. The order $m_x = 10$ is selected to balance the model accuracy and the model complexity.

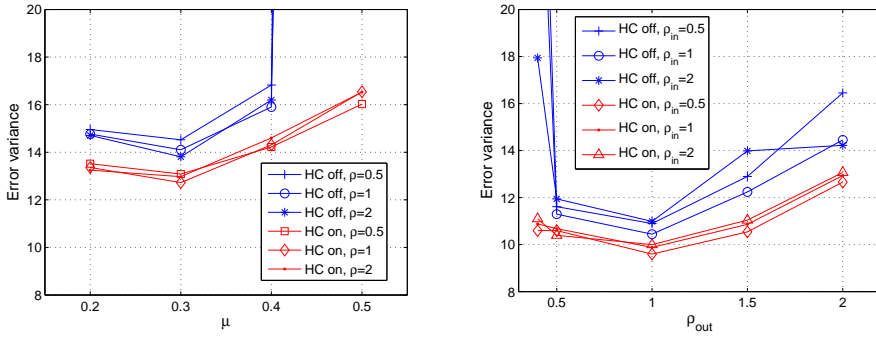


Figure 2.18: Error variance J_e achieved for different μ and ρ in the conventional controller and for different ρ_{in} and ρ_{out} in the proposed dynamic-model-based controller. By combining hysteresis compensation and dynamic-model-based controller design, J_e has been reduced from 13.8 (A1) to 9.6 (B2), by about 30%.

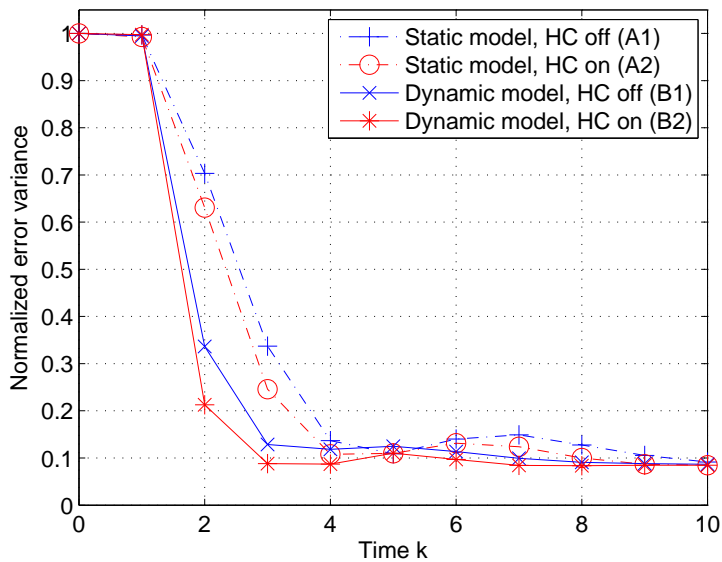


Figure 2.19: Transient response of the closed-loop AO system subject to random static disturbance at a sampling rate of 230 Hz (sampling interval $t_s=4.3$ ms). By dynamic-model-based controller with HC on (B2), the convergence speed of the closed-loop AO system is improved.

Hysteresis compensation for a PDM in a WFSless AO system

In many scientific and medical applications, wavefront-sensor-less (WFS-less) adaptive optics (AO) systems are used to correct the wavefront aberration by optimizing a certain target parameter, which is nonlinear with respect to the control signal to the deformable mirror (DM). Hysteresis is the most common nonlinearity of piezo-driven DMs (PDMs), which imposes a limit in the accuracy of the PDM when the stroke of the piezo-actuator is on the order of micrometers. This chapter discusses how to compensate for the hysteresis in the PDM by an inverse Preisach hysteresis model, where the hysteresis curve is extracted from the input-output data of the WFSless AO system for inverse hysteresis model identification. Experimental results show that the hysteresis in the PDM is reduced significantly by the inverse hysteresis model. The approach discussed in this chapter is used for hysteresis compensation in Chapter 4.

3.1 Introduction

Piezo-driven deformable mirrors (PDMs) are widely used in adaptive optics (AO) systems to reduce the wavefront aberration because of its capability of providing large stroke ($\sim \mu m$) and high stiffness [2, 58]. However, the intrinsic hysteresis of the piezo-actuators [82] impose a limit in the accuracy of the PDM when the applied actuation is on the order of micrometers. The error due to hysteresis can be as much as 10% – 20% when the actuator is driven at large stroke in open-loop by a voltage source. In closed-loop AO systems, if hysteresis is not compensated for, it may affect the convergence speed of the feedback optimization, which either results in larger residual error or limits the bandwidth of the system [60].

To compensate for the hysteresis in PDMs, different approaches have been proposed as summarized below.

- **State initialization**
Kudryashov and Shmalhausen [59] compensated for the hysteresis of a bimorph mirror, by applying harmonic signal with decreasing amplitude to the piezo actuator each time before the desired voltage is assigned. Essentially this method wipes out the input history and initializes the piezo actuator to certain state each time before any new action. This method does not require any hardware modification, but a longer settling time is required due to the initialization process, thus limiting the bandwidth of the system.
- **Feedback control**
Chang [78] used strain gauges, temperature sensors and feedback controller to linearize each piezo actuator in a segmented PDM. In his work, the displacement of each piezo actuator is measured by each strain gauge and compared with the desired trajectory. The control signal is generated by the controller such that the displacement of the actuator tracks the desired trajectory. To obtain accurate displacement measurement, the temperature in each strain gauge is measured by the temperature sensor and the thermal effect in the strain gauge is compensated by the controller. This scheme reduces the hysteresis very effectively, but the hardware complexity has been increased significantly, e.g., the use of strain gauges, temperature sensors and the controller incorporating both displacement and temperature measurements.
- **Feedforward control**
Yang [60] corrected the hysteresis of a bimorph mirror by feedforward linearization with an enhancing Coleman-Hodgdon inverse hysteresis model. Dubra [61] also reduced the hysteresis of a single-actuator bimorph mirror with a classical and a generalized Preisach inverse hysteresis model. In this approach, a mathematical model of hysteresis should be identified beforehand from the experimental data, and then used to generate control signal to the DM based on the desired trajectory. The advantage of this approach is that it can be implemented without hardware modification and can be easily extended for large-scale AO systems. Furthermore, since the controller is built from the experimental data, it is able to give accurate estimation of both the memory effect and gain variation due to hysteresis, thus improving the performance in compensation.
- **Charge control**
In this approach, the charge rather than the voltage is used to control the displacement of the piezo actuator, which results in less hysteresis (e.g., by a factor of approximately five [84]) than with a voltage source. However, apart from the fact that a specially designed charge drive amplifier is required in this approach, it can lead to additional drift and saturation problems and has a negative effect on the scan range [75].

Feedforward control has the advantages of being efficient in hysteresis reduction, simple in implementation and extendable for large-scale AO systems, which makes it a promising candidate for hysteresis compensation for the PDM.

In WFS-based AO systems, the hysteresis of the PDM can be directly characterized by the S-H WFS, where the sensor output is linearly related to the actuator displacement. But in WFS-less AO systems, the only measurement is the target parameter, like the light intensity within certain aperture, which involves some memory-less nonlinearity originating from the optical system as well as the hysteresis of the PDM. This makes the hysteresis identification and compensation even more challenging. Therefore this chapter investigates how to reconstruct the hysteresis of the PDM only based on the nonlinear measurement of the WFS-less AO system, and then compensate for the hysteresis in the DM using an inverse Preisach hysteresis model [75] which is identified from the reconstructed hysteresis curve. The technique described in this chapter is used to reduce the uncertainty in the WFSless AO system in Chapter 4 and leads to an accurate model for the model-based control.

In Section 3.2, the experimental setup is described. Principles on hysteresis reconstruction and hysteresis compensation is discussed in Section 3.3, followed by the results in Section 3.4. Concluding remarks are given in Section 3.5.

3.2 Experimental setup

The schematic of the experimental setup is depicted in Figure 3.1 (left). The collimated laser beam (He-Ne laser, with a wavelength of 632 nm) passes through the beam splitter first, then reflected by the PDM and directed to the lens. Similar to the Foucault test [91], a razor blade blocks part of the beam at the back focal plane of the lens, followed by a photodiode(TSL250R-LF, TAOS, Korea) measuring the light intensity of the residual beam. The PDM prototype (OKOTech, Delft, The Netherlands) has a clear aperture of 25 mm and the mirror plate is supported symmetrically by 12 piezoelectric tubes (PT130.00, Physik Instrumente, Karlsruhe, Germany, refer to Figure 3.1 (right) for the actuator distribution). The high voltage amplifier (HVA) has an input range of 0~5 V and a voltage amplification of 60 for frequency lower than 1 kHz. Signal generation and data acquisition is accomplished by a dSPACE system (DS1103PPC, dSPACE, Germany) with the D/A card output range of ± 10 V, 14-bit and A/D card input range of ± 10 V, 16-bit.

As discussed in Section 2.3, the PDM is considered as a Hammerstein-type nonlinear system with hysteresis at its input followed by the linear dynamics at its output. The hysteresis in each piezo-actuator is decoupled. During each experiment, only one actuator in the DM is driven by the voltage V_i via the HVA, while the electrodes of all other actuators are open. Since the frequency of V_i (less than 10 Hz) is much lower than the first resonant frequency of the DM (about 1 kHz), all the dynamics is neglected. The voltage V_i is defined as the input of this opto-mechatronic system and the output is the light intensity measurement V_o .

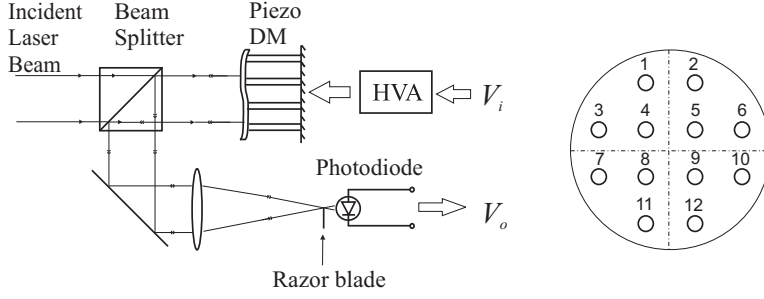


Figure 3.1: Left: schematic of the experimental setup (input: voltage V_i ; output: light intensity measurement V_o); right: actuator layout in the PDM.

By physical modeling [13], the intensity measurement V_o can be represented as:

$$V_o = A_l \iint_{\Sigma_b} \left| \iint_{\Sigma_l} \exp[-j \frac{2\pi}{\lambda} (\phi_i(\xi, \eta) + 2\phi_m(\xi, \eta))] \cdot \exp[-j \frac{2\pi}{\lambda d_l} (m_1 \xi + m_2 \eta)] d\xi d\eta \right|^2 dm_1 dm_2 \quad (3.1)$$

where A_l is a constant determined by the power of the incident light, $j = \sqrt{-1}$, λ is the wavelength of light and d_l the focal distance of the lens. (ξ, η) and (m_1, m_2) represent the coordinates in the input plane and the focal plane of the lens, respectively. Σ_l represents the illuminated area in the lens by the incident light. Σ_b represents the area in the focal plane of the lens, which is not blocked by the razor blade. ϕ_i is the wavefront of the incident light. ϕ_m is the surface deflection of the DM, determined by following equations [92]:

$$\phi_m(z_x, z_y) = \sum_{q=1}^{n_q} \frac{P_q W(z_x, z_y, \zeta_{q,x}, \zeta_{q,y})}{16\pi D_m} + w_0 + w_1 z_x + w_2 z_y \quad (3.2)$$

$$P_q = \begin{cases} k_e (h_i - \phi_m(\zeta_q)) & \text{if actuator } q \text{ is excited by } V_i \\ -k_e \phi_m(\zeta_q) & \text{otherwise.} \end{cases} \quad (3.3)$$

$$h_i = H(V_i), \quad (3.4)$$

$$\sum_{q=1}^{n_q} P_q = 0, \quad \sum_{q=1}^{n_q} P_q \zeta_{q,x} = 0, \quad \sum_{q=1}^{n_q} P_q \zeta_{q,y} = 0. \quad (3.5)$$

Here (z_x, z_y) and (ζ_x, ζ_y) are the coordinates in the PDM surface. P_q , $q = 1, \dots, n_q$ are the forces applied to the PDM faceplate by actuator q at $(\zeta_{q,x}, \zeta_{q,y})$. D_m is the cylindrical rigidity of the faceplate, $W(z_x, z_y, \zeta_{q,x}, \zeta_{q,y})$ is a constant matrix determined by the DM structure, w_0 , w_1 and w_2 are the coefficients. k_e is the elastic constant of the piezo-actuator. $H(\cdot)$ represents the hysteresis in the piezo-actuator and $h_i = H(V_i)$ represents the displacement of the actuator when driven

by voltage V_i , with free end.

As formulated at the end of Section 3.1, the problem is how to reconstruct the hysteresis $H(\cdot)$ or the displacement h_i of the piezo-actuator only based on the (V_i, V_o) data, and identify an inverse hysteresis model based on the reconstructed hysteresis curve.

3.3 Principles

3.3.1 Hysteresis reconstruction

According to Mayergoyz's theory [82], hysteresis can be defined as the memory effect in the input-output relationship. This allows to separate hysteresis from the memory-less nonlinearity originating from the optical system (see Figure 3.2). Eq. (3.1)-(3.5) can be written as

$$V_o = f_l(x_h), \quad (3.6)$$

$$x_h = H(V_i), \quad (3.7)$$

where $H(\cdot)$ represents the memory effect due to hysteresis and $f_l(\cdot)$ represents all memory-less nonlinearity originating from the optical system. Variable x_h denotes the output of $H(\cdot)$. Since there is no other transformation in $H(\cdot)$ except for the memory, the hysteresis represented by $H(\cdot)$ is normalized in the sense that two hysteresis branches in a hysteresis loop join at (V_{ic}, x_c) with $x_c = V_{ic}$ (refer to Figure 3.3) and this loop can be generalized for different input ranges.

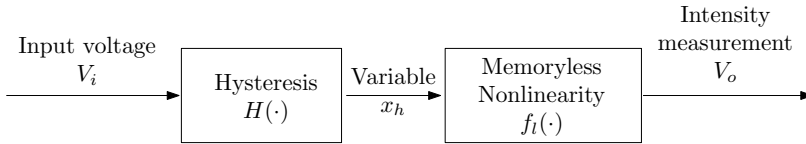


Figure 3.2: The hysteresis $H(\cdot)$ and the memoryless nonlinearity $f_l(\cdot)$ originating from the optical system are separated.

To identify $H(\cdot)$ from V_i and V_o , the signal x_h needs to be reconstructed from V_o as

$$x_h = f_l^{-1}(V_o). \quad (3.8)$$

Physical expression of $f_l^{-1}(\cdot)$ is difficult to achieve if only based on Eq. (3.1)-(3.5), because the parameters like ϕ_i , Σ_l and Σ_b are unavailable in most practical cases. However, a numerical approach can be taken as an alternative, which consists of three steps:

1. Suppose there were no hysteresis in the system, then $x_h = V_i$. The virtual

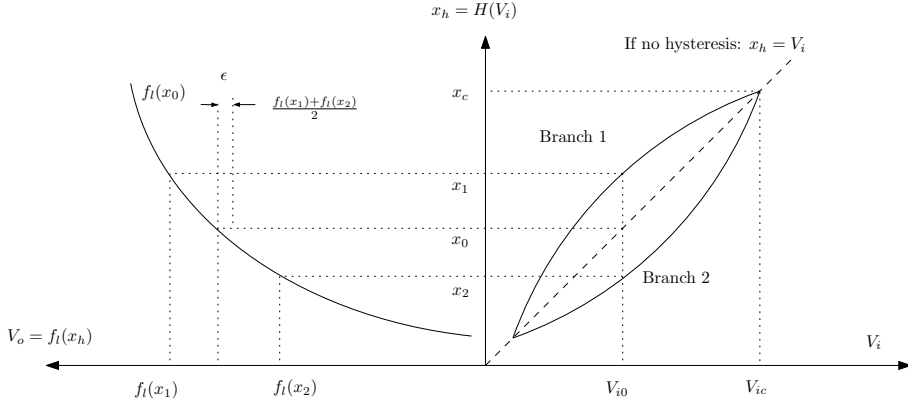


Figure 3.3: Transfer from V_i to V_o . Two hysteresis branches join at $x_h = V_i$. Virtual output $V_{ol} = f_l(x_0) = f_l(V_{i0})$ can be approximated by $\frac{f_l(x_1) + f_l(x_2)}{2}$ with error ϵ .

output V_{ol} would be

$$V_{ol} = f_l(V_i). \quad (3.9)$$

As hysteresis is present, V_{ol} can be approximated by taking the average of the two branches in the (V_i, V_o) loop. For certain input $V_i = V_{i0}$ (see Figure 3.3), this approximation denoted as \hat{V}_{ol} equals

$$\hat{V}_{ol} = \frac{1}{2}(f_l(x_1) + f_l(x_2)). \quad (3.10)$$

By a Taylor series expansion of $f_l(x_h)$ near $x_h = x_0$, we get

$$\hat{V}_{ol} = \frac{1}{2}(f_l(x_1) + f_l(x_2)) = f_l(x_0) + \epsilon, \quad (3.11)$$

where

$$\begin{aligned} \epsilon = & \frac{1}{2} \frac{df_l(x_h)}{dx_h} \Big|_{x_h=x_0} (x_1 + x_2 - 2x_0) \\ & + \frac{1}{2} \frac{d^2 f_l(x_h)}{2! dx_h^2} \Big|_{x_h=x_0} ((x_1 - x_0)^2 + (x_2 - x_0)^2) + \dots \end{aligned} \quad (3.12)$$

is the approximation error. If

$$x_1 - x_0 \approx x_0 - x_2 \quad (3.13)$$

and the higher-order terms are small enough, then

$$\hat{V}_{ol} \approx f_l(x_0) = f_l(V_{i0}). \quad (3.14)$$

More generally,

$$\hat{V}_{ol} \approx f_l(V_i). \quad (3.15)$$

2. The inverse of the nonlinearity $f_l(\cdot)$ (if it exists), can be identified by polynomial curve-fitting, defined as

$$\min_{a_m} \|V_i - \hat{V}_i\|_2^2, \quad (3.16)$$

with

$$\hat{V}_i = \hat{f}_l^{-1}(\hat{V}_{ol}) = \sum_{m=0}^M a_m \hat{V}_{ol}^m \quad (3.17)$$

where \hat{V}_i and $\hat{f}_l^{-1}(\cdot)$ are the estimates of V_i and $f_l^{-1}(\cdot)$, respectively. M and a_m are the order and the coefficients of the polynomial, respectively. If $f_l^{-1}(\cdot)$ does not exist because the mapping from \hat{V}_{ol} to V_i is not unique, then the (V_i, \hat{V}_{ol}) data set is divided into different subsets according to the first-order derivative of \hat{V}_{ol} with respect to V_i [93]. In each subset, the mapping from \hat{V}_{ol} to V_i is unique, thus can be approximated by function $\hat{f}_{l,p}^{-1}(\cdot)$, $p = 1, 2 \dots n_p$, where n_p is the number of subsets.

3. Appropriate function $\hat{f}_{l,p}^{-1}(\cdot)$ is selected for given V_o , according to the first order derivative of V_o . Then the estimation of x_h , denoted by \hat{x}_h , is obtained by

$$\hat{x}_h = \hat{f}_{l,p}^{-1}(V_o), \quad p = 1, 2 \dots, n_p. \quad (3.18)$$

To get accurate estimate \hat{x}_h , the function $f_l^{-1}(\cdot)$ should be approximated accurately with the polynomial. Two methods can be used to improve the accuracy of $\hat{f}_l^{-1}(\cdot)$:

- The nonlinearity $f_l(\cdot)$ and its inverse $f_l^{-1}(\cdot)$ depend on the integration area Σ_l and Σ_b (refer to Eq. (3.1)). The beam size or the razor may be tuned such that $f_l^{-1}(\cdot)$ is simple enough to be approximated accurately.
- Polynomials with higher order may be used to approximate $f_l^{-1}(\cdot)$.

3.3.2 Hysteresis compensation

Once the hysteresis curve of the piezo-actuator is reconstructed, the hysteresis in the piezo-actuator can be reduced by feedforward control as shown in Figure 2.2. The piezo-actuator is considered as the cascade of the rate-independent hysteresis and the LTI structure dynamics [75]. Since the frequency range of the input (less than 10 Hz) is much lower than the resonant frequency of the DM (about 1 kHz), the LTI dynamics is neglected. The inverse hysteresis model can be identified as described in Chapter 2.

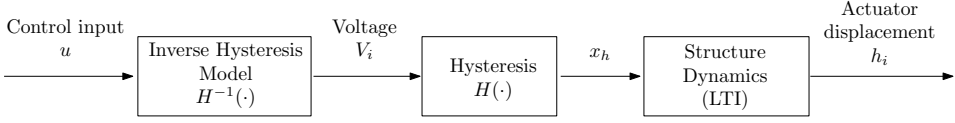


Figure 3.4: Block diagram of feedforward compensation of the piezo hysteresis. The hysteresis compensator consists of the inverse hysteresis model $\hat{H}^{-1}(\cdot)$.

3.4 Experimental results

Experiments have been done to verify the algorithm proposed in Section 3.3. The experimental setup is the same as in Section 3.2. The sampling rate in all the experiments are set as 10 Hz to prevent to excite the dynamics in the system.

Experiments consists of four steps: 1. single-loop hysteresis reconstruction; 2. multi-loop hysteresis reconstruction; 3. identification of the inverse Preisach hysteresis model; 4. hysteresis compensation.

3.4.1 Single-loop hysteresis reconstruction

The system is excited by voltage V_i and intensity measurement V_o is collected. During the experiments, the razor is finely tuned to observe the change in the nonlinearity. Concerning the symmetry in the actuator layout and the optical system, only Actuator 1 or 4 is excited individually. Figure 3.5 shows the typical (V_i, V_o) curves corresponding to Actuator 1 (left) and 4 (right) when the razor is at different positions. The change of nonlinearity as well as the hysteresis can be observed clearly.

To get accurate \hat{x}_h , only the curves with simple nonlinearity, marked as A_1 , A_2 , B_1 and B_2 , are selected for further processing and the hysteresis curves extracted from these four are plotted in Figure 3.6. To evaluate the accuracy of the estimation, hysteresis of a piezo actuator of the same type has been measured independently by a position sensor (S5990-01, HAMAMATSU, Japan) using an optical lever, as shown in Figure 3.6. Because the measured hysteresis curve involves linear transformations due to the measurement as well as the memory due to the hysteresis but $H_s(\cdot)$ only includes the memory, the measured hysteresis curve has been scaled to eliminate the effect of linear transformations while keeping the memory unchanged. Table 1 shows the VAF (variance accounted for) for all \hat{x}_h extracted from A_1 , A_2 , B_1 and B_2 , with polynomial order $M = 8, 12, 15$, where VAF is defined by:

$$\text{VAF} = \left(1 - \frac{\text{var}(\hat{x}_h - x_{\text{measure}})}{\text{var}(x_{\text{measure}})} \right) \times 100\%. \quad (3.19)$$

x_{measure} is the hysteresis curve from the measurement after scaling and $\text{var}(x_h)$ is the variance of x_h . Even in the worst case, VAF still reaches as high as 99.95%, indicating quite accurate estimation of x_h .

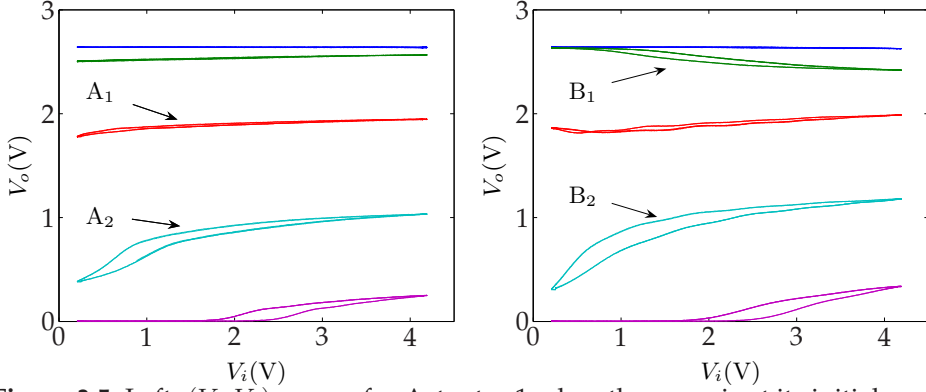


Figure 3.5: Left: (V_i, V_o) curves for Actuator 1 when the razor is at its initial position, tuned by 0.45 mm, 0.52 mm, 0.60 mm and 0.80 mm (top to bottom); right: (V_i, V_o) curves for Actuator 4 when the razor is at its initial position, tuned by 0.37 mm, 0.50 mm, 0.59 mm and 0.80 mm (top to bottom).

Table 3.1: VAF of \hat{x}_h extracted from A_1 , A_2 , B_1 and B_2 , with polynomial order $M = 8, 12, 15$.

M	A_1	A_2	B_1	B_2
8	99.95%	99.96%	99.99%	99.96%
12	99.95%	99.96%	99.99%	99.97%
15	99.95%	99.96%	99.99%	99.97%

Based on the hysteresis curve extracted from A_1 (with $M = 8$, as in Figure 3.6), an inverse Coleman–Hodgdon hysteresis model [60] has been identified and inserted between V_i and HVA to compensate for the hysteresis in the piezo DM. Figure 3.7 shows the resulting (V_i, V_o) curves, where the reduction of hysteresis can be observed clearly compared with Figure 3.5. The largest gaps between two branches in A_1 , A_2 , B_1 and B_2 have been reduced by 67% (0.03 V to 0.01 V), 89% (0.18 V to 0.02 V), 83% (0.06 V to 0.01 V) and 86% (0.21 V to 0.03 V) as in \tilde{A}_1 , \tilde{A}_2 , \tilde{B}_1 and \tilde{B}_2 , respectively, indicating accurate estimation of the hysteresis. Moreover, although the inverse hysteresis model is only based on the hysteresis curve extracted from A_1 , it is still able to correct hysteresis in other conditions like A_2 , B_1 and B_2 , which means good generalization property of the hysteresis estimation.

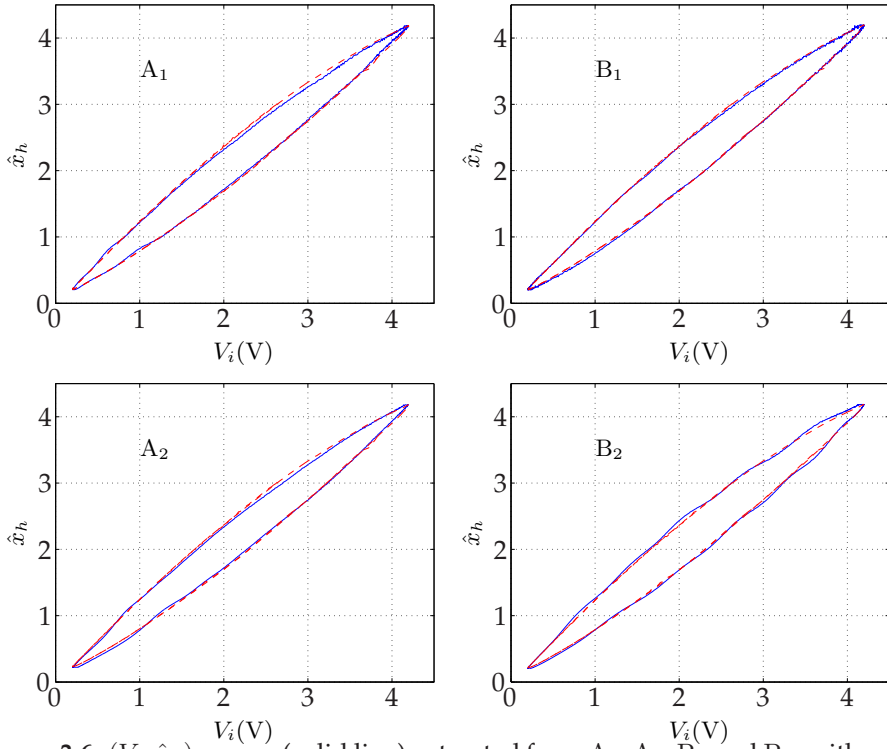


Figure 3.6: (V_i, \hat{x}_h) curves (solid line) extracted from A_1, A_2, B_1 and B_2 , with polynomial order $M = 8$. The hysteresis curve measured by a position sensor (dashed line) is used for comparison.

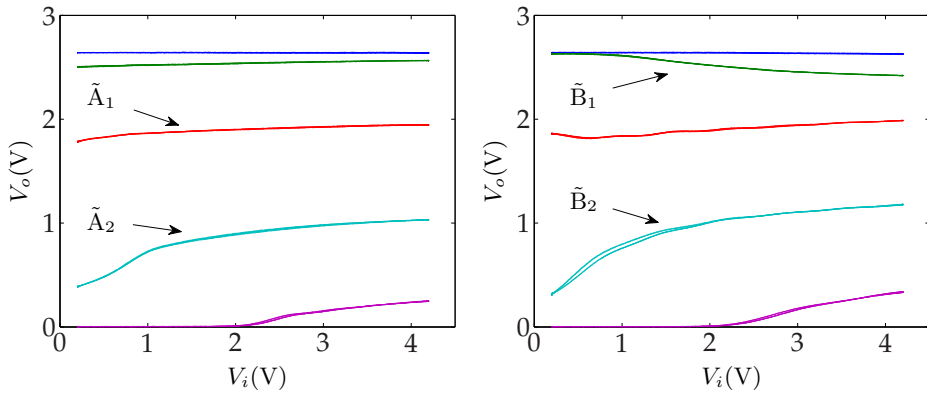


Figure 3.7: (V_i, V_o) curves corresponding to Actuator 1 (left) and 4 (right) after hysteresis compensation. The razor is at the same positions as in Figure 3.5.

3.4.2 Multi-loop hysteresis reconstruction

The algorithm for single-loop hysteresis reconstruction has been verified in Section 3.4.1. However, to identify the inverse Preisach hysteresis model, multiple first-order reverse hysteresis loops are required.

The input voltage V_i has been designed as a periodic signal with decreasing amplitude to contain different extrema, as shown in Figure 3.8. During the experiments, the WFS-less AO system is excited by V_i and the intensity measurement V_o is recorded. The (V_i, V_o) relationship is depicted in Figure 3.9, where the memoryless nonlinear as well as the hysteresis (gaps between the tracing and retracing branches) can be observed clearly. Based on the outermost loop in the (V_i, V_o) relationship, the nonlinearity $f_l^{-1}(\cdot)$ is estimated as in Section 3.4.1 and x_h is estimated by $\hat{x}_h = \hat{f}_l^{-1}(V_o)$ (shown in Figure 3.10).

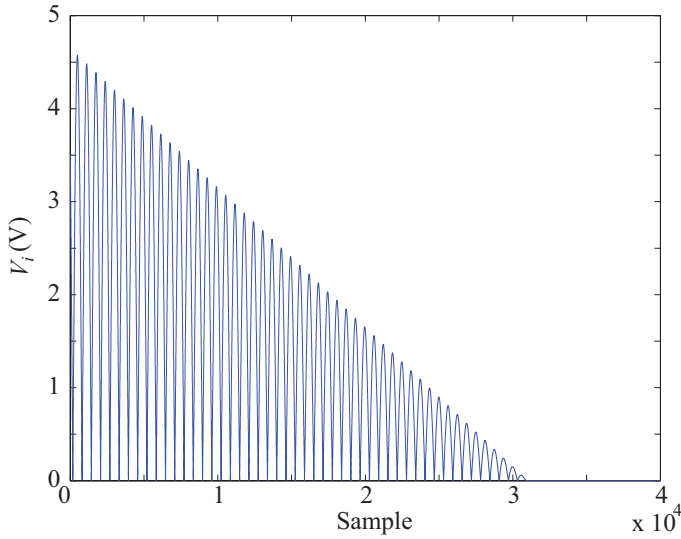


Figure 3.8: Input voltage V_i has been designed as a periodic signal with decreasing amplitude to contain different extremum.

To validate \hat{x}_h , the output voltage V_o is estimated as:

$$\hat{V}_o = \hat{f}_l(\hat{x}_h) \quad (3.20)$$

and compared with V_o from measurement. The error $\epsilon_{V_o} = V_o - \hat{V}_o$ has the root-mean-square (RMS) of 0.007 V and the VAF of 99.99%, indicating accurate estimation of \hat{x}_h and $\hat{f}_l(\cdot)$.

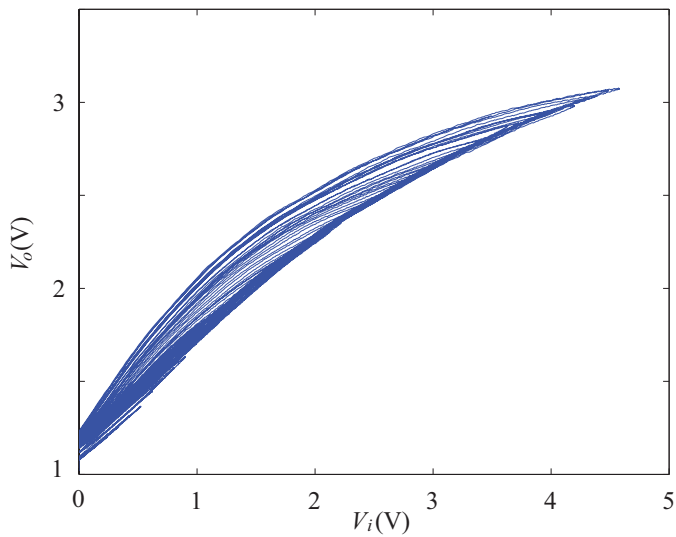


Figure 3.9: Relationship between V_i and V_o , showing hysteresis and nonlinearity in multi-loops.

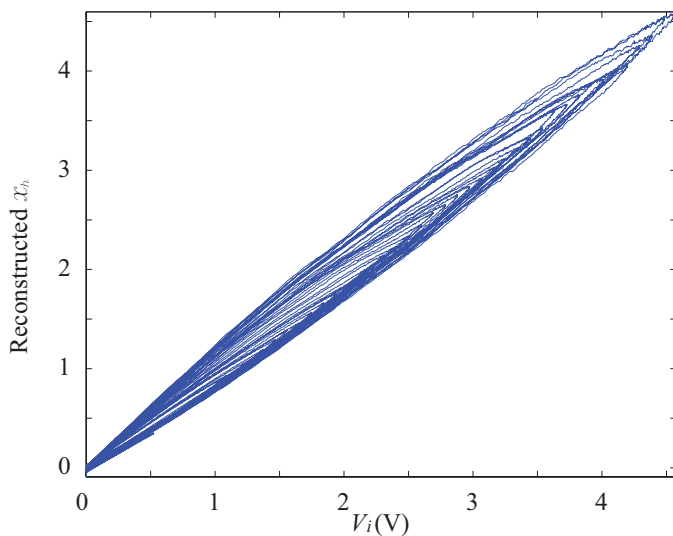


Figure 3.10: Estimated hysteresis curve \hat{x}_h with respect to V_i , where $\hat{x}_h = \hat{f}_l^{-1}(V_o)$. The memory-less nonlinearity has been removed.

3.4.3 Identification of the inverse hysteresis model

To compensate for hysteresis using feed-forward control, the inverse hysteresis model $\hat{H}^{-1}(\cdot)$ is identified with input \hat{x}_h and output V_i . However, the noise in \hat{x}_h makes it difficult to find the local minima and local maxima of \hat{x}_h and it is infeasible to identify the inverse hysteresis model $\hat{H}^{-1}(\cdot)$ directly using \hat{x}_h as an input. In our work, $\hat{H}^{-1}(\cdot)$ is identified in two steps:

1. The Preisach hysteresis model $\hat{H}(\cdot)$ is identified with input V_i and output \hat{x}_h . Because V_i is generated by the controller, the local extrema of V_i can be determined accurately. The Preisach function is approximated by a two-layer feedforward neural network with eight neurons in the first layer and one neuron in the second layer, trained by means of Levenberg-Marquardt backpropagation, using the Matlab neural network toolbox. The output of the model, denoted as $\hat{x}_{h,H} = \hat{H}(V_i)$, is shown in Figure 3.11. The intensity measurement is estimated by $\hat{V}_o = \hat{f}_l(\hat{x}_{h,H})$. The RMS error between V_o and \hat{V}_o is 0.02 V, and the VAF is 99.94%. This indicates that the hysteresis model gives an accurate estimate of \hat{x}_h . A closer observation in $\hat{x}_{h,H}$ shows that $\hat{x}_{h,H}$ is smooth enough that the local extrema of $\hat{x}_{h,H}$ can be determined accurately, which is important for the identification of the inverse hysteresis model.
2. The inverse hysteresis model $\hat{H}^{-1}(\cdot)$ is identified with $\hat{x}_{h,H}$ as input and V_i as output. Since $\hat{x}_{h,H}$ is generated by $\hat{H}(\cdot)$, it is smooth enough that its local maximum and minimum can be determined accurately. The Preisach function is approximated by a two-layer feedforward neural network with eight neurons in the first layer and one neuron in the second layer, trained by means of Levenberg-Marquardt backpropagation, using the Matlab neural network toolbox. The output of the inverse hysteresis model, denoted as \hat{V}_i , is given by

$$\hat{V}_i = \hat{H}^{-1}(\hat{x}_{h,H}). \quad (3.21)$$

Figure 3.12 shows \hat{V}_i with respect to $\hat{x}_{h,H}$. The RMS error between \hat{V}_i and V_i is 0.06 V and the VAF is 99.92%, indicating accurate estimate of V_i by the inverse hysteresis model $\hat{H}^{-1}(\cdot)$ and the nonlinear function $\hat{f}_l^{-1}(\cdot)$.

3.4.4 Hysteresis compensation

To check the effect of the hysteresis compensator, the inverse hysteresis model is inserted right in front of V_i as in Figure 3.4. Various waveforms are applied as the control signal u and the intensity measurement V_o is collected. The voltage V_i is determined by

$$V_i = \begin{cases} \hat{H}^{-1}(u) & \text{HC on,} \\ u & \text{HC off.} \end{cases} \quad (3.22)$$

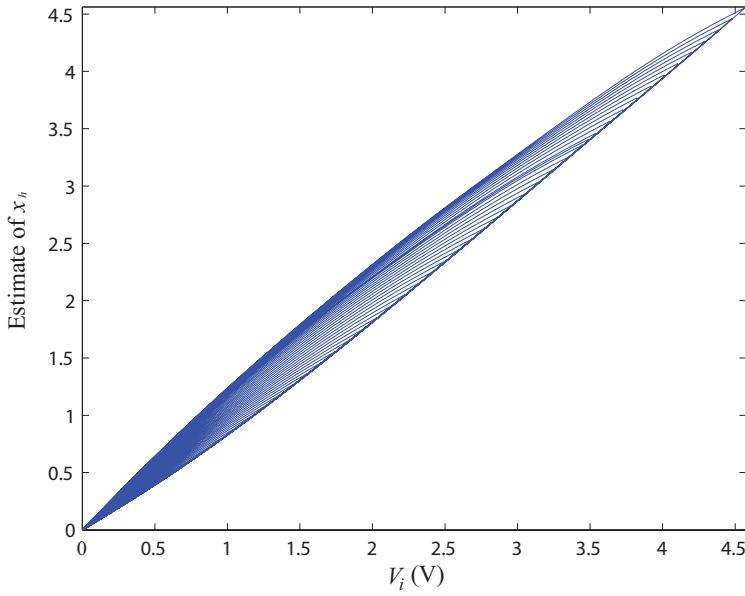


Figure 3.11: Input-output relationship of the Preisach hysteresis model $\hat{H}(\cdot)$, which is identified from V_i and \hat{x}_h . The output of the hysteresis model, $\hat{x}_{h,H}$ is given by $\hat{x}_{h,H} = \hat{H}(V_i)$.

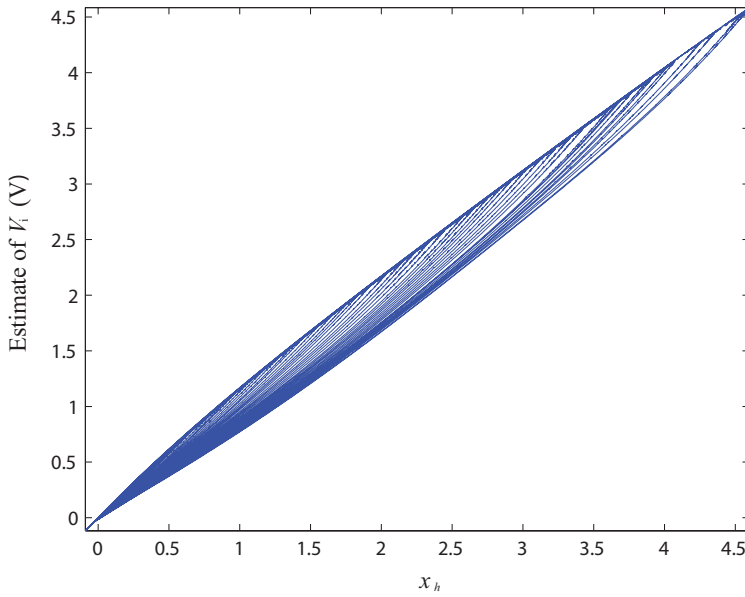


Figure 3.12: Input-output relationship of the inverse Preisach hysteresis model $\hat{H}^{-1}(\cdot)$, which is identified from $\hat{x}_{h,H}$ and V_i . The output of the inverse hysteresis model, \hat{V}_i is given by $\hat{V}_i = \hat{H}^{-1}(\hat{x}_{h,H})$.

The input-output relationship of the system is shown in Figure 3.13 and 3.14. It can be seen that the uncertainty in V_o (visualized as the gap between the loop branches) has been reduced significantly by the inverse hysteresis model. For instance, the difference in V_o for $u = 1.5$ V has been reduced by 88% (from 0.24 V to about 0.03 V) in Test signal 3 and by 73% (from 0.26 V to about 0.07 V) in Test signal 4.

3.5 Conclusion

Hysteresis compensation in a WFSless AO system is done in two steps: 1. extracting hysteresis curves from the nonlinear measurement of the WFSless AO system; 2. identifying an inverse hysteresis model to compensate for the hysteresis in the PDM. Experimental results show that the uncertainty in the WFSless AO system has been reduced significantly, as the gap in the input-output loop has been reduced by about 73% in case of random excitation.

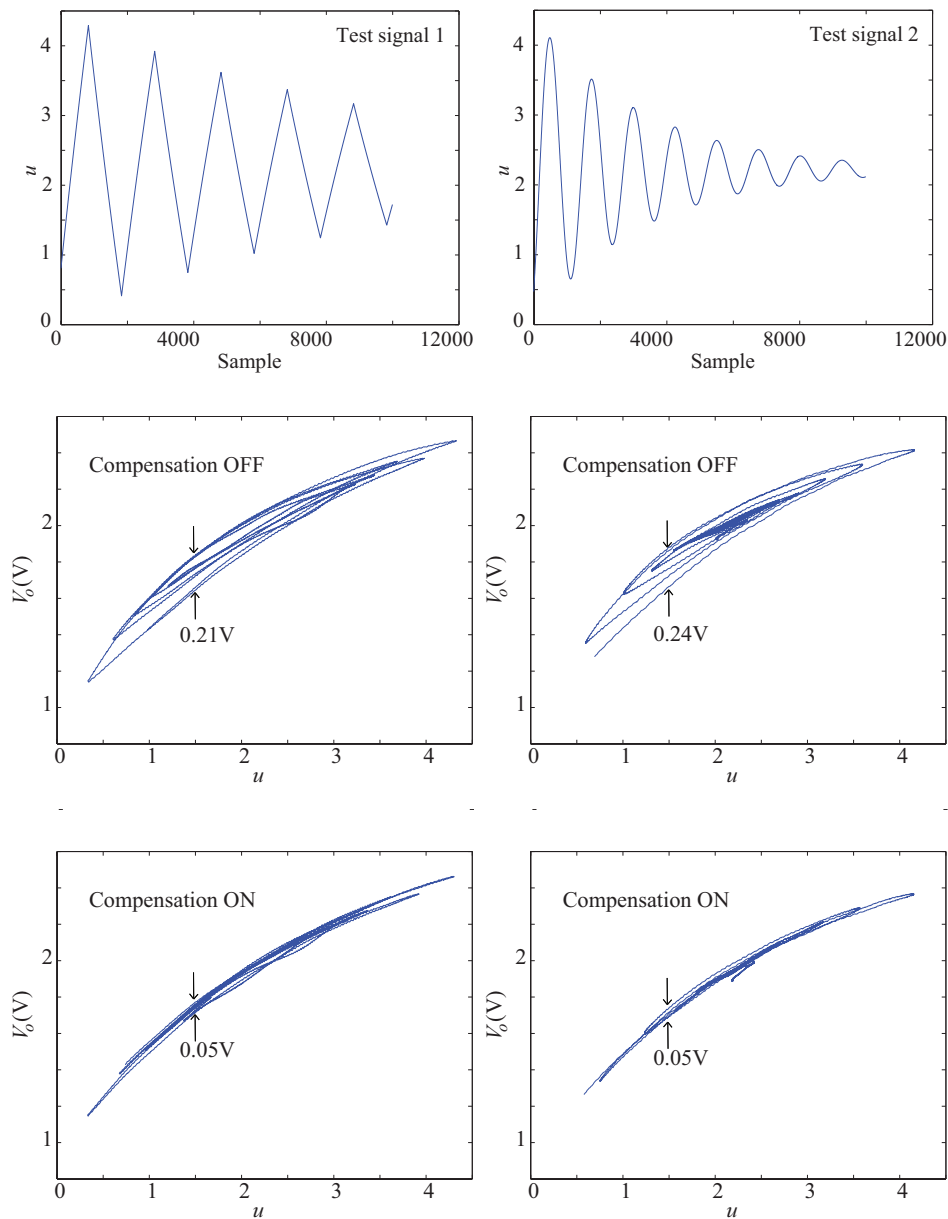


Figure 3.13: Left: with decreasing-amplitude sawtooth test signal; right: with decreasing-amplitude sinusoid test signal. Top: control signal u ; mid: the (u, V_o) relationship with hysteresis compensation off; bottom: the (u, V_o) relationship with hysteresis compensation on. By hysteresis compensation, the largest gaps in the input-output loop of Test Signal 1 and 2 have been reduced by 65% and 81%, respectively.

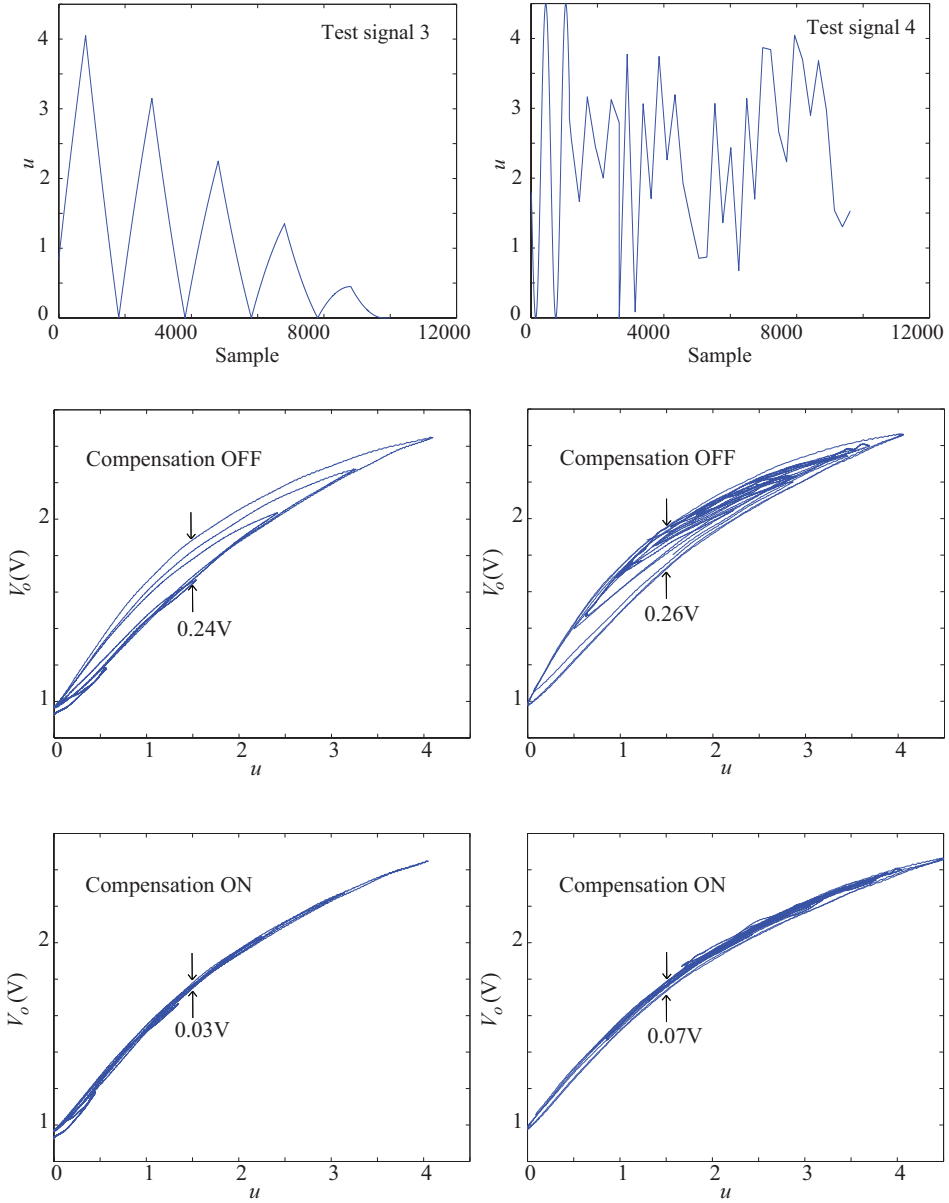


Figure 3.14: Left: with sawtooth-like test signal; right: with random sequence test signal. Top: control signal u ; mid: the (u, V_o) relationship with hysteresis compensation off, i.e., $V_i = u$; bottom: the (u, V_o) relationship with hysteresis compensation on, i.e., $V_i = \hat{H}^{-1}(u)$. By hysteresis compensation, the largest gaps in the input-output loop of Test Signal 3 and 4 have been reduced by 88% and 73%, respectively.

Model-based control in a WFSless AO system

In many scientific and medical applications, such as laser systems and microscopes, wavefront-sensor-less (WFSless) adaptive optics (AO) systems are used to improve the laser beam quality or the image resolution by correcting the wavefront aberration in the optical path. The lack of direct wavefront measurement in WFSless AO systems imposes a challenge to achieve efficient aberration correction. This chapter presents an aberration correction approach for WFSless AO systems based on the model of the WFSless AO system and a small number of intensity measurements, where the model is identified from the input-output data of the WFSless AO system by black-box identification. This approach is validated in an experimental setup with 20 static aberrations having Kolmogorov spatial distributions. By correcting $N = 9$ Zernike modes (N is the number of aberration modes), an intensity improvement from 49% of the maximum value to 89% has been achieved in average based on $N + 5 = 14$ intensity measurements. With the worst initial intensity, an improvement from 17% of the maximum value to 86% has been achieved based on $N + 4 = 13$ intensity measurements.

4.1 Introduction

In recent years, wavefront-sensor-less (WFSless) adaptive optics (AO) systems have been used in many scientific and medical applications, such as laser systems [6, 38–46] and microscopes [47–52, 56, 57], to improve the laser beam quality or the image resolution, by correcting the air-turbulence-, heat- or specimen-induced wavefront aberrations in the optical path. Unlike the AO systems in astronomy applications [1, 3] where the wavefront aberration can be measured directly with dedicated wavefront sensors (e.g., the Shack-Hartmann WFS), there is no direct

wavefront measurement in WFSless AO systems and the sensor signal (e.g., the intensity within a pin hole) is usually nonlinearly related to the wavefront aberration. Aberration correction is performed by adapting the shape of the deformable mirror (DM) such that certain performance metric (e.g., the light intensity measurement or the sharpness of the image) reaches its maximum.

Different optimization algorithms, such as gradient descent optimization algorithm, simplex optimization algorithm, genetic algorithm, simulated annealing algorithm, etc., have been used for aberration correction in WFSless AO systems and the improvements in the performance metric have been demonstrated in [6, 38–51]. By exploring the structure of the performance metric function, model-based approaches have been proposed to speed up the correction [52, 53, 56, 57]. In a recent work by Débarre [57], the performance metric is locally represented as a separable quadratic function of the aberration modal coefficients by sophisticated choice of the aberration modal basis, such that N aberration modes can be corrected after $2N + 1$ images.

In this chapter, we further improve the correction speed of the WFSless AO system by wavefront aberration estimation and correction in three steps. First, with the external aberration absent (e.g., the aberration induced by air turbulence, heat or specimen), the WFSless AO system is calibrated such that the system aberration (e.g., initial aberration in the DM, misalignment of the optical components) is removed. Second, still with the external aberration absent, a nonlinear static model of the calibrated WFSless AO system is identified from the measurement data, which describes the transfer from the DM control signal to the intensity measurement. This step is analogue to determining the influence matrix of the DM in WFS-based AO systems; however, in WFSless AO systems, because the transfer from the DM control signal to the intensity measurement is nonlinear, a nonlinear model identification approach is required. Third, when the external aberration is present, the DM is initially excited by $N + 2$ predefined control signals and the corresponding $N + 2$ intensity measurements are collected. Aberration is estimated and corrected based on these $N + 2$ pairs of input-output data and the model of the WFSless AO system, by solving a nonlinear least squares (NLLS) optimization problem online. With new input-output data available, the aberration estimation and correction are refined iteratively. This approach is validated in a WFSless AO experimental setup and the performance of the resulting closed-loop system is evaluated.

The contribution of this chapter is that a new model-based approach has been proposed and validated for aberration estimation and correction in WFSless AO systems. The chapter is organized as follows. Section 4.2 analyzes the WFSless AO system. Section 4.3 explains our approach on wavefront aberration estimation and correction. Section 4.4 describes the experimental setup. Section 4.5 reports and evaluates the experimental results. Section 4.6 concludes this chapter.

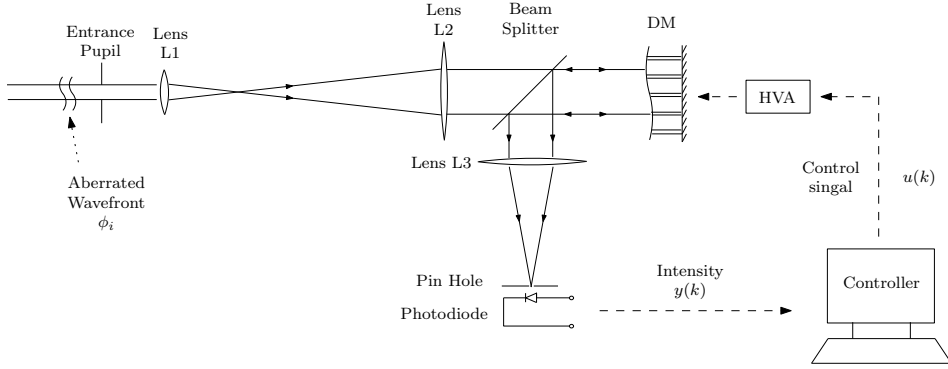


Figure 4.1: Schematic of a common closed-loop WFSless AO system. The incident light beam is disturbed in front of the entrance pupil. The control system adapts the control signal $u(k)$ to maximize the intensity measurement $y(k)$.

4.2 System analysis

The schematic of a common closed-loop WFSless AO system [39,40,53] under investigation is depicted in Figure 4.1. The incident light beam is disturbed in front of the entrance pupil. The entrance pupil is conjugated to the DM by two lenses L1 and L2. After the beam is reflected by the DM, it is focused by the lens L3. A pin hole is placed at the focal point of L3. After the pin hole, a photodiode measures the intensity within the pin hole and feeds the intensity measurement to the control system. The control objective is to maximize the intensity measurement $y(k) \in \mathbb{R}$ at time k by adapting the control signal $u(k) \in \mathbb{R}^N$ to the DM, i.e,

$$\max_{u(k)} y(k), \quad (4.1)$$

where $u(k)$ can be the zonal or modal representation of the control signal, with dimension N .

By physical modeling (referring to [13] and Eq. (1.5)-(1.7)), the light intensity measurement $y(k)$ is related to the incident wavefront aberration and the DM deformation as:

$$y(k) = S_\lambda \iint_{\Sigma_2} \left| \iint_{\Sigma_1} a_i(\xi, \eta, k) \exp[-j \frac{2\pi}{\lambda} (\phi_x(\xi, \eta, k) + \phi_m(\xi, \eta, k))] \cdot \exp[-j \frac{2\pi}{\lambda d} (\alpha \xi + \beta \eta)] d\xi d\eta \right|^2 d\alpha d\beta + \nu(k). \quad (4.2)$$

Here (ξ, η) and (α, β) represent the coordinates in the input plane and the focal plane of the lens L3, respectively, and with $j = \sqrt{-1}$. $a_i(\xi, \eta, k)$ is the amplitude of the complex optical field at time instant k . $\phi_x(\xi, \eta, k)$ and $\phi_m(\xi, \eta, k)$ represent

the incident wavefront aberration and wavefront manipulation by the DM at time k , respectively. The phase of the complex optical field is given by $\phi_x(\xi, \eta, k) + \phi_m(\xi, \eta, k)$. λ is the wavelength of the light and d the focal distance of L3. Σ_1 represents the illuminated area of L3 and Σ_2 the area of the pin hole. $\nu(k)$ is the measurement noise. S_λ is the sensitivity of the photodiode at wavelength λ .

Because in many cases wavefront aberration is the main factor for intensity measurement reduction at given incident light power [48, 52, 56], the amplitude variation in the optical field is omitted such that

$$a_i(\xi, \eta, k) = a_i, \quad (4.3)$$

where a_i is a constant. Apart from that, if the aberration is corrected within a short time, it is reasonable to consider the wavefront aberration as constant (e.g., when any single point in the specimen is imaged in scanning-type microscopes under normal operational conditions). This simplifies $\phi_x(\xi, \eta, k)$ as

$$\phi_x(\xi, \eta, k) = \phi_x(\xi, \eta), \quad (4.4)$$

such that $\phi_x(\xi, \eta)$ is time-independent.

The speed of aberration correction generally depends on the correction algorithm and the sampling rate of the WFSless AO system. As the sampling rate increases, the dynamics in the DM becomes more significant. Since the static nonlinearity in the intensity measurement is a common bottleneck for efficient aberration correction in WFSless AO systems while the DM dynamics is device- and sampling-rate- dependent, in this chapter we focus on the static nonlinearity in the intensity measurement. Dynamics in the DM at high sampling rate is left for future research. In this case, the DM wavefront manipulation $\phi_m(\xi, \eta, k)$ can be written as

$$\phi_m(\xi, \eta, k) = D(\xi, \eta)u(k) \quad (4.5)$$

where $D(\xi, \eta)$ represents the static linear response of the DM. This linear representation of the DM response is valid for most commonly-used DMs when they are appropriately linearized, e.g, taking the square root of the voltage as the control signal for electrostatic-actuated DM [39], or by hysteresis compensation in piezo-driven DM [94]. Each column of $D(\xi, \eta)$ can be considered as a mode of the DM deformation and $u(k)$ contains all the modal coefficients. The column space of $D(\xi, \eta)$ forms a basis for $\phi_m(\xi, \eta, k)$. Different basis can be used (e.g., DM actuator basis, Zernike basis, Lukosz basis), depending on how the control signal $u(k)$ is defined. For instance, if $u(k)$ is same as the voltage applied to each actuator of the DM (i.e, zonal control), then $D(\xi, \eta)$ is the influence function of the DM; otherwise, Zernike modal control or Lukosz modal control can also be applied.

Combining Eq. (4.2)-(4.5), the behavior of the WFSless AO system can be represented as

$$y(k) = S_\lambda \iint_{\Sigma_2} \left| \iint_{\Sigma_1} a_i \exp[-j \frac{2\pi}{\lambda} (\phi_x(\xi, \eta) + D(\xi, \eta)u(k))] \right|$$

$$\cdot \exp[-j \frac{2\pi}{\lambda d} (\alpha\xi + \beta\eta)] d\xi d\eta]^2 d\alpha d\beta + \nu(k). \quad (4.6)$$

Static nonlinearity is visible in Eq. (4.6) in the wavefront-intensity mapping. Because this mapping is surjective (i.e., different wavefronts can give the same intensity measurement) and not invertible, the wavefront can not be obtained from single intensity measurement. However, with the model of the WFSless AO system describing the transfer from $u(k)$ to $y(k)$ with the aberration $\phi_x(\xi, \eta)$ absent, and at least $N + 2$ pairs of $u(k)$ to $y(k)$ collected with $\phi_x(\xi, \eta)$ present, the aberration $\phi_x(\xi, \eta)$ can be estimated in the basis defined by $D(\xi, \eta)$, as will be explained in Section 3.

4.3 Model-based aberration estimation and correction

4.3.1 Modeling of the WFSless AO system

Because the DM deformation $\phi_m(\xi, \eta)$ can not be measured in the WFSless AO system and $D(\xi, \eta)$ can not be obtained with high accuracy, it is difficult to get an accurate model of the real system from Eq. (4.6). The artifacts in the optical components may also degrade the accuracy of Eq. (4.6). As will be shown later on, since hundreds of times of intensity calculations are needed by our proposed algorithm to estimate the aberration, the computational complexity in Eq. (4.6) (e.g., two double integrals for each intensity calculation) will slow down the aberration correction speed. Therefore in our work the AO model is identified directly from $\{u(k), y(k)\}$ by black-box identification [95, 96].

In this sense, the system description in Eq. (4.6) is represented by

$$y(k) = g(\phi_x(\xi, \eta) + D(\xi, \eta)u(k)) + \nu(k), \quad (4.7)$$

where g represents the static nonlinear wavefront-intensity mapping, including the double integral over the coordinate (ξ, η) . The wavefront aberration $\phi_x(\xi, \eta)$ can be split into two parts as

$$\phi_x(\xi, \eta) = \underbrace{D(\xi, \eta)x}_{\phi_1(\xi, \eta)} + \Delta\phi_x(\xi, \eta). \quad (4.8)$$

Here $\phi_1(\xi, \eta)$ represents the part of $\phi_x(\xi, \eta)$ lying within the range of the mapping $D(\xi, \eta)$ and $\Delta\phi_x(\xi, \eta)$ represents the part of $\phi_x(\xi, \eta)$ which is orthogonal to the range of $D(\xi, \eta)$. It is assumed that the wavefront aberration can be represented by a finite low-order Zernike aberrations [52, 97, 98], then it is possible that the DM can generate these low-order Zernike modes efficiently and $\Delta\phi_x(\xi, \eta)$ can be neglected. As a result, Eq. (4.8) can be approximated by

$$\phi_x(\xi, \eta) \approx D(\xi, \eta)x. \quad (4.9)$$

Substitute Eq. (4.9) into (4.7), we have

$$y(k) \approx g(D(\xi, \eta)(x + u(k))) + \nu(k). \quad (4.10)$$

Merging $D(\xi, \eta)$ and g into one static nonlinear mapping f , we can further simplify the system description as

$$y(k) \approx f(x + u(k)) + \nu(k). \quad (4.11)$$

Eq. (4.11) considers the aberration as a disturbance directly applied on the input $u(k)$, which allows to identify the model of the WFSless AO system only based on $u(k)$ and $y(k)$ but meanwhile accounting for the influence of the aberration.

To identify an accurate nonlinear model of the WFSless AO system from $u(k)$ and $y(k)$, the nonlinearity in the system should be excited persistently by the input $u(k)$. Random signals can then be used to excite the system for data collection. Since f is identified only based on $u(k)$ and $y(k)$, $y(k)$ should be collected with $x = 0$. If $x = x_0 \neq 0$ (x_0 is an unknown non-zero constant vector) during the data collection, then there is an offset of x_0 in the estimated aberration, as will be seen in the next section. In practice, this aberration-free condition may be achieved after the calibration of the WFSless AO system, when the aberration of the WFSless AO system itself (system aberration, e.g., initial aberration in the DM, misalignment of the optical components) has been corrected and the aberration induced by external sources (e.g., air turbulence, high power heating or specimen) is still absent. The system aberration can be corrected by optimization algorithms like simplex algorithm, genetic algorithm, etc. Although optimization algorithm is used here for system aberration correction, the system aberration only needs to be corrected once during the operation of the WFSless AO system. Significant time can still be saved in correcting the external aberrations.

With the input-output data $u(k)$ and $y(k)$, the model structure needs to be selected for the nonlinear black-box model. There is a very rich spectrum of possible descriptions for nonlinear black-box models, e.g., neural network [99, 100], fuzzy models [101], etc. Because a 2-layer neural network is able to model a broad range nonlinearities and, from practical point of view, it can be implemented and trained with the MATLAB Neural Network Toolbox [85] very conveniently, a 2-layer neural network is built in our work, with N_Q neurons in the first layer and one in the second. The output $\hat{y}(k)$ of the neural network is determined as

$$\hat{y}(k) = \hat{f}(u(k)) = W_1 \tanh(W_2 u(k) + s_1) + s_2. \quad (4.12)$$

$W_2 \in \mathbb{R}^{N_Q \times N}$ and $W_1 \in \mathbb{R}^{1 \times N_Q}$ contain the input and output weights of the neural network, respectively; $s_1 \in \mathbb{R}^{N_Q \times 1}$ and $s_2 \in \mathbb{R}$ are biases on the input and output neurons, respectively. \tanh is the hyperbolic tangent function. Parameters W_1 , W_2 , s_1 and s_2 can be optimized by training the neural network with sufficient data points $u(k)$ and $y(k)$. Details on training and validating the neural network can be found, for instance, in [99, 100].

4.3.2 Aberration estimation and correction

With the unknown aberration x present, if the WFSless AO system is excited by a certain number of inputs $u(k)$, $k = 1, \dots, K$ (K is the number of data points) and the intensity $y(k)$, $k = 1, \dots, K$, are collected, then x can be estimated by solving a set of nonlinear equations as

$$\begin{cases} y(1) &= a\hat{f}(x + u(1)) \\ y(2) &= a\hat{f}(x + u(2)) \\ \vdots &\vdots \\ y(K) &= a\hat{f}(x + u(K)) \end{cases} \quad (4.13)$$

Here \hat{f} is the model of the WFSless AO system identified in previous step. a is a scaling factor, accounting for the possible variation in the incident light power between the modeling and aberration estimation. For instance, in microscopes, the light power emitted or reflected by the specimen may vary from point to point. The obstructing layers of the specimen may also scatter, reflect or absorb the light passing through. Although we are only interested in x for aberration correction, a should also be estimated because it is unknown in Eq.(4.13).

To obtain an analytical solution of Eq.(4.13) may be infeasible in practice, for instance, if the nonlinearity \hat{f} has some high-degree components. Alternatively, a numerical solution can be obtained by solving a nonlinear least squares (NLLS) problem as

$$(\hat{a}, \hat{x}) = \arg \min_{\hat{a}, \hat{x}} \underbrace{\|Y_{[1,K]} - \hat{Y}_{[1,K]}\|_2^2}_{J(\hat{a}, \hat{x})}, \quad (4.14)$$

with $Y_{[1,K]}$ and $\hat{Y}_{[1,K]}$ constructed as

$$Y_{[1,K]} = \begin{bmatrix} y(1) \\ y(2) \\ \vdots \\ y(K) \end{bmatrix}, \quad \hat{Y}_{[1,K]} = \begin{bmatrix} \hat{y}(1) \\ \hat{y}(2) \\ \vdots \\ \hat{y}(K) \end{bmatrix} = \begin{bmatrix} \hat{a}\hat{f}(\hat{x} + u(1)) \\ \hat{a}\hat{f}(\hat{x} + u(2)) \\ \vdots \\ \hat{a}\hat{f}(\hat{x} + u(K)) \end{bmatrix}. \quad (4.15)$$

Here \hat{a} and \hat{x} are the estimates of a and x , respectively. For given \hat{a} and \hat{x} , the intensity is estimated by $\hat{y}(k) = \hat{a}\hat{f}(\hat{x} + u(k))$.

To have an efficient aberration correction, a compromise should be made in K concerning the accuracy of the aberration estimation and the correction speed. From one hand, inadequate data points can not give an accurate aberration estimation, for instance, more than one solutions may exist in Eq. (4.13) and the cost function $J(\hat{a}, \hat{x})$ in Eq. (4.14) does not have a unique global minimum (see Figure 4.2 for an illustration). From the other hand, if more data points are collected than necessary, then the correction speed will be slowed down. A theoretical analysis on this is difficult because several factors should be considered, e.g., the nonlinear-

ity f , the model uncertainty in \hat{f} , the measurement noise in $y(k)$ and the values of the K inputs. However, as a practical solution, aberration estimation and correction can be implemented in an iterative manner and the model-based aberration correction (MBAC) algorithm is described below.

- (1) Before the aberration estimation, the WFSless AO system is initially excited by $N + 2$ control signals $u(k)$ and the corresponding intensity measurements $y(k)$ are collected. Here $N + 2$ data points are collected for initialization due to the concerns that $N + 1$ unknowns need at least $N + 1$ equations in Eq. (4.13) to have a unique solution if f were a linear function, and that non-linear functions may need more equations in general. Since the aberration estimation and correction will be refined iteratively later on, these $N + 2$ data points serves as an initial trial for the MBAC algorithm. A natural option for the first control signal is $u(1) = 0$, i.e., no correction by the DM. The other $N + 1$ control signals should excite the aberrated system in such a way that rich information can be collected on the aberration x . Selection of such $N + 1$ inputs has been investigated in [53]. The optimum distribution of the $N + 1$ inputs can be geometrically interpreted as the $N + 1$ vertices of a regular simplex in the N -dimensional space (see Appendix B of [53]).
- (2) From time $k = N + 2$ on, the aberration estimation (denoted as $\hat{x}(k - 1)$) is given by Eq. (4.14), based on previous $K = k - 1$ control inputs and intensity measurements. The control input is then set as $u(k) = -\hat{x}(k - 1)$ to counter-react on the aberration and the corresponding intensity $y(k)$ is measured. The newly-collected $y(k)$ and $u(k)$ are added into $Y_{[1,K]}$ and $\hat{Y}_{[1,K]}$ respectively in Eq. (4.15) and the aberration estimation can be refined by solving Eq. (4.14) with the latest $Y_{[1,K]}$ and $\hat{Y}_{[1,K]}$. This estimation-correction-collection procedure can be repeated iteratively. The algorithm can be stopped when a certain criterion is met, for instance, when the improvement over the previous intensity measurement is less than a certain threshold value, or when the maximum number of intensity measurements is exceeded.

Due to the modeling uncertainty in \hat{f} and the measurement noise in $y(k)$, the accuracy of the aberration estimation may be limited and the intensity may not reach its maximum by the MBAC algorithm. In this situation, other optimization algorithms like simplex algorithm, genetic algorithm, etc., can be used to continue searching for the optimum. Under the assumption that \hat{f} is a close approximation of f , the MBAC algorithm will steer the DM to a point close to its optimum. This point can then be used as a new initial condition for desired nonlinear optimization method, like the simplex algorithm described in [102]. The initial simplex of the simplex algorithm is constructed around the control signal which gives the maximum intensity measurement in the MBAC algorithm. The hybrid algorithm (MBAC+Simplex) is described in pseudo code below. The MBAC algorithm stops after a fixed number of intensity measurements P (P is a user-defined number), to distinguish the intensity improvements due to the MBAC algorithm and due to the simplex algorithm. The simplex algorithm stops at time \tilde{P} (\tilde{P} is a user-defined

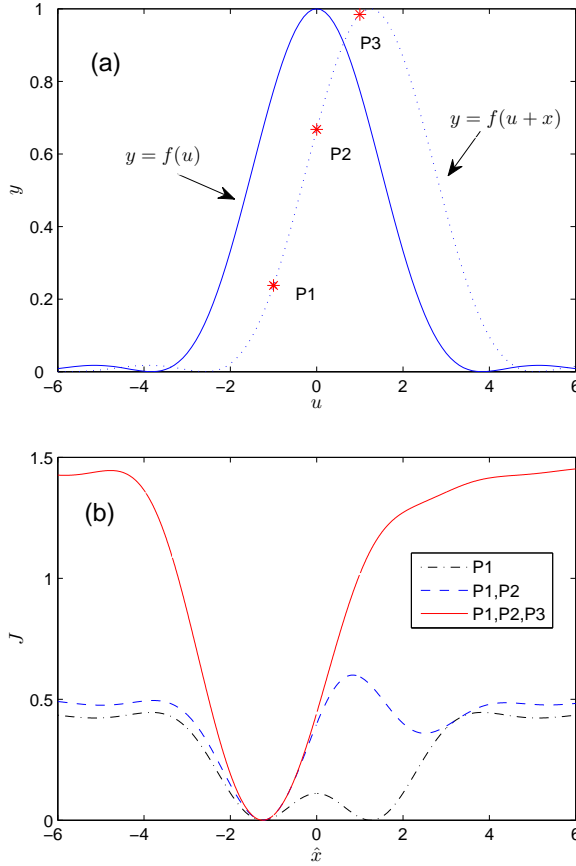


Figure 4.2: Cost function $J(\hat{x})$ depends on the number of data points for solving the NLLS problem in Eq.(4.14). For clarity of explanation, the intensity variation a is not considered. In (a), the nonlinearity is represented as $y = f(x+u) = \left(\frac{2J_1(x+u)}{x+u}\right)^2$ to simulate the intensity distribution in the Airy disk [5], with J_1 the Bessel function of the first kind. The aberration shift the original system $y = f(u)$ horizontally by $x = -1.25$. The model uncertainty is neglected, i.e., $\hat{f} = f$. With single data point P1, the cost function $J(\hat{x})$ has two minima at $\hat{x} = -1.25$ and $\hat{x} = 3.25$ as plotted in (b). With points P1 and P2, $J(\hat{x})$ has one unique global minimum at $\hat{x} = -1.25$ but there is a local minimum at $\hat{x} = 2.5$. This local minimum vanishes when P3 is added and the domain of convex is increased.

number).

MBAC+Simplex algorithm (general description and *pseudo code implementation*):

- (1) Initialization of MBAC, i.e., collecting $N + 2$ data points
 - Set $u(1) = 0$.
 - Set $u(k)$ as in Appendix B of [53], with $k = 2, \dots, N + 2$.
 - Set $\hat{a}(k) = 1$, with $k = 1, \dots, N + 2$.
 - for $k = 1 : N + 2$
 - Excite the WFSless AO system with $u(k)$ and collect $y(k)$.
 - end
- (2) Aberration estimation and correction by MBAC
 - for $k = N + 3 : P$
 - $p = \arg \max_p y(p)$;
 - $\hat{a}_{init} = \hat{a}(p)$, $\hat{x}_{init} = -u(p)$;
 - $[\hat{a}(k - 1), \hat{x}(k - 1)] = \arg \min_{\hat{a}, \hat{x}} J(\hat{a}, \hat{x})$ as in Eq.(4.14), with initial conditions \hat{a}_{init} and \hat{x}_{init} .
 - Set $u(k) = -\hat{x}(k - 1)$, excite the system with $u(k)$ and collect $y(k)$.
 - end
- (3) Aberration correction by the simplex algorithm
 - $p = \arg \max_p y(p)$;
 - $u_c = u(p)$;
 - Construct simplex around u_c as $u(k) = u(k - P + 1) + u_c$ with $k = P + 1, \dots, P + N + 1$.
 - for $k = P + 1 : \tilde{P}$
 - Run simplex algorithm as in [102].
 - end

4.4 Experimental setup

To validate the proposed algorithm for model-based aberration correction, a WFSless AO setup has been built in the Smart Optics Lab in DCSC. Figure 4.3 shows the photo of the WFSless AO setup.

The collimated laser beam is generated by a He-Ne laser with a wavelength of 632 nm. Aberration is generated by a circular glass plate. One side of the glass plate is polished such that the resulting wavefront aberration has a spatial Kolmogorov distribution [1]. The intensity transmission of the disturbance generator is about 78% as measured by a power meter (PM100, Thorlabs, Germany). During the modeling of the WFSless AO system, this aberration generator is removed.

The entrance pupil has a diameter of 6 mm. It is conjugated to the PDM by lenses L1 and L2. The focal distances of L1 and L2 are 6 cm and 20 cm, respectively. The PDM (37-actuator, OKOTech, The Netherlands) has a clear aperture of 30 mm and only the central area with a radius of 20 mm is illuminated to generate Zernike modes efficiently [98]. The high voltage amplifier (HVA, OKOTech, The Netherlands) has 40 channels, each with an output range of 0~300 V, a voltage amplification of 80 at low frequencies and a -3dB bandwidth of 1 kHz. Lens L3 has a focal distance of 400 mm. The pin hole (NT56-282, Edmunds Optics, with a diameter of 50 μm) is placed at the focal point of L3, followed by a photodiode (TSL250R-LF, TAOS, Korea) measuring the light intensity inside the pin hole.

Referring to Figure 4.4, signal generation and data acquisition is accomplished by a dSPACE system with a Simulink diagram. The Simulink diagram is compiled and loaded by the dSPACE process board (DS1006, dSPACE, Germany). The digital-to-analog (DA) card (DS2103) has an output range of ± 10 V, a resolution of 14-bit. The analog-to-digital (AD) card (DS2004) has an input range of ± 10 V and a resolution of 16-bit. The control algorithm is implemented in MATLAB (Version 7.5.0.342, The MathWorks). Interfacing between MATLAB and the dSPACE system is done via MLIB (dSPACE, Germany).

Figure 4.5 depicts the block diagram of the closed-loop WFSless AO system. The physical input of the WFSless AO system is the voltage $V(k) \in \mathbb{R}^{37}$, which is applied to 37 actuators of the PDM. The output of the WFSless AO system is the light intensity measurement $y(k) \in \mathbb{R}$ from the photodiode. To reduce the uncertainty in the AO setup, a hysteresis compensator \hat{H}^{-1} is implemented to compensate for the hysteresis in the PDM as discussed in Chapter 3. To reduce the dimension of the control signal $u(k) \in \mathbb{R}^N$, the PDM is controlled in Zernike basis by $N = 9$ modes. This is accomplished by the matrix $L \in \mathbb{R}^{37 \times N}$ which transforms the modal control signal $u(k)$ to the pseudo voltage $\tilde{V}(k)$. L is derived according to the Zernike polynomials description in [97] and the theoretical model of the PDM in [92]. The indexing of Zernike modes is the same as in [97]. Only Zernike-Mode 2 to 10 are controlled (i.e., piston is neglected). With the hysteresis compensator and the modal transformer, the WFSless AO system is conceptually considered to have the modal control signal $u(k)$ as input and intensity measurement $y(k)$ as output. The intensity measurement is fed into the controller and the control signal $u(k)$ is calculated.

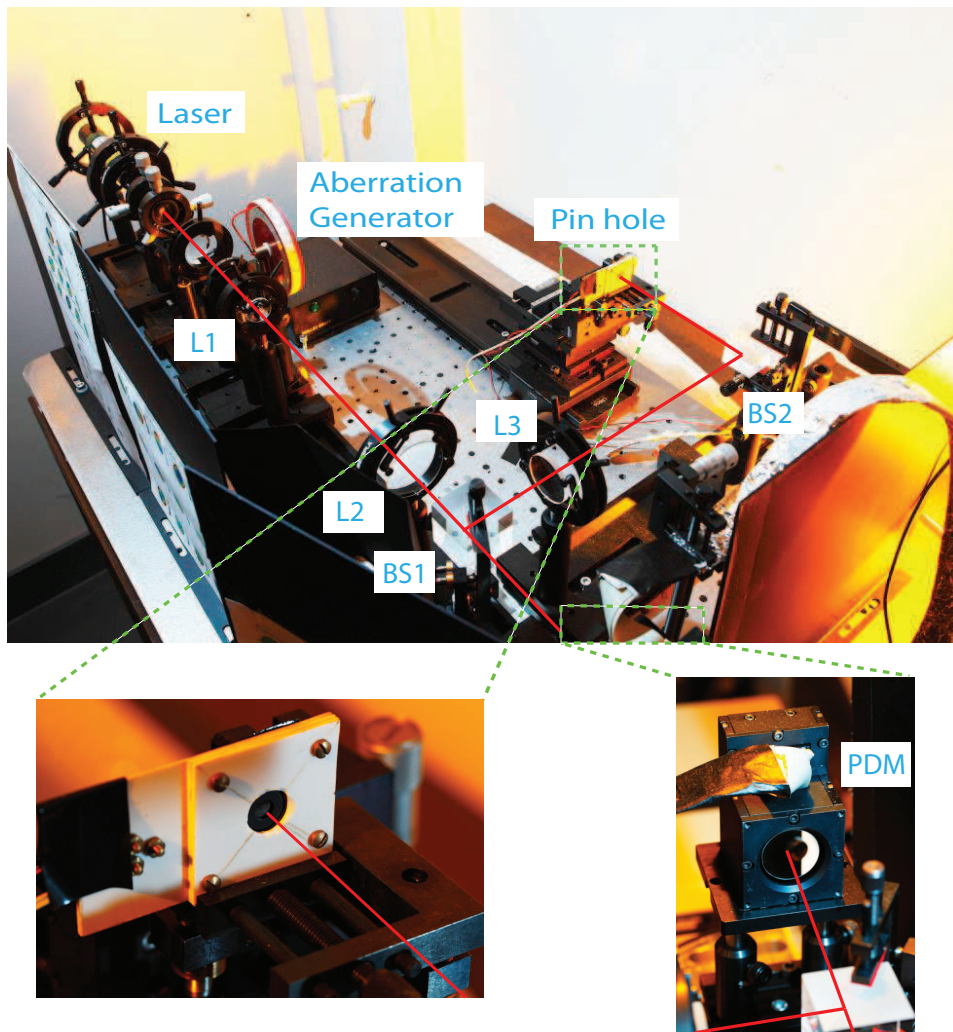


Figure 4.3: Photo of the experimental WFSless AO setup in the laboratory in DCSC. The images of the pin hole (bottom left) and the 37-actuator PDM (bottom right) are zoomed in.

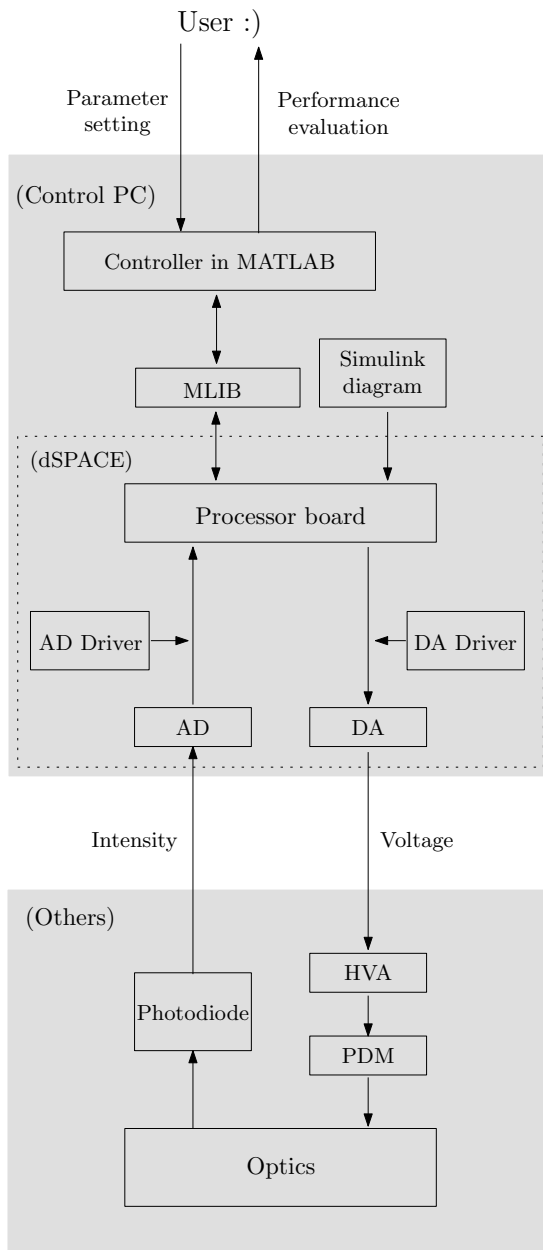


Figure 4.4: Structure of the control system in the WFSless AO setup. Signal generation and data acquisition is done by dSPACE. Aberration is estimated in MATLAB.

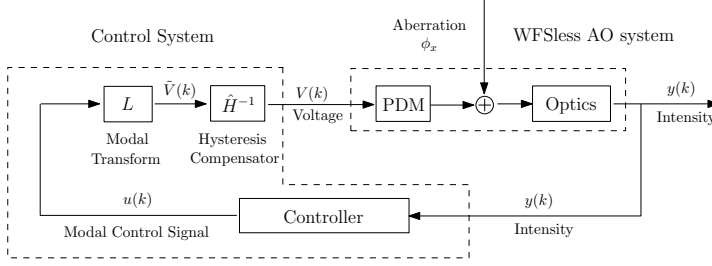


Figure 4.5: Block diagram of the closed-loop WFSless AO system. The physical WFSless AO system has voltage $V(k)$ as input, but conceptually $u(k)$ can be considered as its input because of the hysteresis compensator and the modal transform.

4.5 Experiments and results

Experiments have been carried out in the setup described in Section 4 to validate the proposed approach for aberration correction, which mainly consist of three steps as follows:

- (1) With the aberration generator absent, the WFSless AO system is calibrated using a simplex optimization algorithm. The system aberration is corrected by adapting the shape of the PDM such that the intensity measurement is maximized.
- (2) The WFSless AO system is excited by random control signals $u(k)$ and the intensity measurements $y(k)$ are collected. Based on $u(k)$ and $y(k)$, the WFSless AO system is modeled by a neural network as described in Section 3.1.
- (3) Aberration is introduced in the WFSless AO system by the aberration generator and corrected by the proposed MBAC+Simplex algorithm as described in Section 3.3. For a comparison, the simplex algorithm alone is also used to correct the aberration. Intensity improvements by these two algorithms are evaluated and compared.

4.5.1 System calibration

To allow for bi-directional operation of the PDM in later experiments, all the actuators in the PDM are biased by 150 V initially. A simplex optimization algorithm is then used to correct the system aberration, which maximizes the intensity measurement $y(k)$ by adapting the control signal $u(k)$ as in Eq. (4.1). The sampling rate of the system during the calibration is $f_s = 50$ Hz, which is much less than the resonance frequency of the PDM (about 1 kHz), so that the AO system is considered static. The maximum intensity measurement is denoted as y_{max} , which is

used to normalize intensity measurement in Section 5.3. The control signal which results in the maximal intensity measurement, denoted as u_0 , is used as a bias in all the following experiments.

4.5.2 Modeling of the nonlinear AO system

To collect enough input-output data for modeling the WFSless AO system, the system is excited by 10000 control signals $u(k)$ in open-loop with the aberration generator absent and the intensity measurements $y(k)$ are collected. The control signals $u(k)$ distribute randomly within the operational range of the PDM, to give a persistent excitation. The sampling rate of the system is also 50 Hz.

Among the 10000 collected data points, 6000 are randomly selected for identification of the AO model and the rest 4000 are for validation. The AO system is modeled as a 2-layer feedforward neural network with N_Q neurons in its first layer and one neuron in its second layer as in Eq. (4.12). The neural network is implemented and trained by MATLAB Neural Network Toolbox [85]. Parameters W_1 , W_2 , s_1 and s_2 in Eq. (4.12) are optimized by minimizing the mean square of the fitting error, using Levenberg-Marquardt (LM) backpropagation algorithm, i.e.,

$$(W_1, W_2, s_1, s_2) = \arg \min_{(W_1^*, W_2^*, s_1^*, s_2^*)} \frac{1}{N_t} \sum_{k=1}^{N_t} (y(k) - \hat{y}(k))^2. \quad (4.16)$$

N_t is the number of data points for identification, in our case, $N_t = 6000$.

The accuracy of the model is evaluated by calculating the variance accounted for (VAF) of the model, which is defined as

$$\text{VAF}(\hat{y}, y) = \left(1 - \frac{\text{var}(\hat{y} - y)}{\text{var}(y)} \right) \times 100\%. \quad (4.17)$$

Here $\text{var}(y)$ is the variance of y . Figure 4.6 shows the VAFs of the AO model with different number of neurons in the first layer. From this plot, it can be seen that VAF already reaches as high as 98.2% at $N_Q = 20$ for the identification set and 97.8% for the validation set, indicating that the neural network can model the AO system very accurately. The difference in VAF is negligible for $N_Q > 20$. Therefore 20 neurons are used in the first layer, to have a good balance between the model accuracy and the model complexity.

4.5.3 Aberration correction

The aberration generator is inserted in the optical path as in Figure 4.1. The MBAC+Simplex algorithm is used to correct the aberration. To have a statistics of the performance, experiments have been carried out for 20 static aberrations, which are generated by rotating the circular glass plate such that the beam is disturbed by different regions of the glass plate.

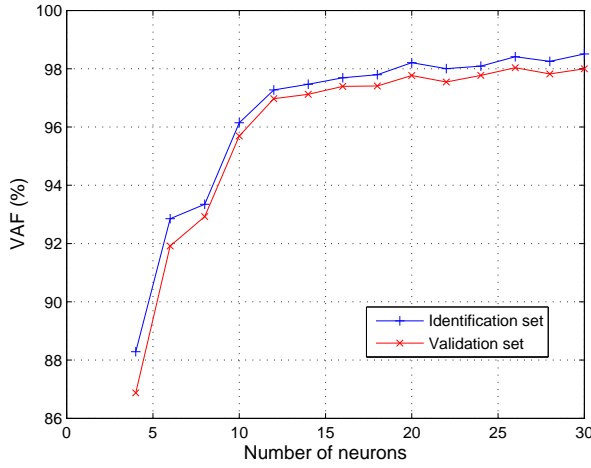


Figure 4.6: Accuracy of the neural network model for different number of neurons N_Q . VAF increases with N_Q in both identification and validation sets for $N_Q \leq 20$. The difference in VAF is negligible for $N_Q > 20$. Hence 20 neurons are used.

Figure 4.7 shows the time line of the WFSless AO system. In each experiment, during the initialization, the aberrated system is excited by $N + 2 = 11$ control signals $u(k)$, $k = 1, \dots, N + 2$, at a rate of 50 Hz. Inputs $u(k)$ are initialized as in Section 3.3. The amplitude of the simplex is selected as half of the operational range of the PDM. After the intensity $y(k)$, $k = 1, \dots, N + 2$, are collected, the aberration is estimated by solving a NLLS optimization problem as in Eq. (4.14), using the function *fmincon* in MATLAB Optimization Toolbox. *fmincon* is used in our work because: (1) it is computationally very efficient and can be called in MATLAB very conveniently; (2) the convexity of $J(\hat{a}, \hat{x})$ improves with more data points so that a local optimization algorithm like *fmincon* may already be enough to get an accurate estimation \hat{a} and \hat{x} . \hat{a} is constrained to be within $[0, 1]$ during the estimation. As time keeps going, more data points are available and the aberration is estimated and corrected iteratively as in the MBAC+Simplex algorithm. After $P = 19$ data points, the simplex algorithm (named as Simplex 1) continues to improve the intensity. For a comparison, the intensity is also maximized by the simplex algorithm alone (Simplex 2). Simplex 1 and Simplex 2 are the same except that the initial guess for Simplex 1 comes from the MBAC algorithm, but the initial guess for Simplex 2 is zero. Both simplex algorithms stop after $\tilde{P} = 200$ intensity measurements, when they have converged. The sampling intervals between the 11th and the 19th samples vary because of the computational time of the NLLS algorithm, as will be discussed later. After Simplex 1 is switched, the sampling rate returns to 50 Hz.

Figure 4.8 shows the convergence curve for one static aberration which gives the lowest initial intensity. The intensity has been normalized as $\tilde{y}(k) = y(k)/y_{max}$ *

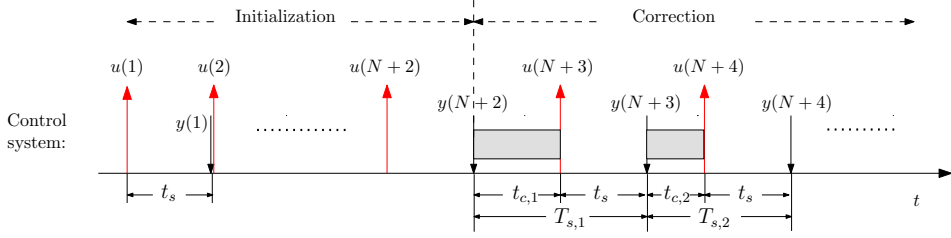


Figure 4.7: Time line of the WFSless AO system with the MBAC algorithm, including initialization and aberration correction. The initial sampling interval is $t_s = 20$ ms. The computational time $t_{c,1}$ for the first aberration estimation takes about 40 ms, while the estimation time $t_{c,2}$ afterwards takes about 20 ms because a better initial guess is provided for the solving the NLLS problem.

0.78), where $\tilde{y}(k)$ is the normalized intensity, also accounting for the intensity transmission ratio (78%) of the disturbance generator. The initial intensity without correction is 0.17. After $N + 2 = 11$ samples are collected, the aberration is estimated and corrected by the MBAC algorithm. The intensity increases to 0.38 (about 2.2 times of the initial value) at the 12th time sample. With one more data samples acquired, the intensity jumps to 0.83 at the 13th time sample, which is almost 5 times of the initial value. At the 14th time sample, the intensity already converges to 0.86 and the intensity keeps at about 0.86 from the 15th and 19th data points. Simplex 1 continues to increase the intensity from the 20th time sample. Because the MBAC algorithm provides a better initial value for Simplex 1, the convergence speed is improved.

Figure 4.9 shows the convergence curve averaged over 20 experiments and the standard deviation of $\tilde{y}(k)$ for $k \geq 12$. The initial intensity is 0.49 in average. With the MBAC algorithm, the intensity increases to 0.82 (an improvement of 67%) and 0.87 (an improvement of 78%) at the 12th and 13th time sample, respectively. The intensity converges to 0.89 at the 15th time sample, while it takes Simplex 2 about 45 time samples to reach the same level. Because Simplex 1 starts at a better initial condition provide by MBAC, the intensity reaches 0.95 at the 60th time sample, while Simplex 2 takes 90 time samples to reach the same level. A significant improvement has been achieved in correction speed. The standard deviation of $\tilde{y}(k)$ with MBAC is also smaller than with the simplex algorithm. For instance, at the 15th time sample, the standard deviation of $\tilde{y}(k)$ with the MBAC algorithm is about 0.02 while that with Simplex 2 is 0.08, about 3 times larger. This indicates that the MBAC algorithm can improve the intensity in a more deterministic manner than simplex.

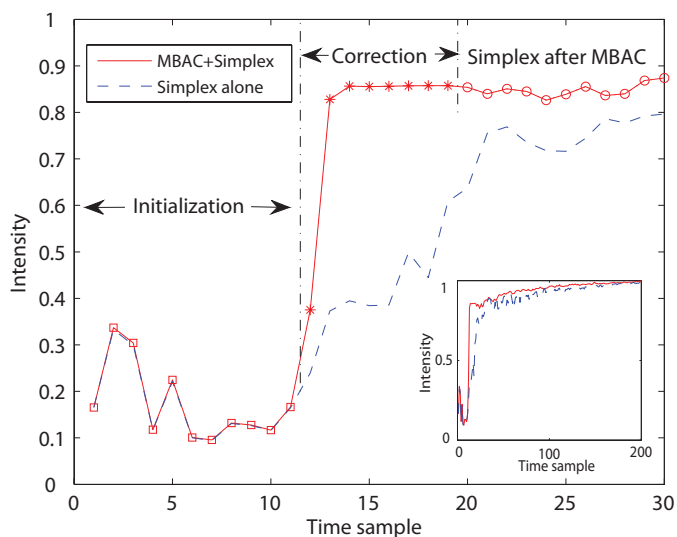


Figure 4.8: Aberration correction with the MBAC+Simplex algorithm and with the simplex algorithm alone, for one static aberration. The MBAC algorithm consists of the initialization and the aberration correction. The initial intensity is 0.17. With the MBAC algorithm, the intensity converges to 0.86 at the 14th time sample, which it takes 30 time samples for the simplex algorithm alone to reach 0.8. The simplex algorithm after MBAC also shows faster convergence than the simplex algorithm alone.

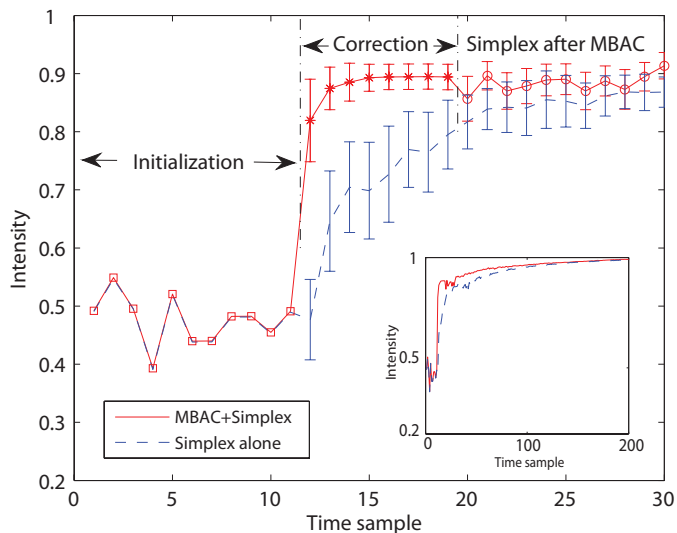


Figure 4.9: Correction of 20 static aberrations. The initial intensity is 0.49 in average. With the MBAC algorithm, the intensity increases to 0.82 at the 12th time sample and to 0.87 at the 13th time sample. The intensity converges to 0.89 by the MBAC at the 15th time sample, while Simplex 2 needs 45 time samples to reach the same level. The standard deviation of $\tilde{y}(k)$ is also reduced with the MBAC algorithm, indicating that MBAC can give a more deterministic intensity improvement than simplex.

4.5.4 Computational complexity

Referring to Figure 4.7, the computational time varies from each time when the aberration is estimated. In the first aberration estimation after 11 data samples, the cost function $J(\hat{a}, \hat{x})$ is evaluated for about 578 times by the function *fmincon* and $t_{c,1}$ is about 40 ms in average. The sampling interval between the 11th and the 12th time sample is then equal to $T_{s,1} = t_{c,1} + t_s = 40 + 20 = 60$ ms. In the aberration estimations afterwards, because better initial guess is provided for \hat{a} and \hat{x} , the number of cost function evaluations is reduced to 251 in average and the computational time $t_{c,2}$ reduces to about 20 ms. The sampling interval becomes $T_{s,2} = 20 + 20 = 40$ ms. In applications where the correction speed is the most important, the MBAC algorithm alone can be used and the correction may stop, for instance, after 15 time samples in our experiments. This leads to a total correction time of $t_s \times 11 + T_{s,1} + T_{s,2} \times 3 = 400$ ms. If the final value needs more concerns, then the hybrid MBAC+Simplex algorithm can be used, which gives a higher end value than MBAC alone and the convergence speed is improved.

4.6 Conclusion

A new approach has been proposed for aberration estimation and correction in WFSless AO systems. The wavefront aberration is estimated by solving a NLLS problem online, based on the model of the WFSless AO system and a minimum number of $N + 2$ intensity measurements. Experimental results show that in average 82% of the maximum intensity can be achieved at the $N + 3 = 12$ th time sample by the MBAC algorithm and intensity converges to 89% at the 15th time sample. With the better initial condition provide by the MBAC algorithm, the simplex algorithm also shows faster convergence than used alone.

Future work will further improve the correction speed by increasing the sampling rate of the control system and considering the dynamics of the DM.

Conclusions and Recommendations

This chapter concludes the thesis and gives recommendations for future work.

5.1 Conclusions

This thesis demonstrates that the performance of closed-loop AO systems is improved by accurate modeling of the AO system and model-based control, thus meeting the goal in Chapter 1.

To have an accurate model of the WFS-based AO system, hysteresis in the PDM is compensated by inverse hysteresis models. The inverse hysteresis model is identified from the hysteresis curve of a single piezo-actuator, which is measured directly by the WFS. Experimental results show that hysteresis in each actuator in the PDM is reduced from 16% to about 1% in average, thus the nonlinearity and the uncertainty in the AO system is reduced. After the AO system is linearized by hysteresis compensation, a linear dynamic AO model is identified by a closed-loop subspace identification approach. Since the MIMO dynamic AO model is identified directly from experimental data without any assumption on the decoupling of actuator dynamics or in the timing of separate components in the loop, high accuracy is achieved for the AO model. The validation data set shows that the VAF of the linear dynamic AO model with hysteresis compensation is as high as 98.4% while the VAF of conventional static AO model without hysteresis compensation is only 72.0%. A controller is then designed to minimize the variance of the residual wavefront error. The controller is based on the models of the AO system and the disturbance. During the controller design, the internal model control (IMC) approach is used to convert the feedback optimal controller design problem to a feedforward optimal controller design problem. The performance of the closed-loop AO system with the proposed controller is evaluated by experiments and compared with the conventional controller. Experimental results show that the variance of the residual error has been reduced by 30% by the proposed controller compared to the conventional controller.

Aberration correction is sped up by accurate modeling of the WFSless AO system and model-based control in the WFSless AO system. To reduce the uncertainty in the system, the hysteresis in the PDM is compensated by inverse hysteresis models as well, but the hysteresis curve of the piezo-actuator is extracted from the intensity measurement of the photodiode. Experimental results show that the largest gap in the intensity loop has been reduced by over 60%. After the hysteresis is compensated, the system aberration in the WFSless AO system is corrected by the simplex optimization algorithm and a nonlinear model is identified for the WFSless AO system using the black-box identification method. A 2-layer feedforward neural network is used to describe the input-output behavior of the WFSless AO system. When the aberration plate is inserted in the optical path, the DM is deformed in $N + 2$ predefined shapes and the corresponding intensity measurements are collected. The unknown aberration is initially estimated based on the neural network and $N + 2$ intensity measurements, and then refined iteratively. This approach is validated in an experimental setup with 20 static aberrations having Kolmogorov spatial distributions. By correcting $N = 9$ Zernike modes, an intensity improvement from 49% of the maximum value to 89% has been achieved in average based on $N + 5 = 14$ intensity measurements. With the lowest initial intensity, an improvement from 17% of the maximum value to 86% has been achieved based on $N + 4 = 13$ intensity measurements. The convergence speed of the proposed model-based control algorithm is about twice as fast as the simplex optimization algorithm.

5.2 Recommendations

Although model-based control has shown to be able to improve the performance of the closed-loop AO systems, this is still far from the end of the story. Future work may focus on the following aspects:

- In this thesis, to reduce the computational complexity, only 28 sensor measurements are used for modeling and control. As the number of sensor measurements and actuators in the AO system increase, the size of the data matrices in the closed-loop subspace identification algorithm increases dramatically, which requires a large memory and computational power for the model identification. Therefore an efficient algorithm is called for identification of large scale AO system.
- Any physical system has its limitations or constraints, e.g., the voltage limit of the DM, the maximum slew rate of the DM, the maximum stress in the DM face plate or in the connection point between the actuator and the DM face plate. These constraints can be included in the controller design for a improved performance in reality or for a longer lifetime of the system.
- Dynamics in the WFSless AO is neglected in this thesis because the sampling rate of the WFSless AO is far from the resonant frequency of the DM. However, to achieve a high correction speed in time, the sampling rate of

the WFSless AO system should be increased and as a consequence, the dynamics of the DM will become more significant. As demonstrated in this thesis, the performance of the closed-loop WFS-based AO system has been improved by accurately modeling the dynamics of the AO system. This motivates that the dynamics in the WFSless AO system should be modeled for an improved convergence at a high sampling rate. The presence of both nonlinearity and dynamics in the WFSless AO system imposes a challenge for modeling the AO system and aberration estimation.

- In scanning-type microscopes, the image is formed by scanning each point in the specimen and the aberration changes with the scanned point. As inspired by model-based control in WFS-based AO systems, if a model can be built which accounts for the temporal and spatial correlation in the aberration during the scanning process, then this model can be incorporated in the controller to predict the aberration in advance. Thus the wavefront aberration can be corrected efficiently during the scanning process.
- The only measurement available in the WFSless AO system in this thesis is the intensity within the pin hole, which is the integration of intensity distribution over the pin hole aperture. Information is lost on the intensity distribution due to the integration. If a camera is used to measure the intensity distribution in the pin hole instead of a photodiode, then the wavefront aberration can be estimated more efficiently as a camera provides richer information than a photodiode.

Bibliography

- [1] J.W. Hardy. *Adaptive Optics for Astronomical Telescopes*. Oxford University Press, New York, USA, 1998.
- [2] R. Tyson. *Principle of Adaptive Optics*. Academic Press, Boston, USA, 1998.
- [3] F. Roddier. *Adaptive Optics in Astronomy*. Cambridge University Press, Cambridge, UK, 1999.
- [4] J.B. Pawley. *Handbook of Biological Confocal Microscopy (3rd Edition)*. Springer, New York, USA, 2006.
- [5] M. Born and E. Wolf. *Principles of Optics: Electromagnetic Theory of Propagation, 7th ed.* Cambridge Univ. Press, Cambridge, U.K., 1999.
- [6] U. Wittrock, I. Buske, and H.M. Heuck. Adaptive aberration control in laser amplifiers and laser resonators. In *Proceeding of SPIE*, volume 4969, pages 122–136, 2003.
- [7] D.L. Fried. Least-square fitting a wave-front distortion estimate to an array of phase-difference measurements. *J. Opt. Soc. Am.*, 67(3):370–375, 1977.
- [8] R.H. Hudgin. Wave-front reconstruction for compensated imaging. *J. Opt. Soc. Am.*, 67(3):375–378, 1977.
- [9] J. Herrmann. Least-squares wave front errors of minimum norm. *J. Opt. Soc. Am.*, 70(1):28–35, 1980.
- [10] E.P. Wallner. Optimal wave-front correction using slope measurements. *J. Opt. Soc. Am.*, 73(12):1771–1776, 1983.
- [11] P.A. Bakut, V.E. Kirakosyants, V.A. Loginov, C.J. Solomon, and J.C. Dainty. Optimal wavefront reconstruction from a shack-hartmann sensor by use of a bayesian algorithm. *Optics Communications*, 109(1-2):10 – 15, 1994.
- [12] N.F. Law and R.G. Lane. Wavefront estimation at low light levels. *Optics Communications*, 126(1-3):19 – 24, 1996.
- [13] J.W. Goodman. *Introduction to Fourier Optics (2nd edition)*. McGraw-Hill, USA, 1996.

- [14] F.J.G. Stoffelena N.J. Doelman, K.J.G. Hinnen and M. Verhaegen. Optimal control strategy to reduce the temporal wavefront error in ao systems. *Proc. SPIE*, 5490:1426–1437, 2004.
- [15] C. Kulcsár, H.-F. Raynaud, C. Petit, J.-M. Conan, and P.V. de Lesegno. Optimal control, observers and integrators in adaptive optics. *Opt. Express*, 14:7464–7476, 2006.
- [16] N.J. Doelman, P.R. Fraanje, I. Houtzager, and M. Verhaegen. Real-time optimal control for adaptive optics systems. *Eur. J. Control*, 15:480–488, 2009.
- [17] J.-M. Conan, G. Rousset, and P.Y. Madec. Wave-front temporal spectra in high-resolution imaging through turbulence. *J. Opt. Soc. Am. A*, 12(7):1559–1570, 1995.
- [18] E. Gendron and P. Léna. Astronomical adaptive optics: I. modal control optimization. *Astronomy Astrophys*, 291:337–352, 1994.
- [19] B. Ellerbroek. Optimizing closed-loop adaptive-optics performance with use of multiple control bandwidths. *J. Opt. Soc. Am. A*, 11:2871–2886, 1994.
- [20] R. Paschall and D. Anderson. Linear quadratic Gaussian control of a deformable mirror adaptive optics system with time-delayed measurements. *Appl. Opt.*, 32:6347–6358, 1993.
- [21] D. Looze, M. Kasper, S. Hippler, O.B. Ans, and R. Weiss. Optimal compensation and implementation for adaptive optics systems. *Experimental Astronomy*, 15:67, 2003.
- [22] D.P. Looze. Minimum variance control structure for adaptive optics systems. *J. Opt. Soc. Am. A*, 23:603–612, 2006.
- [23] D.P. Looze. Linear-quadratic-Gaussian control for adaptive optics systems using a hybrid model. *J. Opt. Soc. Am. A*, 26:1–9, 2009.
- [24] B.L. Roux, J.-M. Conan, C. Kulcsár, H.-F. Raynaud, L. Mugnier, and T. Fusco. Optimal control law for classical and multiconjugate adaptive optics. *J. Opt. Soc. Am. A*, 21:1261–1276, 2004.
- [25] C. Petit, J.-M. Conan, C. Kulcsár, H.-F. Raynaud, T. Fusco, J. Montri, and D. Rabaud. Optimal control for multi-conjugate adaptive optics. *Comptes Rendus Physique*, 6(10):1059 – 1069, 2005.
- [26] C. Petit, J.-M. Conan, C. Kulcsár, H.-F. Raynaud, T. Fusco, J. Montri, and D. Rabaud. First laboratory demonstration of closed-loop kalman based optimal control for vibration filtering and simplified mcao. volume 6272, page 62721T. SPIE, 2006.
- [27] C. Correia, H.-F. Raynaud, C. Kulcsár, and J.-M. Conan. On the optimal reconstruction and control of adaptive optical systems with mirror dynamics. *J. Opt. Soc. Am. A*, 27(2):333–349, 2010.

- [28] K.J.G. Hinnen, M. Verhaegen, and N. Doelman. Exploiting the spatiotemporal correlation in adaptive optics using data-driven H_2 -optimal control. *J. Opt. Soc. Am. A*, 24:1714–1725, 2007.
- [29] K.J.G. Hinnen. *Data-Driven Optimal Control for Adaptive Optics*. PhD thesis, TU Delft, 2007.
- [30] K.J.G. Hinnen, M. Verhaegen, and N. Doelman. A data-driven H_2 -optimal control approach for adaptive optics. *IEEE Transactions on Control Systems Technology*, 16:381–395, 2008.
- [31] B.L. Ellerbroek and T.A. Rhoadarmer. Adaptive wavefront control algorithms for closed loop adaptive optics. *Mathematical and Computer Modelling*, 33(1-3):145 – 158, 2001. Computation and control VI proceedings of the sixth Bozeman conference.
- [32] J.S. Gibson, C.-C. Chang, and B.L. Ellerbroek. Adaptive optics: Wave-front correction by use of adaptive filtering and control. *Appl. Opt.*, 39(16):2525–2538, 2000.
- [33] S. Monirabbasi and S. Gibson. Adaptive control in an adaptive optics experiment. *J. Opt. Soc. Am. A*, 27(11):A84–A96, 2010.
- [34] P. Massioni, R. Fraanje, and M. Verhaegen. Adaptive optics application of distributed control design for decomposable systems. pages 7113 – 7118. IEEE, 2006.
- [35] P. Massioni. *Decomposition Methods for Distributed Control and Identification*. PhD thesis, Delft University of Technology, 2010.
- [36] R. Fraanje, J. Rice, M. Verhaegen, and N. Doelman. Fast reconstruction and prediction of frozen flow turbulence based on structured kalman filtering. *J. Opt. Soc. Am. A*, 27(11):A235–A245, 2010.
- [37] J. Rice. *Efficient Algorithms for Distributed Control: A Structure Matrix Approach*. PhD thesis, Delft University of Technology, 2010.
- [38] M.A. Vorontsov, G.W. Carhart, D.V. Pruidze, J.C. Ricklin, and D. G. Voelz. Adaptive imaging system for phase-distorted extended source and multiple-distance objects. *Appl. Opt.*, 36(15):3319–3328, 1997.
- [39] G. Vdovin. Optimization-based operation of micromachined deformable mirrors. In *Proceeding of SPIE*, volume 3353, pages 902–909, 1998.
- [40] M.A. Vorontsov, G.W. Carhart, M. Cohen, and G. Cauwenberghs. Adaptive optics based on analog parallel stochastic optimization: analysis and experimental demonstration. *J. Opt. Soc. Am. A*, 17(8):1440–1453, 2000.
- [41] W. Lubeigt, G. Valentine, J.M. Girkin, E. Bente, and D. Burns. Active transverse mode control and optimization of an all-solid-state laser using an intracavity adaptive-optic mirror. *Opt. Express*, 10(13):550–555, 2002.

- [42] M. de Boer, K.J.G. Hinnen, M. Verhaegen, R. Fraanje, G. Vdovin, and N. Doelman. Control of a thermal deformable mirror: correction of a static disturbance with limited sensor information. In *Proceedings of the 4th International Workshop on Adaptive Optics for Industry and Medicine*, pages 61–71, Münster, Germany, 2003.
- [43] R. El-Agmy, H. Bulte, A.H. Greenaway, and D. Reid. Adaptive beam profile control using a simulated annealing algorithm. *Opt. Express*, 13(16):6085–6091, 2005.
- [44] P. Yang, Y. Liu, W. Yang, M.W. Ao, S.J. Hu, B. Xu, and W.H. Jiang. Adaptive mode optimization of a continuous-wave solid-state laser using an intracavity piezoelectric deformable mirror. *Opt. Comm.*, 278(2):377 – 381, 2007.
- [45] A.A. Aleksandrov, A.V. Kudryashov, A.L. Rukosuev, T.Y. Cherezova, and Y.V. Sheldakova. An adaptive optical system for controlling laser radiation. *J. Opt. Technol.*, 74(8):550–554, 2007.
- [46] W. Lubeigt, S.P. Poland, G.J. Valentine, A.J. Wright, J.M. Girkin, and D. Burns. Search-based active optic systems for aberration correction in time-independent applications. *Appl. Opt.*, 49(3):307–314, 2010.
- [47] O. Albert, L. Sherman, G. Mourou, T.B. Norris, and G. Vdovin. Smart microscope: an adaptive optics learning system for aberration correction in multiphoton confocal microscopy. *Opt. Lett.*, 25(1):52–54, 2000.
- [48] L. Sherman, J.Y. Ye, O. Albert, and T.B. Norris. Adaptive correction of depth-induced aberrations in multiphoton scanning microscopy using a deformable mirror. *J. Microscopy*, 206(1):65–71, 2002.
- [49] P. Marsh, D. Burns, and J.M. Girkin. Practical implementation of adaptive optics in multiphoton microscopy. *Opt. Express*, 11(10):1123–1130, 2003.
- [50] A.J. Wright, D. Burns, B.A. Patterson, S.P. Poland, G.J. Valentine, and J.M. Girkin. Exploration of the optimisation algorithms used in the implementation of adaptive optics in confocal and multiphoton microscopy. *Microscopy Research and Technique*, 67(1):36–44, 2005.
- [51] S.P. Poland, A.J. Wright, and J.M. Girkin. Evaluation of fitness parameters used in an iterative approach to aberration correction in optical sectioning microscopy. *Appl. Opt.*, 47(6):731–736, 2008.
- [52] M.J. Booth, M.A.A. Neil, R. Juskaitis, and T. Wilson. Adaptive aberration correction in a confocal microscope. *Proc. Nat. Acad. Sci.*, 99(9):5788–5792, 2002.
- [53] M.J. Booth. Wave front sensor-less adaptive optics: a model-based approach using sphere packings. *Opt. Express*, 14(4):1339–1352, 2006.
- [54] M.J. Booth. Wavefront sensorless adaptive optics for large aberrations. *Opt. Lett.*, 32(1):5–7, 2007.

- [55] D. Debarre, M.J. Booth, and T. Wilson. Image based adaptive optics through optimisation of low spatial frequencies. *Opt. Express*, 15(13):8176–8190, 2007.
- [56] D. Débarre, E.J. Botcherby, M.J. Booth, and T. Wilson. Adaptive optics for structured illumination microscopy. *Opt. Express*, 16(13):9290–9305, 2008.
- [57] D. Débarre, E.J. Botcherby, T. Watanabe, S. Srinivas, M.J. Booth, and T. Wilson. Image-based adaptive optics for two-photon microscopy. *Opt. Lett.*, 34(16):2495–2497, 2009.
- [58] *Adaptive Optics Product Guide*. Flexible Optics B.V., 2008.
- [59] A.V. Kudryashov and V.I. Shmalhause. Semipassive bimorph flexible mirrors for atmospheric adaptive optics applications. *Opt. Eng.*, 35:3064–3073, 1996.
- [60] Q. Yang, C. Ftacclas, M. Chun, and D. Toomey. Hysteresis correction in the curvature adaptive optics system. *J. Opt. Soc. Am. A*, 22:142–147, 2005.
- [61] A. Dubra, J. Massa, and C. Paterson. Preisach classical and nonlinear modeling of hysteresis in piezoceramic deformable mirrors. *Opt. Express*, 13:9062–9070, 2005.
- [62] D. Gallieni, M. Tintori, M. Mantegazza, E. Anaclerio, L. Crimella, M. Acerboni, R. Biasi, G. Angerer, M. Andrigettoni, A. Merler, D. Veronese, J. L. Carel, G. Marque, E. Molinari, D. Tresoldi, G. Toso, P. Spanó, M. Riva, R. Mazzoleni, A. Riccardi, P. Mantegazza, M. Manetti, M. Morandini, E. Vernet, N. Hubin, L. Jochum, P. Madec, M. Dimmler, and F. Koch. Voice-coil technology for the E-ELT M4 Adaptive Unit. *Proc. of 1st AO4ELT conference*, page 06002, 2010.
- [63] R. Hamelinck, N. Rosielle, M. Steinbuch, and N. Doelman. Electromagnetic DM technology meets future AO demands. *Proc. of 1st AO4ELT conference*, page 06005, 2010.
- [64] G. Vdovin and P.M. Sarro. Flexible mirror micromachined in silicon. *Appl. Opt.*, 34(16):2968–2972, 1995.
- [65] T. Bifano, S. Cornelissen, and P. Bierden. MEMS deformable mirrors in astronomical adaptive optics. *Proc. of 1st AO4ELT conference*, page 06003, 2010.
- [66] C. Blain, R. Conan, C. Bradley, O. Guyon, and C. Vogel. Characterisation of the influence function non-additivities for a 1024-actuator MEMS deformable mirror. *Proc. of 1st AO4ELT conference*, page 06009, 2010.
- [67] N. Hubin, B.L. Ellerbroek, R. Arsenault, R.M. Clare, R. Dekany, L. Gilles, M. Kasper, G. Herriot, M. Le Louarn, E. Marchetti, S. Oberti, J. Stoesz, J. P. Veran, and C. Vrinaud. Adaptive optics for extremely large telescopes. *Proceedings of the International Astronomical Union*, 1(Symposium S232):60–85, 2005.

- [68] E. Fedrigo, M. Kasper, L. Ivanescu, and H. Bonnet. Real-time control of ESO adaptive optics systems. *Automatisierungstechnik*, 53(10):470–483, 2005.
- [69] B. Crépy, S. Chaillot, J. -M. Conan, R. Cousty, C. Delrez, M. Dimmler, J.L. Dournaux, S. De Zotti, E. Gabriel, R. Gasmi, R. Grasser, N. Hubin, P. Jagourel, L. Jochum, F. Locre, P. Y. Madec, P. Morin, M. Mueller, G. Petit, D. Petitgas, J. J. Roland, J. C. Siquin, and E. Vernet. The M4 adaptive unit for the E-ELT. *Proc. of 1st AO4ELT conference*, page 06001, 2010.
- [70] S.J. Thompson, P. Doel, D. Brooks, and M. Strangwood. A 1-metre Ni coated CFRP demonstrator for large deformable mirrors. *Proc. of 1st AO4ELT conference*, page 06007, 2010.
- [71] N. Olivier, D. Débarre, and E. Beaurepaire. Dynamic aberration correction for multiharmonic microscopy. *Opt. Lett.*, 34(20):3145–3147, 2009.
- [72] A. Chiuso, R. Muradore, and E. Marchetti. Dynamic calibration of adaptive optics systems: a system identification approach. *Proc. of the 47th IEEE Conference on Decision and Control, CDC*, pages 750–755, 2008.
- [73] M. Gevers. Identification for control: from the early achievements to the revival of experiment design. *European Journal of Control*, 11:1–18, 2005.
- [74] M.A. van Dam, D. Le Mignant, and B.A. Macintosh. Performance of the keck observatory adaptive-optics system. *Appl. Opt.*, 43:5458–5467, 2004.
- [75] D. Croft, G. Shed, and S. Devasia. Creep, hysteresis, and vibration compensation for piezoactuators: atomic force microscopy application. *ASME J. Dyn. Syst., Meas., and Control*, 123:35–43, 2001.
- [76] H. Janocha. *Adaptronics and Smart Structures: Basics, Materials, Design, and Applications*. Springer, 2007.
- [77] E. Bai. Decoupling the linear and nonlinear parts in hammerstein model identification. *Automatica*, 40(4):671 – 676, 2004.
- [78] M.P. Chang, A. Zadrozny, D.F. Buscher, C.N. Dunlop, and D.J. Robinson. Hysteresis correction of a piezoelectrically actuated segmented mirror. *Proc. SPIE*, 3353:864–871, 1998.
- [79] A. Holman, P. Scholte, W. Heerens, and F. Tunistra. Analysis of piezo actuators in translation constructions. *Rev. Sci. Instrum.*, 66:3208–3215, 1995.
- [80] B. Coleman and M. Hodgdon. A constitutive relation for rate-independent hysteresis in ferromagnetically soft material. *Int. J. Eng. Sci.*, 24:897–919, 1986.
- [81] K. Dirscherl, J. Garnas, and L. Nielsen. Modeling the hysteresis of a scanning probe microscope. *J. Vac. Sci. Technol*, 18:621–625, 2000.
- [82] I.D. Mayergoyz. *Mathematical Models of Hysteresis and Their Applications*. Elsevier, Amsterdam, 2003.

- [83] K.J.G. Hinnen, R. Fraanje, and M. Verhaegen. The application of initial state correction in iterative learning control and the experiment validation on a piezoelectric tube scanner. *Proc. of the Institution of Mech. Eng. Part I - Journal of Systems and Control Engineering*, 218:503–511, 2004.
- [84] P. Ge and M. Jouaneh. Tracking control of a piezoceramic actuator. *IEEE Trans. Contr. Syst. Technol.*, 4:209, 1996.
- [85] H. Demuth, M. Beale, and M. Hagan. *Neural Network Toolbox 5 User's Guide*. The MathWorks, Inc., 2007.
- [86] L. Breiman. Hinging hyperplanes for regression, classification, and function approximation. *Information Theory, IEEE Transactions on*, 39(3):999–1013, May 1993.
- [87] P. Pucar and J. Sjöberg. On the hinge-finding algorithm for hingeing hyperplanes. *Information Theory, IEEE Transactions on*, 44(3):1310–1319, May 1998.
- [88] R. Fraanje. *Robust and fast schemes in broadband active noise and vibration control*. PhD thesis, Enschede, 2004.
- [89] D. Meschede. *Optics, Light and Lasers: The Practical Approach to Modern Aspects of Photonics and Laser Physics, 2nd, Revised and Enlarged Edition*. WILEY-VCH Verlag GmbH, Weinheim, 2007.
- [90] R. Pintelon and J. Schoukens. *System Identification: A Frequency Domain Approach*. IEEE Press, New York, 2001.
- [91] L. Foucault. Memoire sur la construction des telescopes en verre argente. *Annales de l'Observatoire de Paris*, 5:197–237, 1859.
- [92] M. Loktev, D. Monteiroa, and G. Vdovin. Comparison study of the performance of piston, thin plate and membrane mirrors for correction of turbulence-induced phase distortions. *Opt. Comm.*, 192:91–99, 2001.
- [93] J.H. Conway and N.J.A. Sloan. *Mathematical Methods for Physicists, 3rd Edition*. Academic Press, Orlando, USA, 1985.
- [94] H. Song, G. Vdovin, R. Fraanje, G. Schitter, and M. Verhaegen. Extracting hysteresis from nonlinear measurement of wavefront-sensorless adaptive optics system. *Opt. Lett.*, 34(1):61–63, 2009.
- [95] M. Verhaegen and V. Verdult. *Filtering and System Identification: A Least Squares Approach*. Cambridge University Press, New York, USA, 2007.
- [96] J. Sjöberg, Q. Zhang, L. Ljung, A. Benveniste, B. Delyon, P. Glorennec, H. Hjalmarsson, and A. Juditsky. Nonlinear black-box modeling in system identification: a unified overview. *Automatica*, 31(12):1691–1724, 1995.
- [97] M. Schwertner, M.J. Booth, and T. Wilson. Characterizing specimen induced aberrations for high NA adaptive optical microscopy. *Opt. Express*, 12(26):6540–6552, 2004.

- [98] G. Vdovin, O. Soloviev, A. Samokhin, and M. Loktev. Correction of low order aberrations using continuous deformable mirrors. *Opt. Express*, 16(5):2859–2866, 2008.
- [99] S. Y. Kung. *Digital Neural Networks*. Prentice-Hall, Upper Saddle River, NJ, USA, 1993.
- [100] S. Haykin. *Neural Networks: a Comprehensive Foundation*. Macmillan, New York, USA, 1994.
- [101] M. Brown and C. Harris. *Neurofuzzy Adaptive Modeling and Control*. Prentice-Hall, New York, USA, 1994.
- [102] W.H. Press, S.A. Teukolsky, and W.T. Vetterling. *Numerical Recipes in C; the Art of Scientific Computing (2nd edition)*. Cambridge University Press, New York, USA, 1992.

List of Abbreviations

2-D	2-dimensional
3-D	3-dimensional
ADC	Analog-to-Digital Converter
AO	Adaptive Optics
ARE	Algebraic Riccati Equation
ARX	Auto-Regressive with eXogenous input
CCD	Charge Coupled Device
CWF	Causal Wiener Filter
CMOS	Complementary Metal-Oxide-Semiconductor
DTFT	Discrete-Time Fourier Transform
DAC	Digital-to-Analog Converter
DM	Deformable Mirror
FIR	Finite Impulse Response
HC	Hysteresis Compensation
HVA	High Voltage Amplifier
IMC	Internal Model Control
LQG	Linear Quadratic Gaussian
IO	Input-Output
LMS	Least-Mean-Squares
LS	Least Squares
LTI	Linear Time-Invariant
MBAC	Model-Based Aberration Correction
MEMS	Micro-Electro-Mechanical Systems
MIMO	Multi-Input Multi-Output
MOESP	Multi-variable Output Error State Space

MSE	Mean Square Error
NLLS	NonLinear Least Squares
OE	Output Error
PBSID	Predictor-Based Subspace IDentification
PDM	Piezo-driven Deformable Mirror
PSD	Power Spectral Density
RLS	Recursive Least Squares
S-H WFS	Shack-Hartmann WaveFront Sensor
SISO	Single-Input Single-Output
SMI	Subspace Model Identification
SNR	Signal-to-Noise Ratio
SSARX	State-Space Auto-Regressive with eXogenous input
SVD	Singular Value Decomposition
VAF	Variance-Accounted-For
VAR	VARiance
WFS	WaveFront Sensor
WFSless	WaveFront-Sensor-less
ZOH	Zero-Order Hold

List of Publications

Journal papers:

- **H. Song**, R. Fraanje, G. Schitter, H. Kroese, G. Vdovin and M. Verhaegen, "Model-based aberration correction in a wavefront-sensor-less adaptive optics system", *Opt. Express*, **18**(23), 24070-24084 (2010).
- **H. Song**, G. Vdovin, R. Fraanje, G. Schitter and M. Verhaegen, "Extracting hysteresis from nonlinear measurement of wavefront-sensorless adaptive optics system", *Opt. Lett.* **34**(1), 61-63 (2009).
- **H. Song**, R. Fraanje, G. Schitter, G. Vdovin and M. Verhaegen, "Controller design for a high-sampling-rate closed-loop adaptive optics system with piezo-driven deformable mirror", accepted by *European Journal of Control*, Special Issue on Adaptive Optics Control for Ground Based Telescopes.

Conference proceedings:

- **H. Song**, R. Fraanje, G. Schitter, G. Vdovin and M. Verhaegen, "Modeling and control of a nonlinear dynamic adaptive optics system", invited paper, in *2010 IFAC Symposium on Mechatronic Systems*, Boston, 13-15 Sep., 2010.
- **H. Song**, R. Fraanje, G. Schitter, G. Vdovin and M. Verhaegen, "Hysteresis compensation in a wavefront-sensor-less adaptive optics system", presented in *the Seventh International Workshop on Adaptive Optics for Industry and Medicine*, Moscow, Russia, 8-11 June, 2009.
- **H. Song**, R. Fraanje, G. Schitter, G. Vdovin and M. Verhaegen, "Hysteresis compensation for a piezo deformable mirror", in *Proceedings of the Sixth International Workshop on Adaptive Optics for Industry and Medicine*, pages 112-117, Ireland, 2007.

Magazine article:

- **H. Song**, R. Fraanje, M. Verhaegen, G. Schitter and G. Vdovin, "New Algorithm improves AO systems without wavefront sensors", *Laser Focus World online*, <http://bit.ly/hznuXP> (February 2011).

Summary

Model-based Control in Adaptive Optics Systems

Hong Song

Adaptive optics (AO), also called as Smart Optics, has received increasing attention in the past decades. The main idea behind AO is to actively sense and compensate the optical aberration in the system such that the image resolution is improved or the light beam is well focused. The applications of AO include ground-based telescopes, scanning-type microscopes, laser systems, human vision correction, etc.

It has been demonstrated that the performance of AO systems are improved by model-based control, either in wavefront-sensor-based (WFS-based) or in wavefront-sensor-less (WFSless) AO systems. But there is still room for further performance improvement by accurately modeling of the AO system and by sophisticated model-based controller design, which is just the goal of this thesis.

Most of existing works on WFS-based AO systems focus on modeling the statistics of the disturbance, but the nonlinearity and dynamics in the AO system itself have not been modeled adequately or incorporated in the controller design. In Chapter 2, it is investigated how to accurately model the hysteresis and dynamics in a WFS-based AO system and use the identified model for controller design. An inverse hysteresis model is identified from a single piezo-actuator in the piezo-driven deformable mirror (PDM) and used to compensate for hysteresis in all actuators, thus linearizing the AO system. A linear dynamic AO model is identified by a closed-loop subspace identification approach. Since the multi-input multi-output dynamic AO model is identified directly from the experimental data without any assumption on the decoupling of actuator dynamics or in the timing of separate components in the loop, the accuracy of the AO model is improved. A model-based controller is then designed to minimize the H_2 norm of the residual wavefront error. Performance of the closed-loop AO system with the proposed controller is evaluated by experiments and compared with the conventional controller. Experimental results show that the variance of the residual error has been reduced by 30% by the proposed controller compared to the conventional controller.

WFSless AO systems suffer from memory-less nonlinearity which originates from the optical system itself (e.g., the light intensity measurement through the

pin hole is nonlinear to the DM surface deflection) and hysteresis in the piezo-actuator (which has a memory effect) if a PDM is used. In Chapter 3, it is discussed how to extract and compensate for the hysteresis in a PDM, only based on the light intensity measurement in a WFSless AO system. Experimental results show that the repeatability of the WFSless AO system has been improved significantly, as the difference between system outputs at the same control input has been reduced by about 73% in case of random excitation. This allows to model the memory-less nonlinearity in the WFSless AO system with high accuracy, which is very important for model-based aberration correction as described in Chapter 4.

In Chapter 4, a novel model-based approach has been proposed to estimate and correct the aberration in a WFSless AO system. After hysteresis compensation for the PDM (as described in Chapter 3), a nonlinear model is identified for the WFSless AO system with the measurement data and a 2-layer feedforward neural network. With the aberration present in the optical path, the PDM is initially excited by a small number of predefined control signals and the corresponding light intensity measurements are collected. Aberration is estimated by solving a set of nonlinear equations online, based on the input-output data and the nonlinear model of the WFSless AO system. With new input-output data available, the aberration estimation and correction are refined iteratively. This approach is validated in the experimental setup with 20 static aberrations. The convergence speed of the proposed model-based control algorithm is about twice as fast as the standard simplex optimization algorithm.

This thesis is concluded that the performance of closed-loop AO systems are improved by model-based control. Since scientific research is a never-ending story, suggestions and recommendations are also given for future work.

Samenvatting

Modelgebaseerde Regeling van Adaptieve Optische Systemen

Hong Song

Adaptieve Optiek (AO), ook wel Slimme Optiek genoemd, heeft de afgelopen decennia een toenemende aandacht gekregen. Het belangrijkste idee achter AO is om de optische verstoring in het systeem actief te meten en te compenseren zodat de resolutie van het beeld verbeterd of de lichtbundel goed gefocusseerd wordt. AO vindt toepassing in grondgebaseerde telescopen, scanning microscopen, laser systemen, menselijk zicht correctie, enz.

Het is aangetoond dat de prestatie van AO systemen verbeterd wordt met behulp van een modelgebaseerde regeling, zowel in golffrontsensor-gebaseerde (WFS-gebaseerde) als in golffrontsensorloos (WFS-less) AO systemen. Maar er is nog steeds ruimte voor verdere verbetering van de prestatie door het nauwkeurig modelleren van het AO systeem, en door geavanceerde modelgebaseerde regelaar ontwerp, wat precies het doel is van dit proefschrift.

Het meeste werk in WFS-gebaseerde AO systemen is gericht op de modellering van de statistiek van de verstoring, echter de niet-lineariteit en de dynamica in het AO systeem zelf zijn niet adequaat gemodelleerd of in rekening gebracht in het ontwerp van de regelaar. In hoofdstuk 2, het is onderzocht hoe de hysteresis en de dynamica in een WFS-gebaseerd AO systeem nauwkeurige gemodelleerd kan worden en hoe het geïdentificeerde model gebruikt kan worden voor het ontwerp van de regelaar. Een inverse hysteresis model is geïdentificeerd met behulp van een enkele piezo-actuator van de piezo-geactueerde vervormbare spiegel (PDM) en dit model is gebruikt om te compenseren voor de hysteresis in alle actuators, op deze wijze wordt het AO systeem gelineariseerd. Een lineair dynamisch AO model is vervolgens geïdentificeerd met behulp van een gesloten-lus subspace identificatie benadering. Omdat het multi-input multi-output dynamische AO-model direct geïdentificeerd is op basis van experimentele gegevens, zonder enige aanname over de ont koppeling van de actuator dynamica of in de timing van de afzonderlijke componenten in de lus, is de nauwkeurigheid van het AO-model vergroot. Een modelgebaseerde regelaar wordt vervolgens ontworpen om de H_2 norm van de resterende golffront fouten te minimaliseren. De prestaties van het gesloten-lus AO-systeem met de voorgestelde controller is geëvalueerd door experimenten en vergeleken met de conventionele controller. Experimentele resul-

taten tonen aan dat de variantie van de residu fout is verminderd met 30 % door de voorgestelde regelaar in vergelijking met de conventionele regelaar.

WFS-loze AO systemen hebben te lijden van geheugen-loze nietlineariteiten als gevolg van het optische systeem zelf (bijv. het intensiteits metingen van het licht door een pen gat is een niet-lineaire functie van de DM oppervlakte vervorming) en de hysteresis in de piezo-actuator (welke een geheugen effect heeft) in geval een PDM gebruikt wordt. In Hoofdstuk 3, bediscussieerd hoe de hysteresis in een PDM kan worden verkregen en hoe deze kan worden gecompenseerd, slechts gebaseerd op metingen van de licht intensiteit in een WFS-loos AO systeem. Experimentele resultaten laten zien dat de herhaalbaarheid van het WFS-loze AO systeem significant verbeterd is, want het verschil tussen de systeem uitgangen bij dezelfde regelingang is verminderd met ongeveer 73% in geval van random excitaties. Dit staat toe om de geheugen-loze nietlineariteit in het WFS-loze AO systeem met een grote nauwkeurigheid te modelleren, hetgeen zeer belangrijk is voor de model-gebaseerde aberratie correctie in Hoofdstuk 4.

In Hoofdstuk 4 wordt een nieuwe model-gebaseerde benadering voorgesteld, om de aberratie in een WFSloos AO systeem, te schatten en te compenseren. Na hysteresis compensatie van de PDM (zoals beschreven in Hoofdstuk 3), wordt er een niet-lineair model van het WFS-loze AO systeem geïdentificeerd op basis van gemeten data en een 2-laags feedforward neurale netwerk. Met de aberratie aanwezig in het optische pad aanwezig, wordt de DM aanvankelijk gexciteerd door een klein aantal vooraf gedefinieerde stuursignalen en de bijbehorende intensiteit metingen worden verzameld. De aberratie wordt geschat door middel van het online oplossen van een stelsel niet-lineaire vergelijkingen, gebaseerd op de ingangs-uitgangs data van het niet-lineaire model van het WFS-loze AO systeem. Met de nieuwe beschikbare ingangs-uitgangs-gegevens worden de schatting van de aberratie en de correctie iteratief verfijnd. Deze aanpak is gevalideerd in een experimentele opstelling met 20 statische afwijkingen. De convergentie snelheid van het voorgestelde model-gebaseerde regel algoritme is ongeveer twee keer zo hoog als het simplex optimalisatie algoritme.

Het proefschrift concludeert dat de prestaties van gesloten-lus AO systemen verbeterd worden door model-gebaseerde regelingen. Aangezien wetenschappelijk onderzoek een nooit eindigend verhaal is, worden ook suggesties en aanbevelingen voor toekomstig onderzoek aangegeven.

Curriculum Vitae

Hong Song (in Chinese convention: Song Hong) was born on 29 December, 1981, in Jingjiang, Jiangsu Province, China. In 1998 he started his undergraduate study in the Department of Lighting Source and Illumination in Fudan University, Shanghai, China, supervised by Dr. Zhang Shanduan and Prof. Liu Muqing. He received his Bachelor degree in 2002. In the same year, he continued as a Master student in the Department of Microelectronics in Fudan University. In 2003, he was involved in the international program between Fudan University and Delft University of Technology (TU Delft) and came to the Department of Microelectronics in TU Delft as an exchange student. In 2005, he graduated from Fudan University and TU Delft (cum laude), with the master thesis *Multiplexing Control of a Piezo Deformable Mirror*, under the supervision of Dr. Gleb Vdovin (TU Delft), Dr. Aleksey Simonov (TU Delft) and Prof. Huang Yiping (Fudan University).

In January 2006, he started his Ph.D. research on Model-based Control in Adaptive Optics Systems, in Delft Center for Systems and Control (DCSC) under the supervision of Prof. Michel Verhaegen, Dr. Gleb Vdovin, Dr. Rufus Fraanje and Prof. Georg Schitter. He has worked on algorithm development and experimental verification of the control algorithms.

He enjoys playing basketball, Taiji and guitar (although only being able to play a single song so far) in his spare time.

